

MERGING CLUSTER COLLABORATION: OPTICAL SURVEY OF A RADIO-SELECTED SAMPLE OF MERGING GALAXY CLUSTERS

N. GOLOVICH^{1,2}, D. M. WITTMAN^{1,3}, W. A. DAWSON²

SUBMITTED TO APJ SUPPLEMENT:

ABSTRACT

In this study of merging galaxy clusters, we argue for the merits of major merger systems for a variety of science goals including constraining the self-interacting dark matter cross section, quantifying the effects of mergers on the intra-cluster medium and galaxy population, and understanding particle acceleration models at cluster-scale shock interfaces. We use radio selection to identify an ensemble of 29 nearly-transverse major merger systems with $0.07 < z < 0.56$. We present results of our spectroscopic and photometric survey of this ensemble. We find that the line-of-sight velocity components of the mergers are typically small (usually $< 1000 \text{ km s}^{-1}$ and often consistent with zero). This suggests that the merger axes of these systems are generally in or near the plane of the sky thus confirming that radio selection has produced the desired effect. We augment these observations with a wide array of archival radio and X-ray observations to understand the merger scenario of each system. In 28 of the 29 systems we identify substructures in the galaxy population aligned with the radio relic and presumed underlying cluster shock. From this ensemble, we identify eight systems to include in a “gold” sample that is prime for further observation, modeling, and simulation study. Additional papers will present weak lensing mass maps and dynamical modeling for each merging system, ultimately leading to new insight into a wide range of astrophysical phenomena at some of the largest scales in the universe.

Keywords: galaxies: clusters: general—dark matter—galaxies: evolution—shock waves

1. INTRODUCTION

Galaxy clusters have long served as astrophysical laboratories for the study of dark matter (DM), the intra-cluster medium (ICM), and galaxies, including their interactions and evolution. In the past decade, galaxy cluster *mergers* have been recognized as particularly fruitful laboratories. Cluster mergers have been used to study the nature of DM (Markevitch et al. 2004; Clowe et al. 2006; Randall et al. 2008) and matter/antimatter asymmetry (Steigman 2008) as well as longstanding astronomical questions such as the origin of cosmic rays (e.g. Bell 1978; Giler et al. 1980; Gabici & Blasi 2003; Brunetti & Jones 2014) and of the red sequence; i.e., do mergers quench, stimulate, or have little effect star formation (e.g. Miller & Owen 2003; Poggianti et al. 2004; Chung et al. 2009; Stroe et al. 2017)? Yet, most observed mergers are still poorly understood even in terms of basic dynamical properties such as time since first pericenter (which we will refer to simply as *age*), relative velocity at first pericenter, and viewing angle. In addition, merging is a multistage process which must be pieced together from instantaneous snapshots of a variety of systems, with simulations providing a framework for fitting them together.

We have therefore formed the Merging Cluster Collaboration to undertake a comprehensive study—combining panchromatic observations and modeling of an ensemble of merging systems, with the following goals:

nrgolovich@ucdavis.edu

¹ Department of Physics, University of California, One Shields Avenue, Davis, CA 95616, USA

² Lawrence Livermore National Laboratory, 7000 East Avenue, Livermore, CA 94550, USA

³ Instituto de Astrofísica e Ciências do Espaço, Universidade de Lisboa, Lisbon, Portugal

- improved constraints on DM self interactions
- improved modeling of shocks, particle acceleration, and turbulence in the ICM
- temporal and spatial description of galaxy evolution of member galaxies

Each of these goals requires a dynamical model of the merger including geometry, temporal information, and relative velocities of the merging subclusters and outward propagating shocks. Such modeling necessitates observations including optical photometry and spectroscopy to map the mass and galaxy distributions; i.e., the non-collisional components. These observations are more valuable when augmented with radio and X-ray imaging which offer complimentary information regarding the collisional ICM, which imprints the merger history for millions of years after core passage.

A basic understanding of major mergers begins with the composition of the subclusters, which is typically $\sim 85\%$ DM, $\sim 13\%$ gas, and $\sim 2\%$ galaxies by mass (Vikhlinin et al. 2006; Sun et al. 2009; Sanderson et al. 2013; Gonzalez et al. 2013). As the subclusters approach and pass through pericenter the gas halos exchange momentum while the approximately non-collisional galaxies and DM continue well past pericenter. Thus, a separation arises between the gas, which remains closer to the center of mass, and the outbound galaxies and DM; mergers clearly exhibiting this separation are said to be *dissociative* (Dawson et al. 2012). The dissociative phase of a merging system is eventually erased as the subclusters pass through subsequent core crossing phases and dynamical friction causes each component to relax and create a new, more massive cluster. In this paper we will

argue for the utility of dissociative mergers as ideal astrophysical laboratories for the study of the constituent galaxies, DM halos, and gas clouds.

In the case of DM, dissociative mergers function as DM colliders: any momentum exchange between the DM halos could result in those halos lagging the outbound galaxies. Such lags will be visible only to the extent that the merger is transverse; the classic transverse merger called the Bullet Cluster (Markevitch et al. 2004; Clowe et al. 2006) provided direct evidence for the existence of DM and has yielded the tightest upper limit on DM self-interaction (Randall et al. 2008, $\sigma_{DM} < 0.7 \text{ cm}^2 \text{ g}^{-1}$) to date based on the DM collider concept. Ensemble analyses have attempted to push this limit lower (Harvey et al. 2015); however, these results were based on single band imaging, and it was shown that the multi-band studies throughout the literature substantially relax this constraint (Wittman et al. 2017). Alternative signals may be apparent in a skewed DM profile with a heavier tail toward the center of mass or even in an induced wobbling of the brightest cluster galaxy (BCG) position long after the merger commences (Kim et al. 2017; Harvey et al. 2017). These studies are motivated from discrepancies at smaller scales between the expectation from simulations and observations (see e.g. Tulin & Yu 2017, for a detailed review). We will discuss merging clusters as DM probes in more detail in §8.

Member galaxies are largely non-collisional, but their trajectories undergo an impulsive period of acceleration as the subclusters overlap and the gravitational potential deepens. Because of this fact, galaxy velocity dispersion is notoriously biased for a few million years after pericenter (e.g. Pinkney et al. 1996). Galaxy spectroscopy is vital for modeling the dynamics of the merger as the galaxies serve as tracer particles for the underlying subcluster halo; however, these observations only offer insight into the line of sight motion. Within individual galaxies, there is still much uncertainty with regard to the change in star formation in merging clusters. The genesis of the red sequence of early type galaxies has been well established and studied in relation to redshift, environment, galaxy density, and merger history (Gunn & Gott 1972; Dressler 1980; Aragon-Salamanca et al. 1993; Kodama & Arimoto 1997; Stanford et al. 1998; Gladders et al. 1998), but a direct understanding of the role of major mergers in this evolution has eluded astronomers to date. In particular, do changes occur in step with major mergers, or is it a continuous transformation more associated with the cluster environment on longer time scales? In this framework, comparison studies of emission lines upstream and downstream of merger shocks have yielded conflicting results with turbulence in the ICM possibly playing a role (e.g. Stroe et al. 2014b).

Finally, the highly collisional ICM undergoes immense change during a merger. Many merging clusters have been identified as such based on their projected two-dimensional X-ray surface brightness profile, which often display bulk disturbances such as cold fronts as well as cluster scale supersonic shocks (e.g. Markevitch 2006; Russell et al. 2010). In systems with a merging cool-core remnant, iconic images such as that of the Bullet Cluster show clearly merging “bullets” with trailing wake features highlighting the stripped gas due to ram-pressure. Radio observations of merging clusters have

shown that the underlying shocks in the ICM are often coincident with diffuse radio emission due to synchrotron radiation of electrons in the ICM as they interact with the shock-compressed magnetic fields in the cluster. Active research is underway in search of explanations of apparent discrepancies in the radio and X-ray inferences of particle acceleration at cluster shock interfaces (e.g. Brunetti & Jones 2014; van Weeren et al. 2017).

A global understanding of the interactions of each component throughout the full timescale of the interaction requires intensive computation. The non-collisional DM and galaxies are often studied through gravity-only N-body simulations. Such simulations have been utilized from sub-galactic (kpc) to cosmological (Gpc) scales to study structure formation, halo mass functions, and DM density profiles with both cold dark matter (CDM) and various self-interacting dark matter (SIDM) prescriptions (e.g. Rocha et al. 2012; Skillman et al. 2014). Meanwhile, studies of galaxy evolution, active galactic nuclei (AGN), particle acceleration, and other baryonic physics require full magneto-hydro dynamics (MHD). These simulations have been carried out across a range of scales including cluster and cosmological scales (e.g. Skillman et al. 2013; Vogelsberger et al. 2014). Simulations have progressed greatly as large-scale computation has become more accessible; however, they are hampered in terms of simulating realistic cluster mergers due to the vast parameter space of initial conditions relating to not only merger geometry but also subcluster ICM properties, formation histories, feedback, etc.

In this paper we focus on observations and modeling of the galaxies in 29 merging clusters. Our results will substantially reduce the phase space of initial conditions for simulators as well as provide a dynamical understanding of each merging system including the number of merging subclusters and the relative line of sight motion. We have developed a galaxy and redshift modeling technique through the analysis of several clusters (Dawson et al. 2015; Golovich et al. 2016; van Weeren et al. 2017; Golovich et al. 2017; Benson et al. 2017). The methods developed as successive clusters presented specific complications that further generalized our analysis technique. This paper is the culmination of this project and is organized as follows. In §2, we describe the rationale for our sample selection, and in §3, we describe our spectroscopic and photometric survey of 29 merging galaxy clusters. We describe the ancillary X-ray and radio data utilized in this paper in §4. In §5, we outline the data analysis methods applied in this paper. In §6 we describe results for each cluster while in §7 we summarize the findings of the sample as a whole. Finally, in §8 we discuss the implications of this initial look at the sample and offer our conclusions. We emphasize the importance of a multi-wavelength study of merging galaxy clusters in order to gather insight into the merging process and to constrain physics therein. We assume a flat Λ CDM universe with $H_0 = 70 \text{ km s}^{-1} \text{ Mpc}^{-1}$, $\Omega_M = 0.3$, and $\Omega_\Lambda = 0.7$.

2. RADIO RELIC SAMPLE: GOALS AND SELECTION

As stated in the previous section, each of the primary science goals addressed while observing, modeling, and simulating merging clusters of galaxies are time dependent. To be more explicit, we desire a sample of mergers

observed between first pericenter and first turnaround and with merger axis near the plane of the sky so apparent offsets are maximized. Transverseness also facilitates our goals of (1) studying the effect of mergers on star formation and galaxy evolution, as galaxy membership is more easily assigned to a particular subcluster when the system is viewed transversely; and (2) studying shock physics and particle acceleration processes, as the shocks will be viewed mostly edge-on. This motivation in turn leads to the following selection considerations.

We have adopted the detection of radio relics as our criterion for transverseness—as opposed to projected galaxy populations or detection of sharp X-ray shock features—because it will select for a range of ages and because radio data support further dynamical inferences. First, the position of the relic is closely linked to the time since pericenter because the shock is launched around the time of pericenter, at about the same speed as the corresponding subcluster in the center-of-mass frame (Springel & Farrah 2007). The shock speed can vary somewhat thereafter depending on the details of the gas profile, but this argument still provides a valuable constraint on the time since pericenter as demonstrated by Ng et al. (2015) in the case of El Gordo. Second, highly polarized relic emission provides strong evidence that the relic is viewed edge-on (Ensslin et al. 1998) which confines the merger axis to near the plane of the sky. In addition to the analytical models of Ensslin et al. (1998), the simulations of Skillman et al. (2013) clearly show this effect. Low polarization, however, could result from disorganized magnetic fields even if the merger is transverse, so the constraint is one-sided. Ng et al. (2015); Golovich et al. (2016, 2017) also demonstrated the value of this constraint on models of El Gordo, MACS J1149.5+2223 (hereafter MACSJ1149), and ZwCl 0008.8+5215 (hereafter ZwCl0008), respectively.

Note that the dynamical parameters allow a degeneracy between outbound and returning scenarios. Even if the viewing angle is known, the velocities and projected separations do not distinguish between these two scenarios, which may have markedly differing ages. The continued outward progression of the radio relic breaks this degeneracy, so the constraint from the relic position is valuable in a different way than the constraint from the polarization. In principle the ram-pressure slingshot (see e.g. Abell 168: Hallman & Markevitch 2004) can also distinguish between these two scenarios—gas beyond the DM suggests that the DM has already turned around—but this may be useful only in systems whose cool-core remnant is sufficiently robust to the extreme forces imparted upon it. Thus, the relic position constraints are the more practicable way to break the degeneracy, thus reinforcing the value of radio selection.

A further advantage of radio selection is that it seems to select for quite massive systems: relic systems recently “weighed” with weak gravitational lensing include El Gordo at $\sim 3 \times 10^{15} M_{\odot}$ (Jee et al. 2014), CIZAJ2242 at $\sim 2 \times 10^{15} M_{\odot}$ (Jee et al. 2014) as well as 1RXSJ0603 (hereafter 1RXSJ0604) and ZwCl0008 at $\sim 1 \times 10^{15} M_{\odot}$ (Jee et al. 2015; Golovich et al. 2017). The high DM column density of these systems potentially makes them more sensitive to DM interactions. Furthermore, there is a positive relationship between radio relic power and

cluster mass (de Gasperin et al. 2014).

Our sample thus begins with the list of known radio relics compiled in Table 3 of Feretti et al. (2012). Each of these clusters contain low surface brightness, steep-spectrum, polarized, and extended radio sources that lie at the periphery of the cluster, and these sources were independently classified as a radio relic in the relevant detailed radio analyses. We discarded relics classified as “roundish” since these are likely radio phoenixes rather than Mpc scale cluster shocks. We then impose cuts designed to enable spectroscopic and weak lensing followup. Systems at very low redshift are not efficient lenses, so we eliminate clusters at $z < 0.07$. We also eliminate systems not observable from the Mauna Kea observatories ($\delta < -31^{\circ}$). To this list, we have added two additional radio relic systems that have appeared in the literature and pass the same selection criteria since the Feretti et al. (2012) paper (PSZ1 G108.18-11.5 and ZwCl 1856+6616, hereafter PSZ1G108 and ZwCl1856, respectively). Finally, we added one of the radio phoenix relics (Abell 2443, hereafter A2443) to our spectroscopic survey due to a gap in an observing run. In total, our sample contains 29 systems listed in Table 1.

The sample is generally at low redshift (~ 0.1 – 0.3) due to radio relics typically being discovered in wide, shallow surveys (e.g. NVSS: Condon et al. 1998). This is a reasonable redshift range for lensing followup, and also has the advantage of mapping given physical separations to substantial angular separations. The main potential drawback of this selection is that it will disfavor the very youngest post-pericenter systems, which have not had time to generate radio relics. At the same time, this selection has the advantage of guaranteeing against the selection of pre-pericenter systems since the presence of a radio relic indicates a shockwave traveling in the ICM.

The radio selection strategy does bring challenges in terms of obtaining spectroscopy and lensing followup. Because radio surveys have gone right through the galactic plane, many of the systems suffer more extinction than is typical in visible-wavelength surveys. The all sky galactic dust extinction map is presented in Figure 1 with all 29 systems in our sample. The most extreme example is CIZAJ2242 with $A_V \approx 1.4$ (the approximation sign emphasizes that the extinction varies over the field; Schlegel et al. 1998). Dawson et al. (2015) describes the success of the position-dependent extinction corrections applied to that system in terms of yielding uniform color selection of cluster members, and Jee et al. (2015) demonstrates that weak lensing can be efficiently measured despite the extinction. The low galactic latitude also affected the spectroscopy not only through extinction but also by causing more slits to be wasted on stars ($\sim 50\%$, Dawson et al. 2015). A contributing factor in this case was the poor quality of imaging available at the time of slitmask design. The next most extincted systems in the sample are A2163 and ZwCl0008, for which A_V is substantially lower, ~ 0.8 . We therefore expect the lensing and galaxy analyses of most of the systems in this sample to exceed the quality of those for CIZAJ2242. We have corrected our photometry for extinction throughout. Now, with the sample defined, the following milestones are to be achieved for each cluster:

- Observations including spectroscopic (Keck

Table 1
The Merging Cluster Collaboration radio-selected sample.

Cluster	Short name	RA	DEC	Redshift	Discovery band	§
1RXS J0603.3+4212	1RXSJ0603	06:03:13.4	+42:12:31	0.226	X-ray	6.1
Abell 115	A115	00:55:59.5	+26:19:14	0.193	Optical	6.2
Abell 521	A521	04:54:08.6	-10:14:39	0.247	Optical	6.3
Abell 523	A523	04:59:01.0	+08:46:30	0.104	Optical	6.4
Abell 746	A746	09:09:37.0	+51:32:48	0.214	Optical	6.5
Abell 781	A781	09:20:23.2	+30:26:15	0.297	Optical	6.6
Abell 1240	A1240	11:23:31.9	+43:06:29	0.195	Optical	6.7
Abell 1300	A1300	11:32:00.7	-19:53:34	0.306	Optical	6.8
Abell 1612	A1612	12:47:43.2	-02:47:32	0.182	Optical	6.9
Abell 2034	A2034	15:10:10.8	+33:30:22	0.114	Optical	6.10
Abell 2061	A2061	15:21:20.6	+30:40:15	0.078	Optical	6.11
Abell 2163	A2163	16:15:34.1	-06:07:26	0.201	Optical	6.12
Abell 2255	A2255	17:12:50.0	+64:03:11	0.080	Optical	6.13
Abell 2345	A2345	21:27:09.8	-12:09:59	0.179	Optical	6.14
Abell 2443	A2443	22:26:02.6	+17:22:41	0.110	Optical	6.15
Abell 2744	A2744	00:14:18.9	-30:23:22	0.306	Optical	6.16
Abell 3365	A3365	05:48:12.0	-21:56:06	0.093	Optical	6.17
Abell 3411	A3411	08:41:54.7	-17:29:05	0.163	Optical	6.18
CIZA J2242.8+5301	CIZAJ2242	22:42:51.0	+53:01:24	0.189	X-ray	6.19
MACS J1149.5+2223	MACSJ1149	11:49:35.8	+22:23:55	0.544	X-ray	6.20
MACS J1752.0+4440	MACSJ1752	17:52:01.6	+44:40:46	0.365	X-ray	6.21
PLCKESZ G287.0+32.9	PLCKG287	11:50:49.2	-28:04:37	0.383	SZ	6.22
PSZ1 G108.18-11.53	PSZ1G108	23:22:29.7	+48:46:30	0.335	SZ	6.23
RXC J1053.7+5452	RXCJ1053	10:53:44.4	+54:52:21	0.072	X-ray	6.24
RXC J1314.4-2515	RXCJ1314	13:14:23.7	-25:15:21	0.247	X-ray	6.25
ZwCl 0008.8+5215	ZwCl0008	00:08:25.6	+52:31:41	0.104	Optical	6.26
ZwCl 1447+2619	ZwCl1447	14:49:28.2	+26:07:57	0.376	Optical	6.27
ZwCl 1856.8+6616	ZwCl1856	18:56:41.3	+66:21:56.0	0.304	Optical	6.28
ZwCl 2341+0000	ZwCl2341	23:43:39.7	+00:16:39	0.270	Optical	6.29

DEIMOS), optical wide-field (Subaru Suprime-Cam), pointed optical (HST ACS/WFC3), X-ray (Chandra ACIS), and radio (e.g., JVLA)

- Optical analysis to estimate the number and location of subclusters
- Redshift analysis to estimate line of sight velocity information of subclusters
- X-ray and radio analysis of shocks and radio relics (including polarization)
- Weak lensing analysis to find location and mass of subclusters
- Dynamical analysis

In this paper, we will discuss the spectroscopic and wide-field optical observations as well as the optical and redshift analyses for our sample of 29 merging clusters. This will result in two of the three inputs for the dynamics analysis as well as classify the mergers by their complexity and reasonability to probe the SIDM hypotheses discussed above.

3. OPTICAL AND SPECTROSCOPIC OBSERVATIONAL CAMPAIGN

This paper focuses on the spectroscopic and ground based optical surveys of 29 merging galaxy clusters. The optical survey has a goal of obtaining lensing quality, wide-field imaging in at least two optical bands allowing the mapping of the red sequence galaxy distribution for each cluster. Many clusters have archival imaging that

we have utilized; however, we have observed 18 clusters with Subaru SuprimeCam to complete the photometric survey. We require at least two optical filters that straddle the 4000Å break in order to select cluster members photometrically via red sequence relations. Furthermore, our weak lensing method makes use of these red sequence relations in order to select background galaxies for lensing study (Jee et al. 2015, 2016; Golovich et al. 2017). Additionally, for clusters that our SuprimeCam observations came before our DEIMOS observations, we made use of the SuprimeCam images for spectroscopic target selection (see §3.2.1).

The spectroscopic survey has a goal of obtaining ~ 200 member galaxy velocities in each system. For binary mergers of clusters with line-of-sight velocity dispersions $\sigma_v \sim 1000 \text{ km s}^{-1}$, this provides enough members to constrain the systemic radial velocity of each subcluster to $\sim 100 \text{ km s}^{-1}$, thus constraining the radial velocity difference between subclusters to $\sim 140 \text{ km s}^{-1}$ in our frame. We used redshifts from the literature when available in order to reduce the amount of new observations required. When obtaining new spectra, we designed observations to also meet the secondary goal of enabling studies of recent star formation and ultimately the link between mergers and star formation. We achieve this by adjusting the observed wavelength range for each cluster to the emitted wavelength range from H β to H α for clusters with $z \lesssim 0.3$ and [O II] 3728 to [O III] for clusters with $z \gtrsim 0.3$. The data available for star formation studies therefore varies from cluster to cluster depending on the number of previously published redshifts and the redshift of the cluster. We searched the literature for

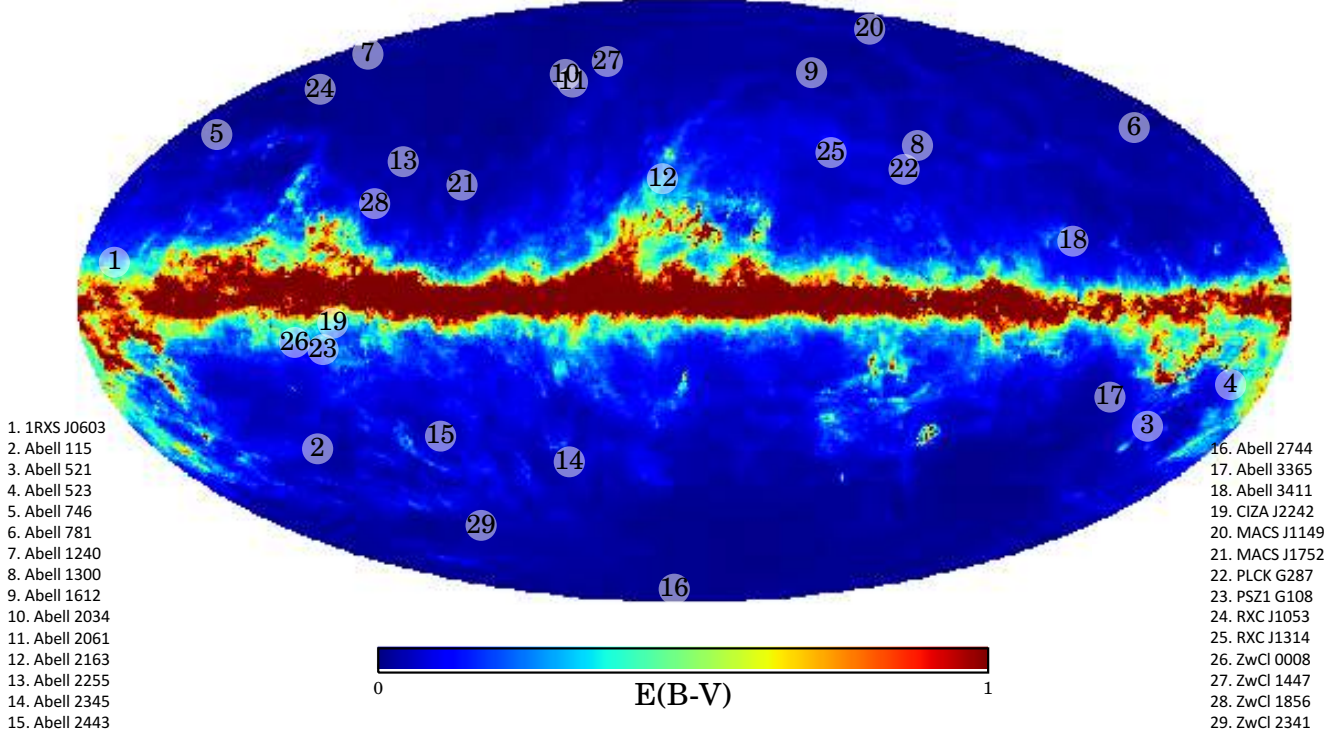


Figure 1. Galactic dust extinction map (Schlegel et al. 1998) with overlaid positions of the 29 systems in our sample.

redshifts using the NASA/IPAC Extragalactic Database⁴ (NED). For each system we considered galaxies within R_{200} and within $\pm 10,000 \text{ km s}^{-1}$ of the systemic redshift to be sufficiently plausible members to reduce the need for new spectra. A substantial amount of data came from previous spectroscopic surveys by the following studies; Beers et al. (A115: 1983); Barrena et al. (A115: 2007); Maurogordato et al. (A521: 2000); Girardi et al. (A523: 2016); Barrena et al. (A1240: 2009); Ziparo et al. (A1300: 2012); Owers et al. (A2034: 2014); Maurogordato et al. (A2163: 2008); Boschin et al. (A2345: 2010); Couch & Sharples (A2744: 1987); Boschin et al. (A2744: 2006); Owers et al. (A2744: 2011); Ebeling et al. (MACSJ1149: 2014); Valtchanov et al. (RXCJ1314: 2002). Additional observations were required for 18 systems with many having no more than a handful of previously published member redshifts. In the following subsections we will detail the targeting, observing, and data reductions of our optical and spectroscopic surveys.

3.1. Subaru SuprimeCam Observations

We observed 18 clusters over four nights in using the 80 Megapixel SuprimeCam (Miyazaki et al. 2002) camera on the Subaru Telescope on Mauna Kea. Table 2 summarizes these observations. The basic strategy is to achieve weak lensing quality in one filter and obtain a second filter to define the color of detected objects by straddling the 4000 Å break. For the lensing quality image, the exposure time was 2880 s (8×360 s) and we rotated the field between each exposure by 15° in order to distribute the bleeding trails and diffraction spikes from

bright stars azimuthally to be later removed by median-stacking. This scheme enabled us to maximize the number of detected galaxies, especially for background source galaxies for weak lensing near stellar halos or diffraction spikes. In the second and third filters (g and/or i), the exposure time was 720 s (4×180 s). These exposures were rotated by 30° from exposure to exposure for the same reason as above. In order to efficiently fill the time of each observing night, we added a third band to several clusters. The actual observing times may vary due to real-time changes to the observational plan due to unexpected lost time, weather, etc.

Archival Subaru SuprimeCam imaging was downloaded from the SMOKA data archive (Baba et al. 2002), and is detailed in Table 3. We note that the observational strategy for the archival data did not prescribe rotating between exposures, so diffraction spikes and bleeding trails are present. Also, we did not make use of the full set of archival images for these clusters since we only required two bands of imaging in order to define the color and complete a color-magnitude selection. We utilized the deepest images available that satisfy this requirement ensuring good seeing conditions.

3.1.1. Subaru SuprimeCam: Data Reduction

The CCD processing (overscan subtraction, flat-fielding, bias correction, initial geometric distortion rectification, etc) were carried out with the SDFRED2 package (Ouchi et al. 2004). Much of the archival data required the first version of this pipeline (SDFRED1: Yagi et al. 2002). We refine the geometric distortion and World Coordinate System (WCS) information using the SCAMP software (Bertin 2006). The Two Micron All Sky Survey (Skrutskie et al. 2006, 2MASS;) catalog was

Table 2
Merging Cluster Collaboration radio-relic selected Subaru SuprimeCam survey.

Cluster	Filter	Date	Seeing (arcsec)	Exposure (s)
1RXS J060313.4+421231	g	2014 February 25	0.57	720
1RXS J060313.4+421231	r	2014 February 25	0.57	2880
1RXS J060313.4+421231	i	2014 February 25	0.50	720
Abell 523	g	2014 February 26	1.00	720
Abell 523	r	2014 February 26	0.78	2880
Abell 746	g	2014 February 26	0.88	720
Abell 746	r	2014 February 26	1.01	2880
Abell 1240	g	2014 February 25	0.67	720
Abell 1240	r	2014 February 25	0.58	2880
Abell 1300	g	2014 February 26	0.89	720
Abell 1300	r	2014 February 26	0.88	2160
Abell 2061	g	2013 July 13	0.68	720
Abell 2061	r	2013 July 13	0.67	2520
Abell 2061	i	2013 July 13	0.60	2676
Abell 2061	i	2014 February 26	0.65	720
Abell 3365	g	2014 February 25	0.97	720
Abell 3365	r	2014 February 25	0.71	2880
Abell 3365	i	2014 February 25	0.62	720
Abell 3411	g	2014 February 25	0.80	720
Abell 3411	r	2014 February 25	0.82	2880
Abell 3411	i	2014 February 25	0.77	720
CIZA J2242.8+5301	g	2013 July 13	0.63	720
CIZA J2242.8+5301	i	2013 July 13	0.55	3400
MACS J175201.5+444046	g	2013 July 13	0.62	720
MACS J175201.5+444046	r	2013 July 13	0.64	1440
MACS J175201.5+444046	i	2013 July 13	0.63	2520
MACS J175201.5+444046	i	2014 February 26	0.73	1260
PLCKESZ G287.0+32.9	g	2014 February 26	0.81	720
PLCKESZ G287.0+32.9	r	2014 February 26	0.97	2880
PSZ1 G108.18-11.53	g	2015 September 12	0.65	1440
PSZ1 G108.18-11.53	r	2015 September 12	0.55	2520
RXC J1053.7+5452	g	2014 February 26	0.83	720
RXC J1053.7+5452	r	2014 February 26	0.92	720
RXC J1314.4-2515	g	2014 February 25	0.86	720
RXC J1314.4-2515	r	2014 February 25	0.71	2880
RXC J1314.4-2515	NB814	2014 February 25	0.77	1000
ZwCl 0008.8+5215	g	2013 July 13	0.52	720
ZwCl 0008.8+5215	r	2013 July 13	0.57	2880
ZwCl 1447+2619	g	2014 February 26	0.91	720
ZwCl 1447+2619	r	2014 February 26	0.76	2880
ZwCl 1447+2619	i	2014 February 26	0.55	720
ZwCl 1856+6616	g	2015 September 12	0.70	720
ZwCl 1856+6616	r	2015 September 12	0.65	2520
ZwCl 2341+0000	g	2013 July 13	0.49	720
ZwCl 2341+0000	r	2013 July 13	0.50	2880

selected as a reference when the SCAMP software was run except for clusters covered by the Sloan Digital Sky Survey (SDSS [Adelman-McCarthy et al. 2007](#)), for which the Data Release 5 catalogs were used. We also rely on SCAMP to calibrate out the sensitivity variations across different frames. For image stacking, we ran the SWARP software ([Bertin et al. 2002](#)) using the SCAMP result as input. We first created median mosaic images and then used it to mask out pixels (3σ outliers) in individual frames. These masked frames were weight-averaged to generate the final mosaic, which is used for the scientific analyses hereafter. Two example images are presented in Figure 2.

3.1.2. Subaru SuprimeCam: Photometric catalog generation

Object detection is achieved with Source Extractor ([Bertin & Arnouts 1996](#)) in dual image mode using the

deepest image for detection. The blending threshold parameter BLEND-NTHRESH is set to 32 with a minimal contact DEBLEND_MINCONT of 10^{-4} . We employ reddening values from [Schlafly & Finkbeiner \(2011\)](#) to correct for dust extinction, which are listed in Tables 2 and 3. Zero points were transferred from SDSS for the overlapping clusters and transferred to the clusters outside the SDSS footprint accounting for atmospheric extinction related to the airmass differences of our observations. Atmospheric extinction values for Mauna Kea were taken from [Buton et al. \(2013\)](#).

Since the sample has relatively low redshift, it is expected for cluster members to have high S/N and correspondingly good photometry. We enforce that potential cluster member objects have uncertainties in their magnitudes of less than 0.5 magnitudes, and we remove all objects brighter than the BCG, which we have identified

Table 3
Archival imaging from Subaru SuprimeCam utilized in this study.

Cluster	Filter	Date	Exposure (s)
Abell 115	V	2003 September 25, 2005 October 03	1530
Abell 115	i	2005 October 03	2100
Abell 521	V	2001 October 14	1800
Abell 521	R	2001 October 15	1620
Abell 781	V	2010 March 14, 15	3360
Abell 781	i	2010 March 15	2160
Abell 2034	g	2005 April 11	720
Abell 2034	R	2005 April 11, 2007 June 19	12880
Abell 2163	V	2009 April 30	2100
Abell 2163	R	2008 April 07	4500
Abell 2255	B	2007 August 14	1260
Abell 2255	R	2007 August 14	2520
Abell 2345	V	2010 June 10, 2010 November 10	3600
Abell 2345	i	2005 October 03	2100
Abell 2744	B	2013 July 16	2100
Abell 2744	R	2013 July 15	3120
MACS J1149	V	2003 April 05	2520
MACS J1149	R	2003 April 05, 2005 March 05, 2010 March 18	5490



Figure 2. Example Subaru SuprimeCam images of the central regions of A2061 (left) and A2744 (right). A2061 is displayed using our g, r, and i band images while A2744 is displayed using archival B, R, and Z images. Note that the i-band image for A2061 and the Z-band image for A2744 were used only to make these true-color images. These images were combined using the trilogy software ([Coe et al. 2012](#)).

spectroscopically in each cluster. These cuts eliminate most bright foreground galaxies and stars as well as false detections at extremely faint magnitudes. Only objects within R_{200} (as determined from our redshift analysis and scaling relations [Evrard et al. 2008; Duffy et al. 2008](#)) of the center of the cluster are retained. This limits the vignetting of the edges as well as removes spurious detections near the edge of the field; however, for the lowest redshift clusters in the sample ($z \lesssim 0.1$) R_{200} is larger than the SuprimeCam field.

3.2. Keck DEIMOS Observations

We conducted a spectroscopic survey utilizing the DEIMOS multi-object spectrograph ([Faber et al. 2003](#)) on the Keck II telescope at the W. M. Keck Observatory on Mauna Kea over the following nights: 26 January 2013, 14 July 2014, 5 September 2014, 3-5 December 2013 (half nights), 22-23 June 2014, 15 February 2015, and 13 December 2015. In total 74 slit masks were observed with 52 covering the clusters studied in this paper. All observing runs were taken with 1'' wide slits with the $1200 \text{ line mm}^{-1}$ grating resulting in a pixel scale of $0.33 \text{ \AA pixel}^{-1}$ and a resolution of $\sim 1 \text{ \AA}$ (50 km s^{-1}). For clusters with a redshift below 0.3, the grating was tilted

to observe the following spectral features: H β , [O III] 4960 & 5008, Mg I (b), Fe I, Na I (D), [O I], H α , and the [N II] doublet (Figure 3). A typical wavelength coverage of 5400 Å to 8000 Å is shown in Figure 3 for a galaxy observed in CIZAJ2242. The actual wavelength coverage may be shifted by $\sim \pm 400$ Å depending where the slit is located along the width of the slitmask. This spectral setup enables us to also study the star formation properties of the cluster galaxies; see related work by Sobral et al. (2015). For higher redshift clusters (above 0.3), the grating was tilted to instead cover the following spectra features: [O II] 3727, Ca(H), Ca(K), H δ , G-band, H γ , H β , and [O III] 4960 & 5008. The position angle (PA) of each slit was chosen to lie between $\pm 5^\circ$ to 30° of the slitmask PA to achieve optimal sky subtraction during reduction with the DEEP2 version of the spec2d package (Newman et al. 2013). In general, for each mask we took three ~ 900 s exposures except for a few cases where a few extra minutes at the end of the night were spent on an individual mask or when weather altered our observation plans in the middle of the night. In total, 52 slitmasks were observed with a total of ~ 6500 slits over the course of the spectroscopic survey of the radio relic sample of merging clusters.

3.2.1. Keck DEIMOS: Target Selection

Our primary objective for the spectroscopic survey was to maximize the number of cluster member spectroscopic redshifts in order to detect merging substructure within R_{200} . For each slitmask, the best imaging data available were utilized. For one third of the clusters this was our own SuprimeCam imaging from our simultaneous wide field imaging survey (see §3.1). In the cases where this was unavailable at the time of our spectroscopic survey planning, we used the next best imaging at our disposal. SDSS Data Release 12 catalogs were utilized (Alam et al. 2015) for ten of the clusters, and for six of the clusters, this was INT WFC data presented in (van Weeren et al. 2011d). For the remaining two clusters, Digitized Sky Survey (DSS: Djorgovski et al. 1992) imaging was utilized. For all imaging except the SDSS data, for which a photometric redshift selection was employed, a red sequence technique was utilized to select likely cluster members to create a galaxy number density map. The slit masks were then oriented to maximize the number of cluster members in the high red sequence density regions. Priors from the literature were also utilized in the placement of slitmasks (e.g. lensing maps, X-ray surface brightness, radio relics, etc.).

The DEIMOS $5' \times 16.7'$ field-of-view (FOV) is very well suited to survey the low-z, elongated merging systems in our sample. In most cases, we aligned the long axis of our slitmasks with the long axis of the system. The success of star-galaxy separation in our targeting data was variable and depended on the seeing of the imaging; thus, several of our slitmasks were highly contaminated with stars. For example, for CIZAJ2242, which sits near the plane of the galaxy, has a stellar density nearly three times that of cluster members. When selecting targets, we divided our potential targets into a bright red sequence sample (Sample 1; $r < 22.5$) and a faint red sequence sample (Sample 2; $22.5 < r < 23.5$). We first filled our mask with as many Sample 1 targets

as possible, then filled in the remainder of the mask with Sample 2 targets. While we preferentially targeted likely red sequence cluster members it was not always possible to fill the entire mask with these galaxies, in which case we would place a slit on bright blue cloud galaxies in the field. For the SDSS targeted galaxies, we selected from galaxies with a photometric redshift within $\pm 1.05(1+z)$ of the cluster redshift and prioritized bright galaxies with a luminosity weighted selection. In these cases, Sample 2 was composed of any other bright objects outside the photometric selection.

We used the DSIMULATOR package⁵ to design each slitmask. DSIMULATOR automatically selects targets by maximizing the sum total weights of target candidates, by first selecting as many objects from Sample 1 as possible then filling in the remaining area of the slitmask with target candidates from Sample 2. We manually edited the automated target selection to increase the number of selected targets, e.g. by selecting another target between targets selected automatically by DSIMULATOR if it resulted in a small loss of sky coverage.

3.2.2. Keck DEIMOS: Data Reduction

The exposures for each mask were combined using the DEEP2 versions of the *spec2d* and *spec1d* packages (Newman et al. 2012b). This package combines the individual exposures of the slit mosaic and performs wavelength calibration, cosmic ray removal and sky subtraction on slit-by-slit basis, generating a processed two-dimensional spectrum for each slit. The *spec2d* pipeline also generates a processed one-dimensional spectrum for each slit. This extraction creates a one-dimensional spectrum of the target, containing the summed flux at each wavelength in an optimized window. The *spec1d* pipeline then fits template spectral energy distributions (SED's) to each one-dimensional spectrum and estimates a corresponding redshift. There are SED templates for various types of stars, galaxies, and active galactic nuclei. We then visually inspect the fits using the *zspec* software package (Newman et al. 2013), assign quality rankings to each fit (following a convention closely related to Newman et al. 2013), and manually fit for redshifts where the automated pipeline failed to identify the correct fit. The highest quality galaxy spectra ($Q=4$) have a mean signal-to-noise-ratio (SNR) of 10.7 per pixel, while the minimum quality galaxy spectra used on our redshift analysis ($Q=3$) have a mean SNR of 4.9 per pixel. Note that the SNR estimates are dominated by the continuum of a spectroscopic trace and an emission line galaxy may be of high quality but very low mean SNR (for example the mean SNR of a $Q=4$ emission line galaxy is 1.2 despite detection of H α and H β or [O III] in most cases). An example of one of the reduced spectra is reprinted from Figure 2 of Dawson et al. (2015) in Figure 3 and more are shown in a related galaxy evolution paper Sobral et al. (2015).

3.2.3. Keck DEIMOS: spectroscopic catalog generation

We combine all known redshifts (from NED, the literature, and our DEIMOS survey) in the cluster fields and check for duplicates using the Topcat (Taylor 2005) software using the *sky* function with a 1'' tolerance. We cut

Table 4
Merging Cluster Collaboration radio-relic selected spectroscopic survey.

Slitmask	Date	Target	Imaging	Exposure (s)	Wavelength (Å)	Slits
1RXSJ0603-1	2013 January 16	WFC		3000	6200	105
1RXSJ0603-2	2013 January 16	WFC		3000	6200	100
1RXSJ0603-3	2013 September 5	WFC		3600	7000	98
1RXSJ0603-4	2013 September 5	WFC		3600	7000	87
A115-1	2014 June 22	SDSS		2500	6900	176
A115-2	2014 June 23	SDSS		2400	6900	142
A523-1	2013 January 16	WFC		3000	6200	99
A523-2	2013 December 4	WFC		2700	6200	94
A523-3	2015 February 16	WFC		2700	6300	111
A746-1	2013 January 16	SDSS		3600	6200	110
A1240-1	2013 December 3	SDSS		2700	6850	120
A1240-2	2015 February 16	SDSS		2700	6820	164
A1612-1	2015 February 16	SDSS		1200	6750	140
A2034-1	2013 July 14	SDSS		2700	6700	158
A2443-1	2014 June 22	SDSS		2400	6400	153
A2443-2	2014 June 23	SDSS		2400	6400	163
A3365-1	2013 January 16	WFC		2700	6200	68
A3365-2	2013 January 16	WFC		2400	6200	66
A3365-3	2013 December 3	WFC		2700	6300	63
A3365-4	2013 December 4	WFC		2700	6300	66
A3365-5	2015 February 16	SC		2700	6200	160
A3411-1	2013 December 3	WFC		2700	6650	132
A3411-2	2013 December 3	WFC		2700	6650	127
A3411-3	2013 December 4	WFC		2700	6650	128
A3411-4	2013 December 4	WFC		2700	6650	131
A3411-5	2015 December 13	SC		3600	6650	142
CIZAJ2242-1	2013 July 14	WFC		2700	6700	148
CIZAJ2242-2	2013 July 14	WFC		2700	6700	126
CIZAJ2242-3	2013 September 5	SC		2700	7000	90
CIZAJ2242-4	2013 September 5	SC		2700	7000	106
MACSJ1752-1	2013 July 14	SDSS		2700	6700	155
MACSJ1752-2	2013 July 14	SDSS		2700	6700	119
MACSJ1752-3	2013 September 5	SDSS		3600	7000	114
MACSJ1752-4	2013 September 5	SDSS		2700	7000	118
PLCKG287-1	2015 February 16	SC		3900	7950	207
PLCKG287-2	2015 February 16	SC		2700	7950	185
PLCKG287-3	2015 February 16	SC		2700	7950	193
PSZ1G108-1	2014 June 22	DSS		1800	7400	198
PSZ1G108-2	2014 June 23	DSS		1800	7650	168
RXCJ1053-1	2013 January 16	SDSS		2803	6200	113
RXCJ1053-2	2013 December 3	SDSS		2700	6200	84
RXCJ1053-3	2013 December 4	SDSS		2430	6200	98
RXCJ1053-4	2015 February 16	SC		2700	6200	141
RXCJ1314-1	2015 February 16	SC		2520	7120	196
RXCJ1314-2	2015 February 16	SC		2520	7120	207
ZwCl0008-1	2013 January 16	WFC		2063	6200	81
ZwCl0008-2	2013 July 14	WFC		2700	6700	81
ZwCl0008-3	2013 September 5	WFC		2700	7000	75
ZwCl0008-4	2013 September 5	WFC		3600	7000	73
ZwCl1447-1	2014 June 22	SDSS		1520	7850	149
ZwCl1447-2	2014 June 23	SDSS		1053	7850	138
ZwCl1856-1	2014 June 22	DSS		1800	7400	150
ZwCl1856-2	2014 June 23	DSS		1800	7400	101
ZwCl2341-1	2013 July 14	SDSS		2700	6700	130
ZwCl2341-2	2013 July 14	SDSS		2700	6700	131
ZwCl2341-3	2013 September 5	SDSS		2700	7000	148

each spectroscopic catalog to only include objects within R_{200} in projected space and to within $\bar{v} \pm 3\sigma_v$, where \bar{v} is the average line of sight velocity and σ_v is the cluster velocity dispersion. This is accomplished with an iterative process starting with 5 Mpc and 10,000 km s $^{-1}$ and shrinking the radius and velocity window until an equilibrium catalog is achieved.. This reduces the chance of

inclusion of galaxies that are uninvolved in the merger. For example, Abell 2067 is ~ 2.7 Mpc (30') from Abell 2061, which is a merging cluster and in our sample; however, the iterative shrinking aperture was able to eliminate this galaxy cluster from the redshift catalog despite being at a similar redshift because it is outside of R_{200} . Furthermore, Abell 523 ($z \sim 0.1$) has two background

[t!]

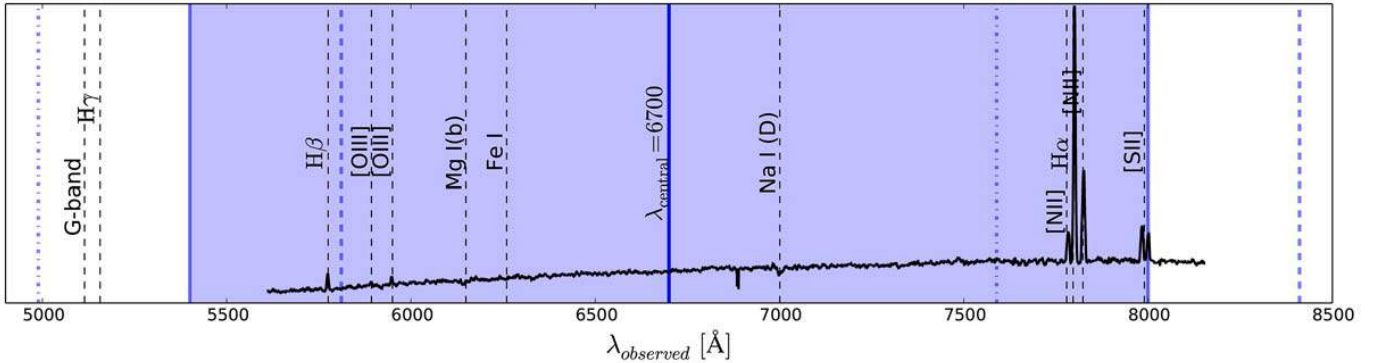


Figure 3. Reprinted Figure 2 of Dawson et al. (2015). Example spectral coverage of the Keck DEIMOS observations (shaded blue region) for a low redshift ($z \lesssim 0.3$) cluster, along with the redshifted location of common cluster emission and absorption features (black dashed lines). The blue dot-dash pair and the blue dashed pair of lines show the variable range depending on where the slit was located along the width of the slitmask. The solid black line shows an example galaxy spectrum from our DEIMOS survey.

groups at $z \sim 0.14$ within R_{200} in projection (Girardi et al. 2016); however, the line of sight velocity difference is large enough to eliminate those spectra from the spectroscopic catalog. In specific cases, we estimate the redshift and velocity dispersion of nearby clusters that we have substantial spectroscopic coverage.

4. RADIO WAVES AND X-RAYS

The primary selection function for this ensemble of merging clusters is the presence of confirmed radio relics. The radio data utilized by the literature in order to confirm these features is quite diverse, and in this section we summarize this aspect of our ensemble. We also detail the archival X-ray data and discuss the additional advantages that X-ray surface brightness maps and radio relics offer when interpreting merger scenarios.

In Table 5, we detail the radio and X-ray data that will be presented in this paper. The radio data are presented in the form of linearly spaced contours on many figures that follow. The wide field radio images were cut down to only display the radio relics using the `ftcopy` function from ftools (Blackburn 1995). All data were shared generously by the authors of the various studies listed in Table 5. Readers are referred to those studies for details regarding observations, data reduction, and analyses.

Radio relics are defined as peripheral, diffuse radio features covering regions several hundred kpc in projection. Most radio relics are unassociated with optical counterparts; although, recent observations have directly imaged the connection of a passing shock causing a radio relic lead to a radio jet from a cluster member AGN (van Weeren et al. 2017).

The spectral index of radio relic emission across frequencies from tens of MHz to several GHz can be used to estimate the Mach number of the underlying shock:

$$\mathcal{M} = v_{\text{shock}}/c_s = \sqrt{\frac{2\alpha_{\text{inj}} + 3}{2\alpha_{\text{inj}} - 1}} \quad (1)$$

where c_s is the sound speed in the upstream medium and α_{inj} is the injection spectral index. Mach numbers are frequently measured to be $\mathcal{M} \sim 2 - 4$ assuming diffusive shock acceleration (DSA: Drury 1983). The radio data presented here by no means exhaust the utility of

radio analyses of galaxy clusters in terms of constraining the dynamics. As mentioned in §1, the polarization may be used to constrain the viewing angle of the merger axis, and the spectral steepening is a clear demonstration of the motion of the subclusters and shocks through the ICM. Radio observations of galaxy cluster mergers may well result in observational understanding of cosmic ray generation, a deeper understanding of shock propagation, turbulence, microphysics within the Mpc scale ICM in terms of plasma instabilities, as well as a better understanding of the timescale of radio plasma from AGN and the interplay between these galaxies and the variety of observed radio relic morphologies.

Also displayed in Table 5 are the archival X-ray data from Chandra Space Telescope (ACIS) , XMM-Newton (EPIC), and the ROSAT All-Sky Survey. These X-ray images represent the best publicly available data for each cluster. Chandra images were downloaded from the archive and reduced with the `chav` package following the process described in Vikhlinin et al. (2005) using CALDB 4.6.5. The calibration includes the application of gain maps to calibrate photon energies, filtering of counts with ASCA grade 1, 5, or 7 and from bad pixels, and a correction for the position-dependent charge transfer inefficiency. Periods with count rates a factor of 1.2 above the mean count rate in the 6–12 keV band were also removed. Standard blank sky files were used for background subtraction. The final exposure corrected image was made in the 0.5–2.0 keV band using a pixel binning of a factor of four.

For the XMM images, the data were reduced using version 16.0 of the Extended Source Analysis Software (ESAS) pipeline following the example reduction of Abell 1795 in the ESAS cookbook⁶. In particular, raw event files were created from the Observation Data Files (ODF) using the `emchain` and `epchain` routines. The data were filtered of flaring from soft protons using the `mos-filter` and `pn-filter` routines. These apply a 1.5σ cutoff from a Gaussian fitted to the light curve. Point sources above a flux threshold of 3×10^{-15} erg cm $^{-2}$ s $^{-1}$ were masked out using the `cheese` routine. Spectra and images were extracted using `mos-spectra` and `pn-spectra`. The data

Table 5
Ancillary radio images utilized in this paper

Cluster	Radio Image	Radio Reference	X-ray Telescope	X-ray Exposure (ks)
1RXS J0603	GMRT 610 MHz	van Weeren et al. (2012b)	Chandra	250
A115	VLA 1.4 GHz	Govoni et al. (2001b)	Chandra	360
A521	GMRT 240 MHz	Venturi et al. (2013)	Chandra	170
A523	VLA 1.4 GHz	van Weeren et al. (2011b)	XMM	230
A746	WSRT 1382 MHz	van Weeren et al. (2011b)	Chandra	30
A781	GMRT 325 MHz	Venturi et al. (2013)	Chandra	48
A1240	VLA 1.4 GHz	Bonafede et al. (2009)	Chandra	52
A1300	GMRT 325 MHz	Venturi et al. (2013)	Chandra	100
A1612	GMRT 325 MHz	van Weeren et al. (2011b)	Chandra	31
A2034	WSRT 1382 MHz	van Weeren et al. (2011b)	Chandra	261
A2061	WSRT 1382 MHz	van Weeren et al. (2011b)	Chandra	32
A2163	VLA 1.4 GHz	Feretti et al. (2001)	Chandra	90
A2255	WSRT 350 MHz	Pizzo & de Bruyn (2009)	XMM	42
A2345	VLA 1.4 GHz	Bonafede et al. (2009)	XMM	93
A2443	VLA 325 MHz	Cohen & Clarke (2011)	Chandra	116
A2744	GMRT 325 MHz	Venturi et al. (2013)	Chandra	132
A3365	VLA 1.4 GHz	van Weeren et al. (2011b)	XMM	161
A3411	GMRT 325 MHz	van Weeren et al. (2017)	Chandra	215
CIZA J2242	WSRT 1382 MHz	van Weeren et al. (2010)	Chandra	206
MACS J1149	GMRT 323 MHz	Bonafede et al. (2012)	Chandra	372
MACS J1752	WSRT 1.4 GHz	van Weeren et al. (2012a)	XMM	13
PLCK G287	GMRT 325 MHz	Bonafede et al. (2014)	Chandra	200
PSZ1 G108	GMRT 323 MHz	de Gasperin et al. (2015)	Chandra	27
RXC J1053	WSRT 1382 MHz	van Weeren et al. (2011b)	Chandra	31
RXC J1314	VLA 2-4 GHz	N/A	XMM	110
ZwCl 0008	WSRT 1382 MHz	van Weeren et al. (2011c)	Chandra	411
ZwCl 1447	VLA 1.4 GHz	Govoni et al. (2012)	RASS	21
ZwCl 1856	WSRT 1382 MHz	de Gasperin et al. (2014)	XMM	12
ZwCl 2341	GMRT 610 MHz	van Weeren et al. (2009b)	Chandra	227

were then background subtracted using the XMM-ESAS CalDB files⁷ and the `mos-back` and `pn-back` routines. CCD #6 became unoperational in 2005, and is automatically excluded by XMM-ESAS for relevant observations.

For ZwCl 1447, no XMM-Newton or Chandra data are available, so the cluster's emission detected by the ROSAT All-sky Survey (Voges et al. 1999) is presented. ZwCl 1447 appeared in exposure 931236. The presented image background subtracted and exposure corrected; however, the number of counts is much lower for this image compared with the rest of the sample. In this paper, these X-ray images are presented as X-ray surface brightness maps, which help in the inference of the merger scenarios, and in a few cases clear up which of several subclusters have merged and which have not. We discuss these more in §5.6 and §6.

X-ray data analysis is similarly rich as radio data analysis. In the context of merging clusters, bulk motion of the ICM such as cold fronts and cool-core survival is studied. Furthermore, in sufficiently deep Chandra exposures, the data are spatially sensitive enough to directly measure the emission profile near radio relics and measure shock properties. XMM-Newton has less spatial resolution; however, its spectral capabilities allow for the detection of shocks in the form of temperature and density jumps between extracted regions on either side of a proposed shock. Shocks have been detected in several clusters (e.g. Markevitch et al. 2002; Russell et al. 2010). Original interpretations of the shock speed from the Mach number suggested that the Bullet Cluster per-

haps merged too fast for Λ CDM (e.g. Markevitch et al. 2002; Hayashi & White 2006, among others). This controversy was resolved when it was noted that the inferred shock speed includes the relative motion of infalling gas (Springel & Farrar 2007).

However, shocks still spawn controversy when comparing inferred Mach numbers from X-ray and radio data. Several examples of discrepancy have been uncovered. For example, in the famous “toothbrush” relic in 1RXSJ0603, the radio analysis indicates a Mach number of $2.8_{-0.3}^{+0.5}$ (van Weeren et al. 2016) versus $\mathcal{M} \lesssim 1.5$ from the X-rays (Ogurain et al. 2013c). If the X-ray measured Mach numbers are taken at face value, DSA seems unable to explain the observed radio relic brightnesses. Presently, the leading explanation in the literature suggests that DSA can explain radio relics only if the passing shocks are creating bright emission by reaccelerating a pre-accelerated (and now cooled) semi-relativistic population of plasma. One such source of pre-accelerated plasma could very well be radio galaxies in the cluster. (van Weeren et al. 2017) found direct evidence for such a connection in Abell 3411; however, detections of specific connections remain rare. Further evidence of this picture is emerging from the new Low-Frequency Array (LOFAR), which has been used to show several low-frequency diffuse sources in A2034 (Shimwell et al. 2016). The observation of a radio relic and AGN in A3411 presents a clear example of this phenomenon. Future radio surveys of merging clusters seem poised to uncover more examples.

5. ANALYSIS TOOLS

In this section, we will describe the steps of analysis starting with photometric and spectroscopic galaxy catalogs from our optical and multi-object spectroscopy observations discussed previously. The analysis has been tailored for our sample analysis but is largely based on the analyses presented in Dawson et al. (2015); Golovich et al. (2016, 2017); van Weeren et al. (2017); Benson et al. (2017) which study five clusters from this sample: CIZAJ2242, MACSJ1149, ZwCl0008, A3411, and ZwCl2341, respectively. The following subsections describe individual analysis steps using 1RXSJ0603 or RXCJ1053 as informative examples for the figures that follow. The details for individual clusters vary and are discussed in the corresponding subsections of §6.

5.1. One dimensional redshift analysis

We display the one dimensional redshift distribution for 1RXSJ0603 in Figure 4. An analogous figure for the remaining 28 systems is presented in Figure 5. The corresponding normalized Gaussian distribution is overlaid with the cluster redshift and velocity dispersion given by the biweight and bias corrected 68% confidence intervals. We implement the biweight statistic based on 10,000 bootstrap samples of each cluster’s member galaxies and calculate the bias-corrected 68% confidence limits for the redshift and velocity dispersion from the bootstrap sample. This method is more robust to outliers than the dispersion of the Gaussians generated by our statistical model (Beers et al. 1990). We also test the goodness of fit of the corresponding Gaussian distribution using a Kolmogorov-Smirnov (KS) test, and the results are also displayed in the panels. We generally find good agreement between the spectroscopic data and single Gaussian distributions, which implies that the merging subclusters have line of sight velocity differences that are small compared to the velocity dispersion. The lowest p-value for the KS test is 0.007 for Abell 781, which is known to be composed of several subclusters with large velocity differences. In the bottom row of Figure 5, the full spectroscopic sample is presented across the redshift range of the clusters in our sample. The corresponding Gaussians from the individual panels are translated to this figure, which depicts the global redshift distribution of the ensemble.

5.2. Galaxy Density Maps

We match objects from the spectroscopic and photometric catalogs using the Topcat (Taylor 2005) software using the sky coordinate match with $1''$ tolerance. We define the color of the objects by selecting the two filters that most evenly straddle the 4000 \AA break. Objects with large photometric errors (>0.5 magnitudes) are eliminated from the catalog. Stars are eliminated via size-magnitude cuts. Stars follow a clear relation and easily eliminated from galaxies. An example size-magnitude diagram is presented in Figure 6.

The red sequence selection is performed by overlaying the spectroscopically confirmed cluster members in a color-magnitude diagram. The width of the red sequence depends on several factors including redshift, dynamical activity, early/late type galaxy population, etc., but to regularize the analysis, we restrict the red sequence width to 0.5 magnitudes along the color axis, and

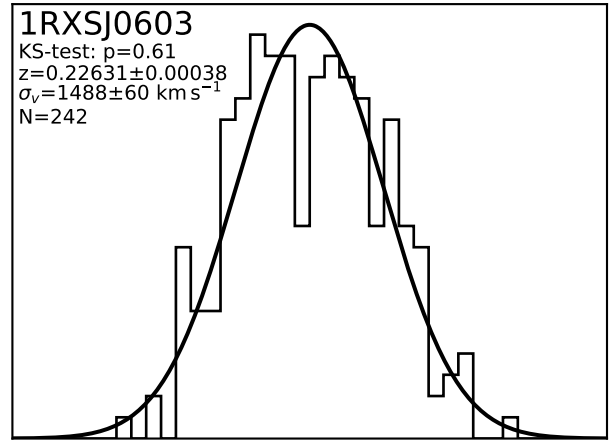


Figure 4. Redshift distribution for 1RXSJ0603 based on our DEIMOS spectroscopic survey. Galaxies are selected with a shrinking 3D aperture until a stable set of galaxies within R_{200} and $\pm 3\sigma_v$ is achieved. The global redshift analysis using the biweight statistic and bias corrected 68% confidence limits are presented in the panel. The p-value for a KS-test for Gaussianity is presented as well. The panel width is $12,000\text{ km s}^{-1}$ centered on the cluster redshift. Bins are 300 km s^{-1} at the cluster redshift. The analogous distribution for the other 28 systems in our sample are located in Figure 5.

length to six magnitudes greater than the BCG, which we find sufficient to capture nearly all targeted red sequence galaxies. We eliminated contaminant stars and non-cluster member galaxies from the red sequence catalogs by cross checking the photometric catalog with the Subaru SuprimeCam images and our spectroscopic catalog. In a few cases SExtractor objects were artificially bright due to proximity to stellar bleeds and diffraction spikes. These objects were eliminated from the red sequence catalogs as well.

A clear and tight red sequence is visible in color-magnitude diagrams, such as the one for RXCJ1053 which is presented in Figure 7. For galaxies that were targeted for spectroscopic observations using a red sequence method, the spectroscopic points will largely fall within the red sequence region; whereas, for galaxies targeted using SDSS photometric redshifts, the blue cloud galaxies will be more completely sampled. In the case of RXCJ1053, a photometric redshift selection was implemented based on SDSS imaging, which is evident from the green points below the clear red sequence.

Typical red sequence populations range between 500 and 2500 galaxies depending on the richness, redshift, and depth of the optical image. We display the information via smoothed density maps weighted by luminosity in the reddest filter (typically r or i). We choose the smoothing bandwidth via a take one out, maximum likelihood, cross-validation, kernel density estimation (KDE) analysis. The KDE bandwidths range from $25''$ to $100''$ roughly proportional to the redshift. The optimal KDE bandwidths for each cluster are displayed on the DS-test plots described in §5.3.

5.3. Dressler-Schechtman Test

The Dressler-Schechtman (DS)-test is performed by computing a statistic for local velocity information as compared to the global values (Dressler & Schechtman

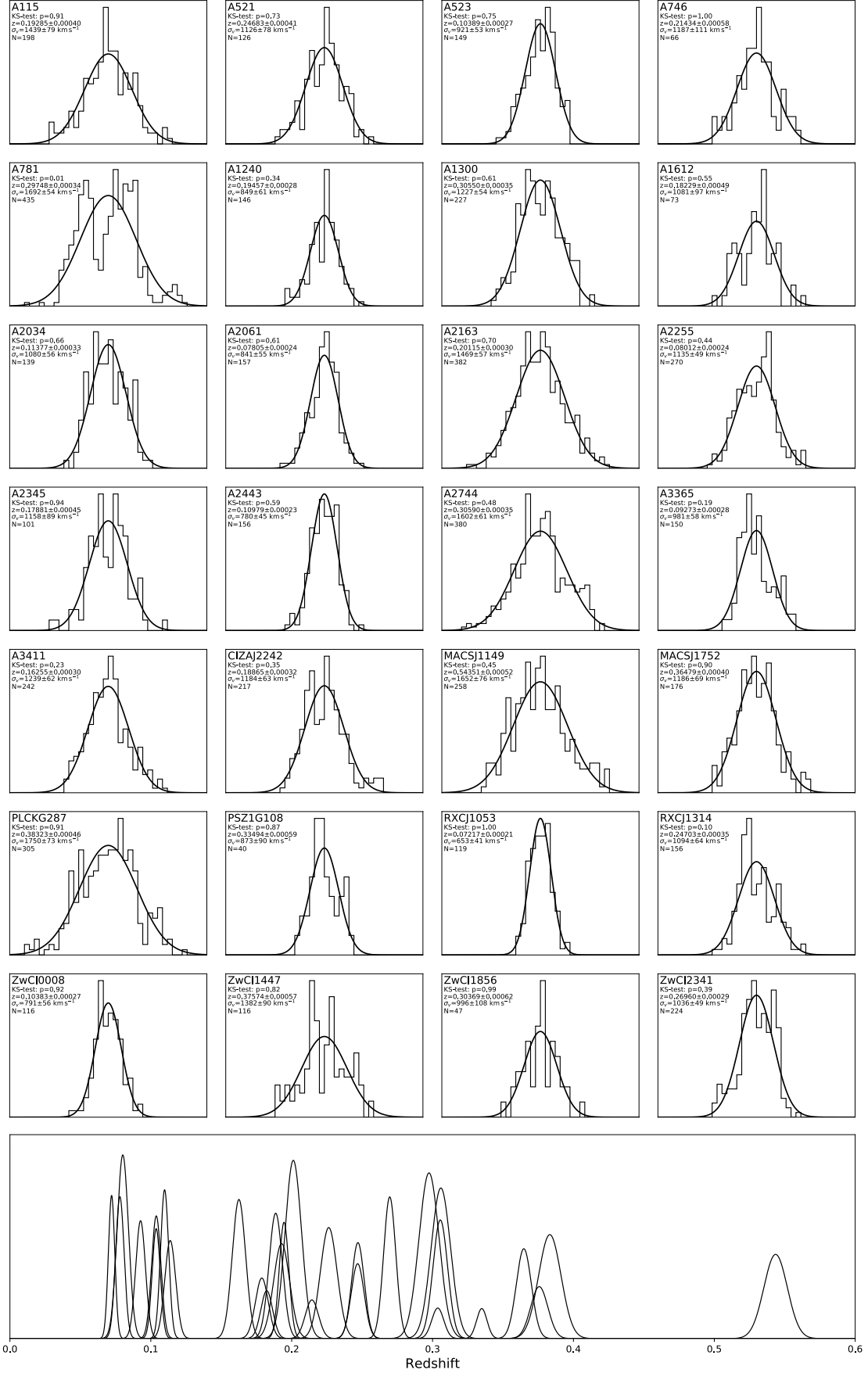


Figure 5. Redshift distribution for 28 merging galaxy clusters. Each panel is analogous to Figure 4. The bottom figure is based on all ~ 5500 spectroscopic cluster members for the 29 merging clusters in our sample. The minimum redshift is for RXCJ1053 ($z \sim 0.07$), and the maximum redshift is for MACSJ1149 ($z \sim 0.54$). Since many systems were discovered to have radio relics in shallow surveys, lower redshifts are more densely populated by our ensemble.

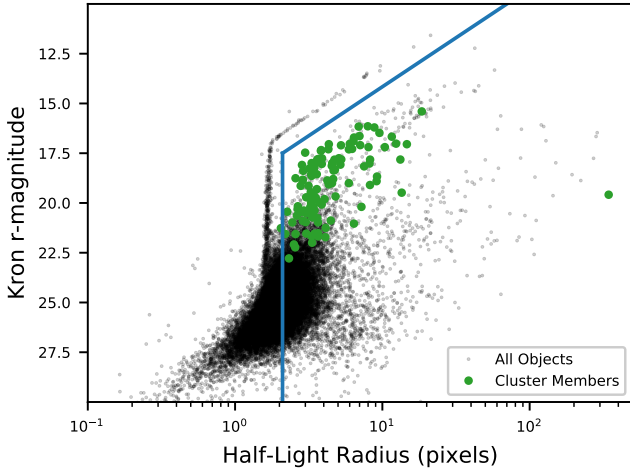


Figure 6. Size-magnitude diagram for the photometric catalog of RXCJ1053 with overlaid spectroscopic matches. The stellar trace is easily eliminated to the left and above the delineating cut (blue line). Stars are defined as less than 2.1 pixels up to $r \sim 17.5$. All objects brighter than the BCG are also eliminated.

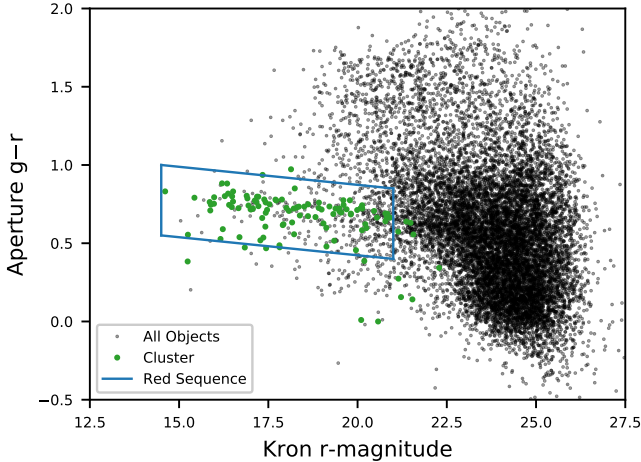


Figure 7. Color-magnitude diagram for the photometric catalog of RXCJ1053 with overlaid spectroscopic matches. The red sequence selection box is shown in blue. Magnitudes are corrected for dust extinction, and all objects that passed the size-magnitude cut are plotted.

1988). The statistic is given by:

$$\delta^2 = \frac{N_{local}}{\sigma^2} [(\bar{v}_{local} - \bar{v})^2 + (\sigma_{local} - \sigma)^2] \quad (2)$$

where N_{local} is the number of nearest neighbors (self-inclusive) to include when calculating \bar{v}_{local} , the local-average LOS velocity, and σ_{local} , the local velocity dispersion. We let $N_{local} \equiv \lceil \sqrt{N_{total}} \rceil$, where N_{total} is the number of galaxies in the full spectroscopic catalog. This follows the best practice identified by Pinkney et al. (1996). Galaxies with larger δ values are highly correlated with their neighbors and different from the global parameters thus identifying local structure.

In Figure 8, we plot the projected location of the galaxies in the spectroscopic catalog as circles with radii proportional to 10^δ over the red sequence luminosity density distribution for 1RXSJ0603. The remaining 28 DS plots are presented in Figure 9. We singled out 1RXSJ0603 as an informative example to enlarge and show the details.

We color-coded the circles in Figures 8 and 9 by redshift. This helps us infer the source of inflated δ ; groups of large circles with a narrow band of redshift indicate an interloping substructure with a line of sight velocity difference, while clustered groups with a large velocity range indicate either massive subclusters or chance alignments of high and low velocity cluster members and thus an inflated local velocity dispersion.

Plotting the DS-test over the red sequence luminosity density distribution mitigates the main fail mode of the DS-test, which is insensitivity to equal mass subclusters distributed in projected space with similar redshifts. In this scenario, the test is effectively reduced to a two dimensional test, which is a strength of the red sequence luminosity for detecting substructure. This technique also provides a check against false subcluster detections in the spectroscopic and photometric data. The spectroscopic selection with DEIMOS causes some regions to be over-sampled relative to the cluster core since DEIMOS slits were placed on as many galaxies as possible. However, since the slits may not overlap along the dispersion axis, the cluster center can't be fully sampled. Thus, small yet correlated groups of galaxies may appear as a group of very large circles in the DS-test; meanwhile, bright substructure may be under-sampled spectroscopically. For this reason, we will only assign potential subclusters to areas that are high in photometric luminosity and were covered with the spectroscopic survey. However, the photometric red sequence selection means there is contamination, so false positives are possible in the red sequence luminosity map as well. Together, high red sequence luminosity density with corresponding high δ groups are constitute strong evidence for an associated subcluster, and this combination of evidence provides the basis for our subcluster priors. As a final step, placing the radio relic contours on these diagnostic plots immediately reveals the likely merger scenarios.

5.4. Gaussian Mixture Models

We seek to fit subcluster properties quantitatively by a clustering algorithm that assigns specific spectroscopically confirmed cluster members to the subcluster that most likely hosts them. Here we describe the subclustering method that we will implement on each cluster's spectroscopic data. We will utilize a three dimensional Gaussian mixture model (GMM) analysis. The basic aim is to simultaneously fit multiple Gaussians to the projected location and redshift distribution of a population of galaxies. Standard packages have been developed for GMM methods, but these codes often fail to fit physically motivated subclusters. It is important to consider the data we are attempting to fit. Galaxy spectroscopy within a cluster environment is a discrete set of data that serve as tracer particles for the dynamics of the cluster. Yet, galaxies make up a small fraction of the total mass, and thus, informative priors can be developed based on other observations that probe the DM halo and ICM of the clusters. Several of our clusters have detailed lensing studies in the literature, and all have dedicated X-ray observations that have mapped the X-ray surface brightness of the ICM. Additionally, each cluster has at least one radio relic that traces the underlying shocks in the ICM. With all this information, we developed a scheme to include informative priors on the location and scale

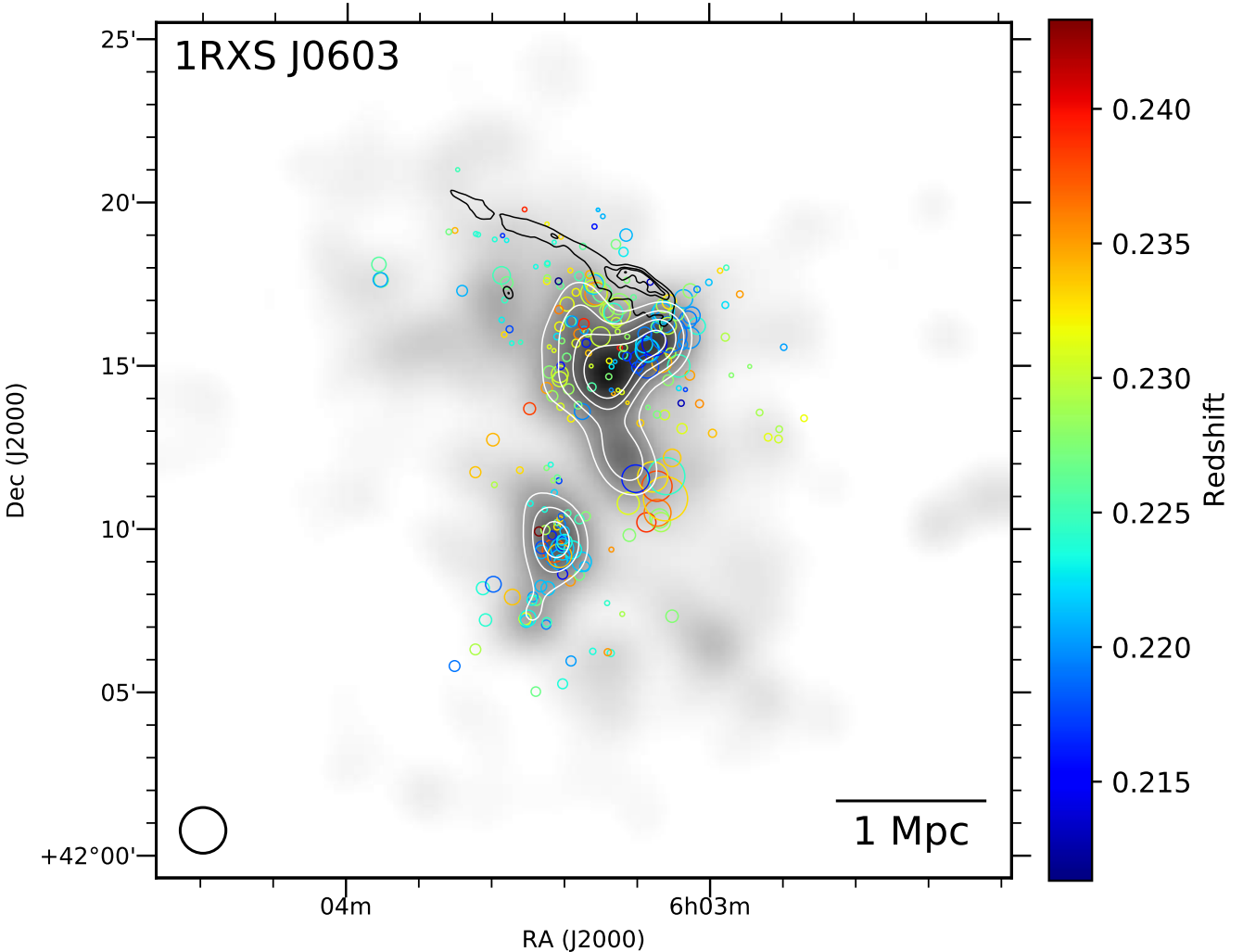


Figure 8. DS-test for 1RXSJ0603. The circles each correspond to spectroscopically confirmed cluster members and are colored according to their redshift. The size of the circles is given by 10^δ . The gray scale map corresponds to the red sequence luminosity density smoothed by the optimal KDE bandwidth, and the corresponding white contours start at 3σ above the median pixel luminosity value and increase in units of σ , where σ is the standard deviation of the pixel values within R_{200} . The smoothing scale is chosen with an optical KDE bandwidth estimation, and is displayed in the lower left. The black contours are linearly spaced and show the so-called “Toothbrush” radio relic based upon the 610 MHz WSRT image of van Weeren et al. (2012b). The field is $2R_{200} \times 2R_{200}$ based on the global velocity dispersion and scaling relations (Evrard et al. 2008).

of the component Gaussians. For these reasons, we have completed a detailed literature review for X-ray, radio, galaxy, and lensing analyses for each cluster. Priors are based upon results from the literature coupled with the DS-test and red sequence luminosity density as in Figure 8.

When determining potential subclusters, we look for areas that are at least 3σ above the median pixel value in the red sequence luminosity maps and also have spectroscopic coverage. We then run a Markov-Chain Monte Carlo (MCMC) code that fits the data to Gaussian mixture models that contain all possible combinations of the potential subclusters. We utilize the python package *emcee* (Foreman-Mackey et al. 2013) for the MCMC sampling. We do not run a model for each subcluster by itself instead running a single one halo model using the global Gaussian for the redshift information and an unin-

formative prior on the RA and DEC components. Thus if there are two potential subclusters we run two models, (1) a single halo model with the redshift Gaussian from the global velocity information as a prior and (2) a two halo model with RA and DEC priors drawn from the red sequence luminosity density map and a conservative redshift prior based on the color of the DS circles in that potential subcluster. For a system with three potential subclusters we run five GMM models, and for a system with four potential subclusters, we run twelve. In general for a system with n potential subclusters we run N total models given by Equation 3.

$$N = 1 + \sum_{k=2}^n \binom{n}{k} \quad (3)$$

We summarize all possible subclusters for all 29 sys-

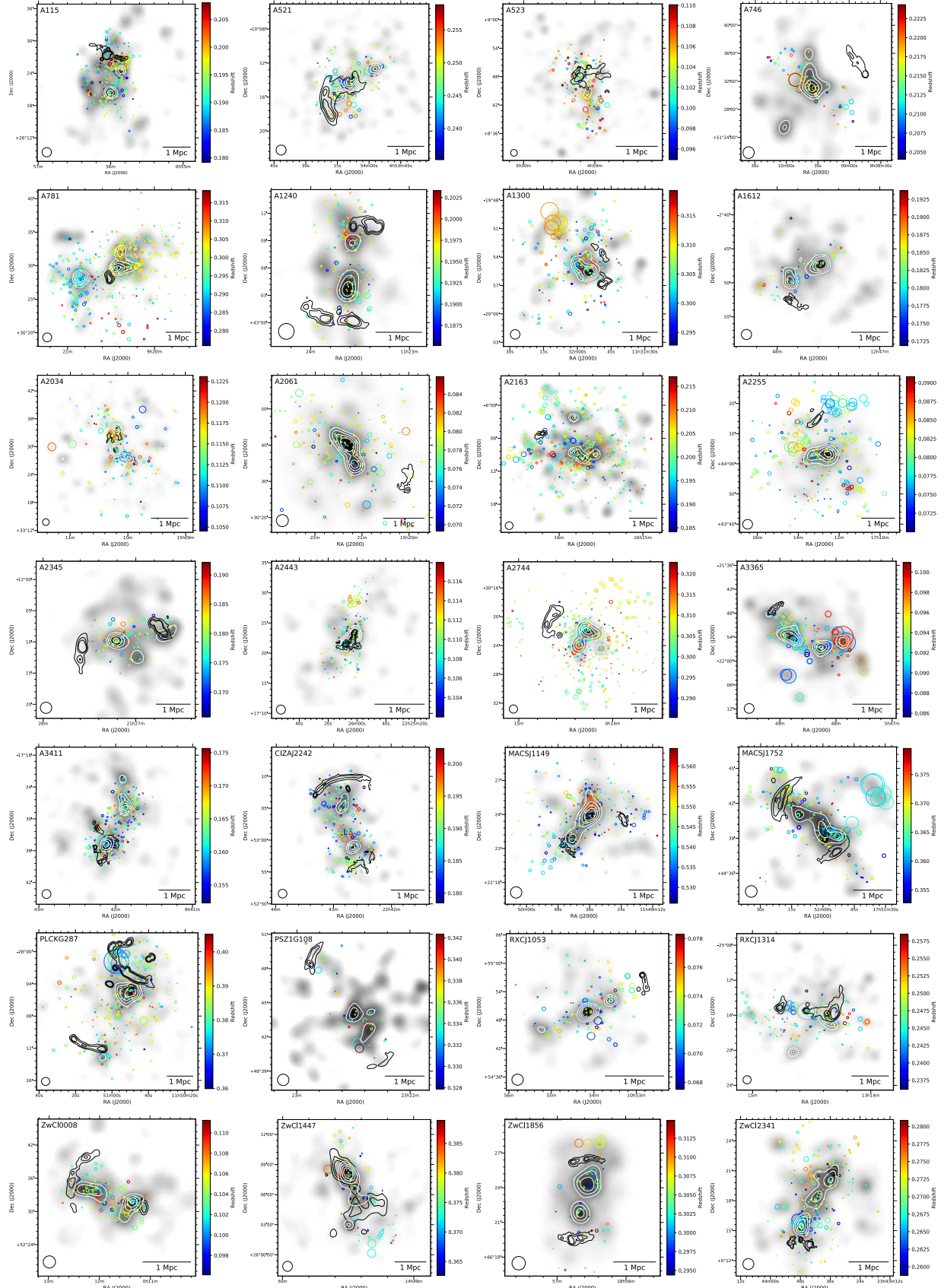


Figure 9. Analogous figures to Figure 8 for 28 merging clusters in our ensemble. The source of the radio relic contours are listed in Table 5. The red sequence luminosity distributions are derived from our Subaru SuprimeCam imaging except for A2443 (SDSS), PSZ1G108 (DSS), and ZwCl1856 (Gemini GMOS). Individual figures are available in the online version of this article.

tems in Table 6, and we detail each model run on the data for all 29 clusters in Table 7. These tables will serve as a master list that will be referred to in each subsection of §6. The number of models for each cluster is determined by the number of potential subclusters listed for a given system in Table 6 following the prescription of Equation 3.

The 3D Gaussian mixture models are defined by the means and covariance matrices. For the i^{th} Gaussian in the model, these are given by:

$$\boldsymbol{\mu}_i = \begin{pmatrix} \mu_{\alpha_i} \\ \mu_{\delta_i} \\ \mu_{z_i} \end{pmatrix} \quad (4)$$

$$\boldsymbol{\Sigma}_i = \begin{pmatrix} \sigma_{\alpha_i}^2 & \sigma_{\alpha_i - \delta_i} & 0 \\ \sigma_{\alpha_i - \delta_i} & \sigma_{\delta_i}^2 & 0 \\ 0 & 0 & \sigma_{z_i}^2 \end{pmatrix} \quad (5)$$

where μ_α , μ_δ , and μ_z are the means of the RA, DEC, and z axes, respectively. $\sigma_{\alpha_i}^2$, $\sigma_{\delta_i}^2$, and $\sigma_{z_i}^2$ are the variances of the RA, DEC, and z axes, and $\sigma_{\alpha_i - \delta_i}$ is the covariance between the RA and DEC coordinates, which allows the projected Gaussians to be aligned at any angle on the sky. The $\sigma_{\alpha_i - z_i}$ and $\sigma_{\delta_i - z_i}$ covariance terms are zero because we do not expect appreciable rotation (compared to the velocity dispersion) within galaxy clusters (Hwang & Lee 2007).

Additionally, for each model, we include a background group, to account for the possibility of field galaxies. This background is modeled as a diagonal multivariate Gaussian with uninformative priors.

We assume uniform priors on all other parameters. Specifically, we enforce the ratio of semi-minor to semi-major axes to be between 0.4 and 1 to avoid highly elliptical projections (Schneider et al. 2012). We enforce the semi-major axis, as defined by the σ of the projected Gaussian, to be between 0.2 and 1 Mpc to avoid overfitting or generating nonphysically large subclusters. Finally, we restrict the velocity dispersion of subclusters to be less than the global velocity dispersion of the spectroscopic population for each cluster.

We run the MCMC with 400 walkers each taking 10,000 steps burning the first 5,000 steps to allow for convergence before posteriors are used to infer parameters. We checked that the number of steps is more than ten times the autocorrelation time to ensure convergence. For each model, we select the realization that results in the maximum likelihood fit. We then select the best model using the Bayesian Information Criterion (BIC):

$$BIC = -2 \log \hat{L} + k (\log n - \log 2\pi) \quad (6)$$

where $\log \hat{L}$ is the log-likelihood function, $k = 8i + 7$ is the number of free parameters to be estimated for i subclusters, and n is the number of datapoints (galaxies in our case). The BIC value measures the likelihood of each model while penalizing the models with more subclusters to avoid rewarding over-fitting. A lower BIC score indicates the data are more economically described by the model. We summarize the results of this analysis for 1RXSJ0603 in Figure 10 in which we plot the difference in BIC scores relative to the lowest BIC score among the models as an informative example. The shaded regions indicate the relative model success given the BIC

scores (Kass & Raftery 1995). There are three models with starkly lower BIC scores than the other nine. Each of these contain the two most massive subclusters (Jee et al. 2015); leaving these subclusters out results in poor models. The BIC scores for all models for each system are displayed Table 7, organized by cluster.

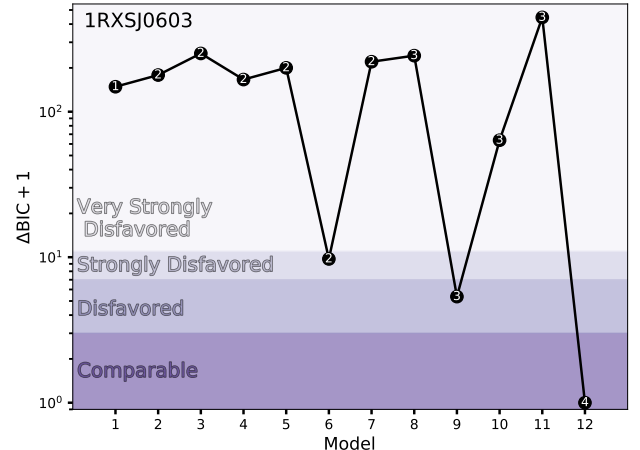


Figure 10. Bayesian Information Criterion scores relative to the most economical model for twelve 3D (RA, DEC, z) Gaussian Mixture Models fit to the 242 spectroscopic cluster member galaxies of 1RXSJ0603. The numbers in the black points indicate the number of subclusters included in a given model. The shaded regions roughly denote how a given model compares with the lowest BIC score (Kass & Raftery 1995). The most economical fit is a four component model (see Table 6 and 7). An analogous plot is not presented for each cluster; however, the ΔBIC scores are presented in Table 7.

We choose the BIC to quantify model success based on the results of Appendix A of Benson et al. (2017), which demonstrates that the BIC is less likely to overestimate the number of halos and less likely to artificially split halos on a suite of simulated clusters as compared to the corrected Akaike information criterion (AIC_c). The AIC_c is essentially similar to the BIC with a slightly lesser penalty for extra model parameters. An important conclusion is that the BIC virtually never underestimates the number of halos indicating that our models will place hard lower limits on the number of substructures in these clusters. For more details, we refer readers to Benson et al. (2017).

In Figure 11, we plot a projected-space (RA and DEC) scatter plot for the preferred model of 1RXSJ0603. The color-coded membership selection for each spectroscopic galaxy is assigned to the subcluster with the highest likelihood of hosting each galaxy based on the three dimensional Gaussian for each subcluster. The subcluster Gaussians are presented as projected ellipses centered on the most likely value with widths corresponding to the marginal 1- σ confidence in the RA and DEC positions. The same galaxy luminosity contours and radio relic contours from Figure 8 are displayed showing the alignment of galaxy substructure and the radio relic. We display analogous figures for the remaining 28 systems in Figure 12.

5.5. Redshift and Velocity Dispersion Estimation

Table 6

Priors for potential subclusters as deemed such by the routine discussed in §5.4 for 29 merging clusters. The first two systems are presented here. The remaining 27 systems can be found online in a machine readable table.

Cluster	Halo	X range (Mpc)	Y range (Mpc)	z range (1000 km s ⁻¹)
1RXSJ0603	a	[−0.58, −0.36]	[+0.32, +0.57]	[−2.5, −0.50]
	b	[−0.24, 0.02]	[+0.10, +0.37]	[−0.50, +0.50]
	c	[−0.67, −0.33]	[−0.78, −0.14]	[+0.75, +2.5]
	d	[+0.11, +0.33]	[−1.1, −0.75]	[−2.0, −1.0]
A115	a	[−0.45, −0.23]	[+0.06, +0.38]	[+0.05, +1.3]
	b	[−0.10, +0.13]	[−0.69, −0.42]	[−0.90, +0.30]

Table 7

MCMC-GMM models run for each system in our ensemble. The first two systems are displayed for demonstration of the form of the table. The remaining 27 systems can be found online in a machine readable table.

Cluster	Model	Halos included	N _{back}	Acceptance	BIC-BIC _{min}
1RXSJ0603	1	-	18	0.160	147
	2	ab	38	0.093	178
	3	ac	66	0.078	250
	4	ad	87	0.121	165
	5	bc	28	0.086	199
	6	bd	0	0.105	8.73
	7	cd	75	0.070	219
	8	abc	0	0.072	242
	9	abd	0	0.084	4.36
	10	acd	8	0.083	62.7
	11	bcd	1	0.052	444
	12	abcd	14	0.074	0
A115	1	-	0	0.170	33.3
	2	ab	26	0.093	0

With the galaxies separated into subclusters by our MCMC-GMM analysis, we implement the biweight statistic based on bootstrap samples of each subcluster's member galaxies and calculate the bias-corrected 68% confidence limits for the redshift and velocity dispersion from the bootstrap sample (similar to the global redshift analysis of §5.1). The redshift distributions of the subclusters for the lowest BIC model of 1RXSJ0603 are shown in Figure 13. We present the analogous figures for the remaining 28 clusters in Figure 14.

We use the biweight analysis to mitigate outliers from affecting the estimates of the subcluster redshifts and velocity dispersions, but this does not protect against the well known fact that mergers tend to bias high the velocity dispersion based mass estimates (Takizawa et al. 2010; Saro et al. 2013). The results of Dawson et al. (2015); Ng et al. (2015); Golovich et al. (2016, 2017) suggest that many of the mergers in the sample are observed at least several hundred Myr after pericenter.

5.6. X-ray Surface Brightness Maps

X-ray surface brightness maps are invaluable for determining the merger scenario. The gas is strongly affected by the merger due to ram pressure, and thus, the merger geometry is imprinted in the gas in ways invisible to optical and lensing studies. In Figure 15 shows the X-ray, radio, and optical features of 1RXSJ0603, and we present the remaining 28 systems in Figure 16.

6. RESULTS: INDIVIDUAL CLUSTERS

In this section we focus on each cluster individually. First, we present a detailed literature review and discuss

the history of understanding each cluster as (1) a merging galaxy cluster and (2) a radio relic cluster. Next, we discuss results of our analysis for each cluster and discuss these results in the context of the literature review. We reserve the ensemble analysis for §7. In each subsection, we will frequently refer readers to the figures (Figures 4–16) and tables (Tables 6 and 7) of the previous section. The potential halos discussed in the text and listed in Table 6 are arranged north to south as halos a, b, c, etc. Subclusters of the lowest BIC model are listed north to south as well, but given a numbered convention instead. The color sequence for presentation of the numbered subclusters is as follows. The northern most subcluster of each lowest BIC model is presented with green colors and labeled “Subcluster 1.” The color sequence is then, orange, purple, and pink for subclusters 2, 3, and 4, respectively. No system is found to have greater than four subclusters; however, as mentioned in §5.4, our models represent a lower limit for the true number of subclusters.

6.1. 1RXSJ0603

6.1.1. Literature Review

1RXSJ0603 (a.k.a. the Toothbrush—named after the radio relic morphology) was first cataloged by the ROSAT All-Sky Survey (RASS: Voges et al. 1999) as an extended and bright X-ray source ($L_{X, 0.2-2.4 \text{ keV}} \sim 10^{45} \text{ erg s}^{-1}$). It was confirmed as a galaxy cluster through cross-correlating RASS catalogs with the Westerbrook Northern Sky Survey (WENSS: Rengelink et al. 1997), the NRAO VLA Sky Survey (NVSS: Condon et al. 1998), and the VLA Low-Frequency Sky Survey (VLSS: Cohen

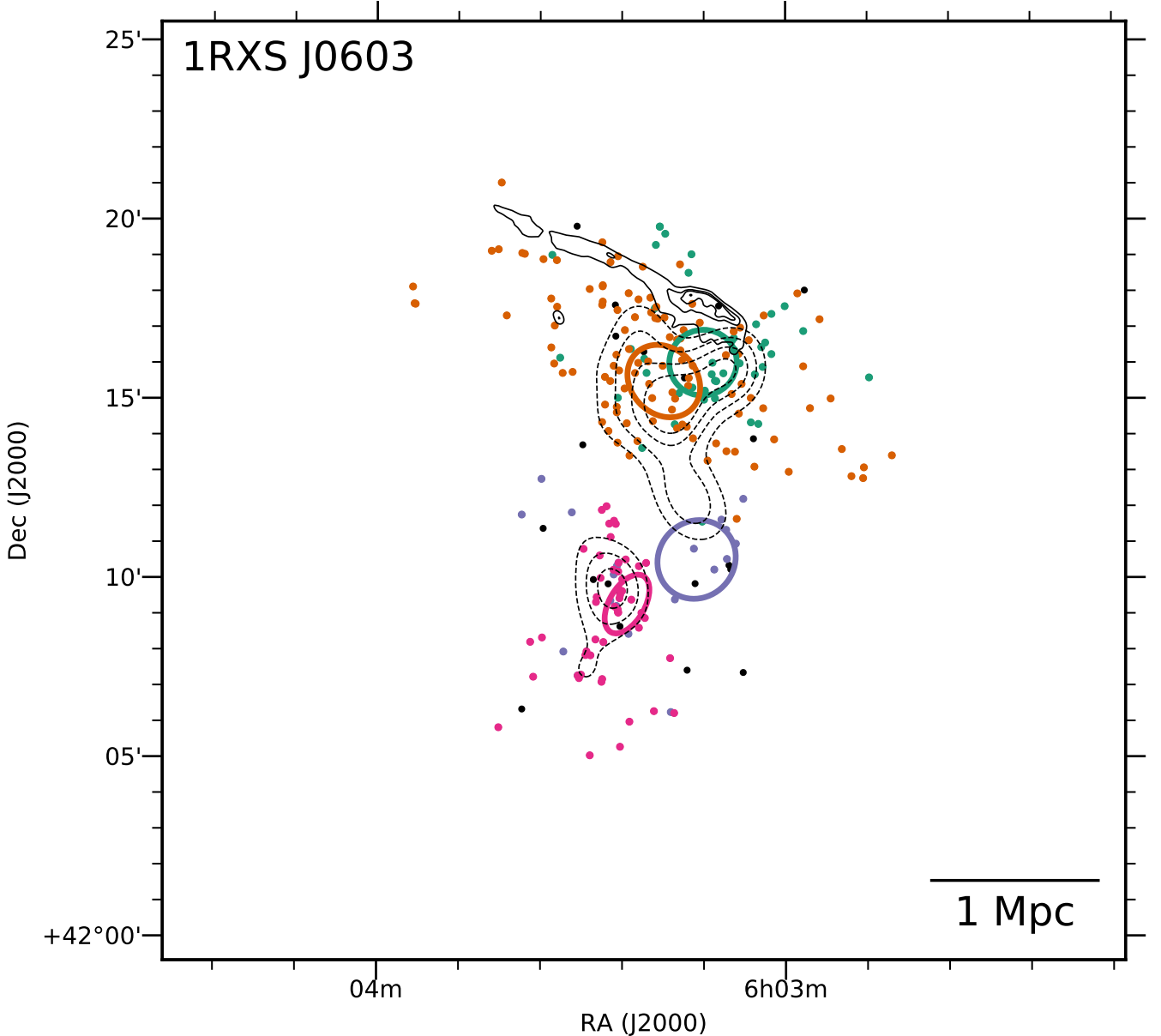


Figure 11. Subcluster membership for the lowest BIC model (see Table 7) for 1RXSJ0603. The dashed contours show the red sequence luminosity distribution starting at 3σ and increasing in units of σ where σ is the standard deviation of the pixel value within R_{200} . The solid black contours show the confirmed radio relic in the 610 MHz GMRT radio image presented in van Weeren et al. (2012b). The colored ellipses show the most likely projected position and size of the corresponding Gaussians from the GMM. The field is $2R_{200} \times 2R_{200}$ based on the global velocity dispersion and corresponding scaling relations (Evrard et al. 2008)

et al. 2007) in conjunction with inspection of the Two-Micron All-Sky Survey (2MASS: Skrutskie et al. 2006) images (van Weeren et al. 2011b,c). van Weeren et al. (2012b) followed-up with WSRT and GMRT radio observations between 147 MHz and 4.9 GHz and enabled the identification of a large ($LLS = 1.9$ Mpc) and bright linear radio relic in the north, a connected and elongated ~ 2 Mpc radio halo, and two smaller and fainter radio relics to the east and southeast. The number of diffuse radio features suggests that this is not a simple bimodal merger. A variable polarization fraction along the northern relic between 10 and 60% was measured, and the radio spectral index was used to estimate a Mach num-

ber of 3.3–4.6. The northern “toothbrush” relic and halo are connected by a region with a spectral index slope of $\alpha < -2$, but then flattens to $\alpha \sim -1.2$, and increases slightly towards the center of the halo. van Weeren et al. (2012b) indicate the possibility that previously accelerated electrons by the shock front are reaccelerated by merger induced turbulence, or even perhaps the halo region is in fact a relic viewed face on. With five spectroscopic redshifts of cluster members they estimated a cluster redshift of 0.225.

Brüggen et al. (2012) performed hydrodynamical N-body simulations to replicate the elongated nature of the toothbrush relic. They found that they reproduce the

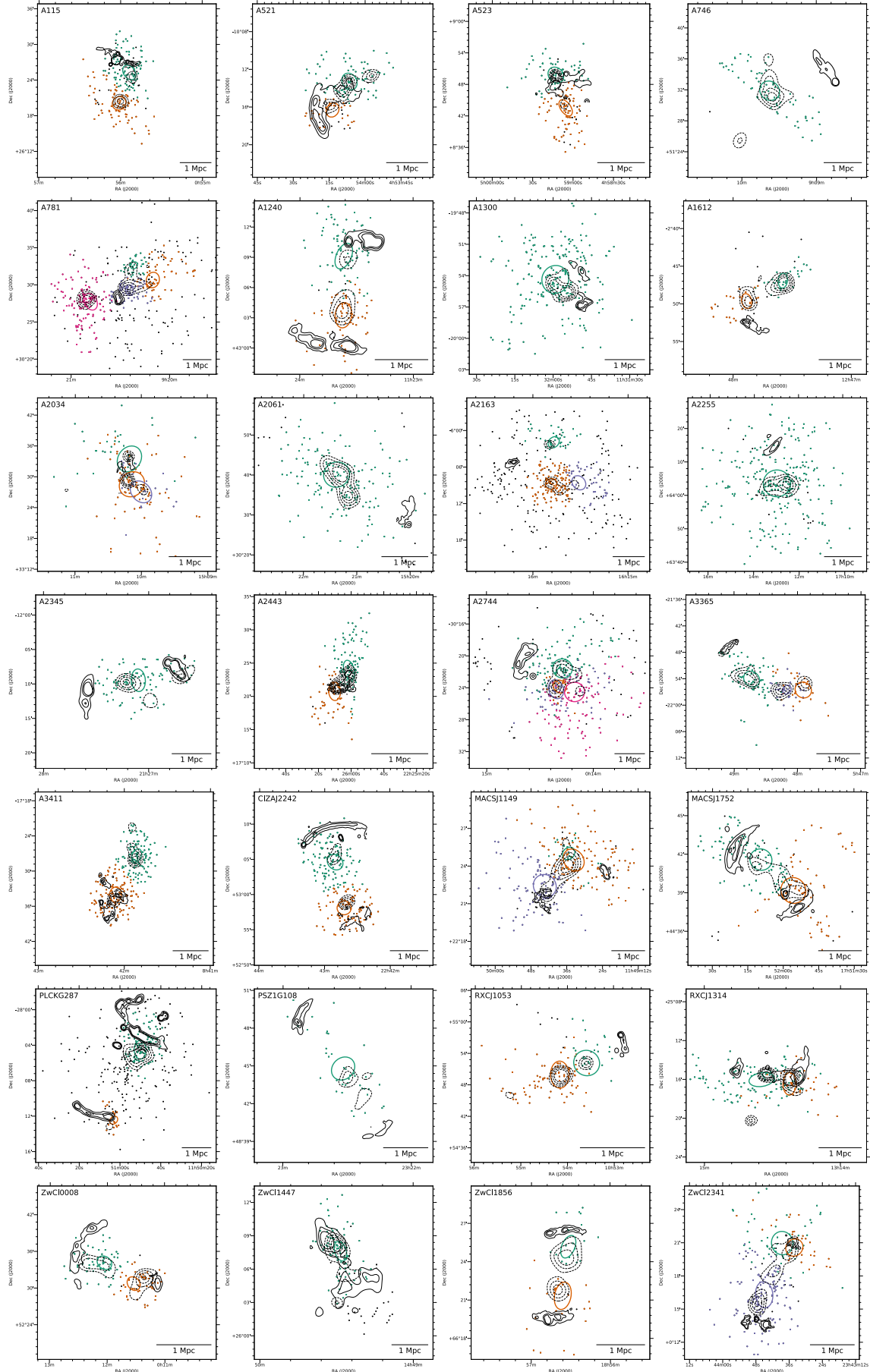


Figure 12. Subcluster membership for the lowest BIC model for 28 clusters. The panels are analogous to Figure 11. The radio relic contours are drawn from the radio images listed in Table 5. Individual figures are available in the online version of this article.

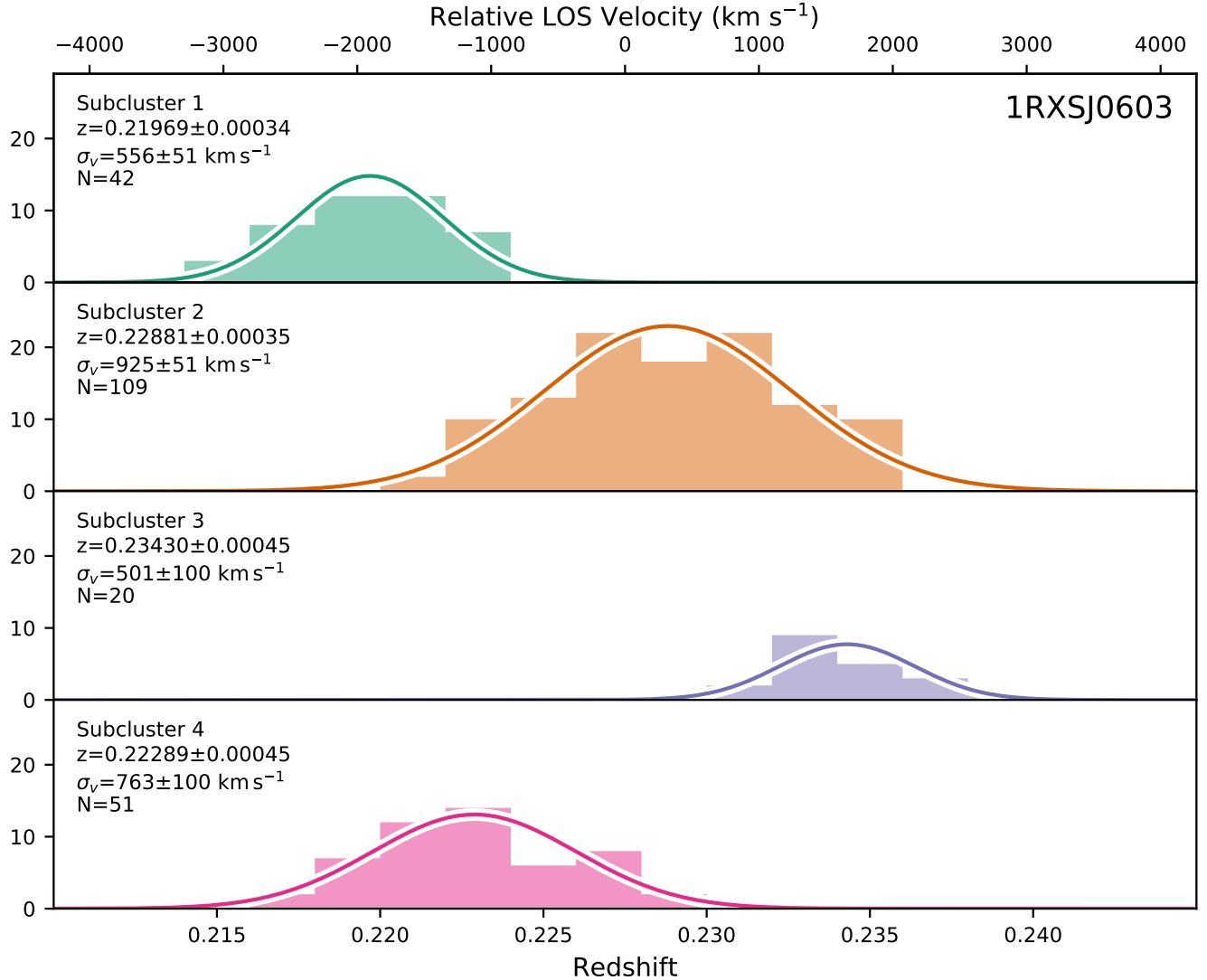


Figure 13. Subcluster redshift distributions for the lowest BIC model of 1RXSJ0603. The four subclusters are color coded according to the scatter points in Figure 11. The overlaid Gaussians are centered on the biweight redshift and have widths from the bias-corrected 68% confidence limits (Beers et al. 1990). The velocity scale at the top of the figure is in the cluster frame and is centered on $z = 0.2275$.

relic morphology with a triple merger between two equal mass subclusters merging along the north-south axis with a third smaller subcluster in-falling in the south on a mostly west to east trajectory. The third cluster then slingshots around and ends up in the northeast near the toothbrush handle.

Ogrealan et al. (2013c) observed 1RXSJ0603 with XMM-Newton and found X-ray gas density and temperature discontinuities at the locations of the three relics identified by van Weeren et al. (2012b) indicating that the relics likely trace underlying shocks in the ICM. However they only estimate a Mach number < 2 for the northern shock (inconsistent with radio Mach number of 3.3 - 4.6). They find that the X-ray shock is in part spatially offset from the radio emission in both distance and position angle. This runs counter to the diffusive shock acceleration assumption that particle acceleration occurs at the shock. Ogrealan et al. (2013c) also note the peculiarity of a density jump at the location of the eastern relic but no

surface brightness jump.

Stroe et al. (2013, 2015) present a narrow band H α survey or the 1RXSJ0603 field. They found no enhanced H α emitters are distributed near the northern shock, although there are at least six near the eastern relic candidate. The H α luminosity of 1RXSJ0603 is consistent with the low star formation rates of blank field galaxies at $z = 0.2$. They suggest that the difference between 1RXSJ0603 and CIZAJ2242 could be explained by 1RXSJ0603 being in a more evolved merger phase.

van Weeren et al. (2016) present new deep LOFAR low frequency radio observations and combine with VLA and GMRT data to provide a wide view of the radio spectrum. Spectral steepening from $\alpha = -0.8 \pm 0.1$ at the northern edge to $\alpha \sim -2$ towards the south. The spectral index suggests a Mach number of $\mathcal{M} = 2.8^{+0.5}_{-0.3}$ assuming diffusive shock acceleration. This confirms the discrepancy with the X-ray data from Chandra ($\mathcal{M} \lesssim 1.5$) which suggests that the relic emission is supported

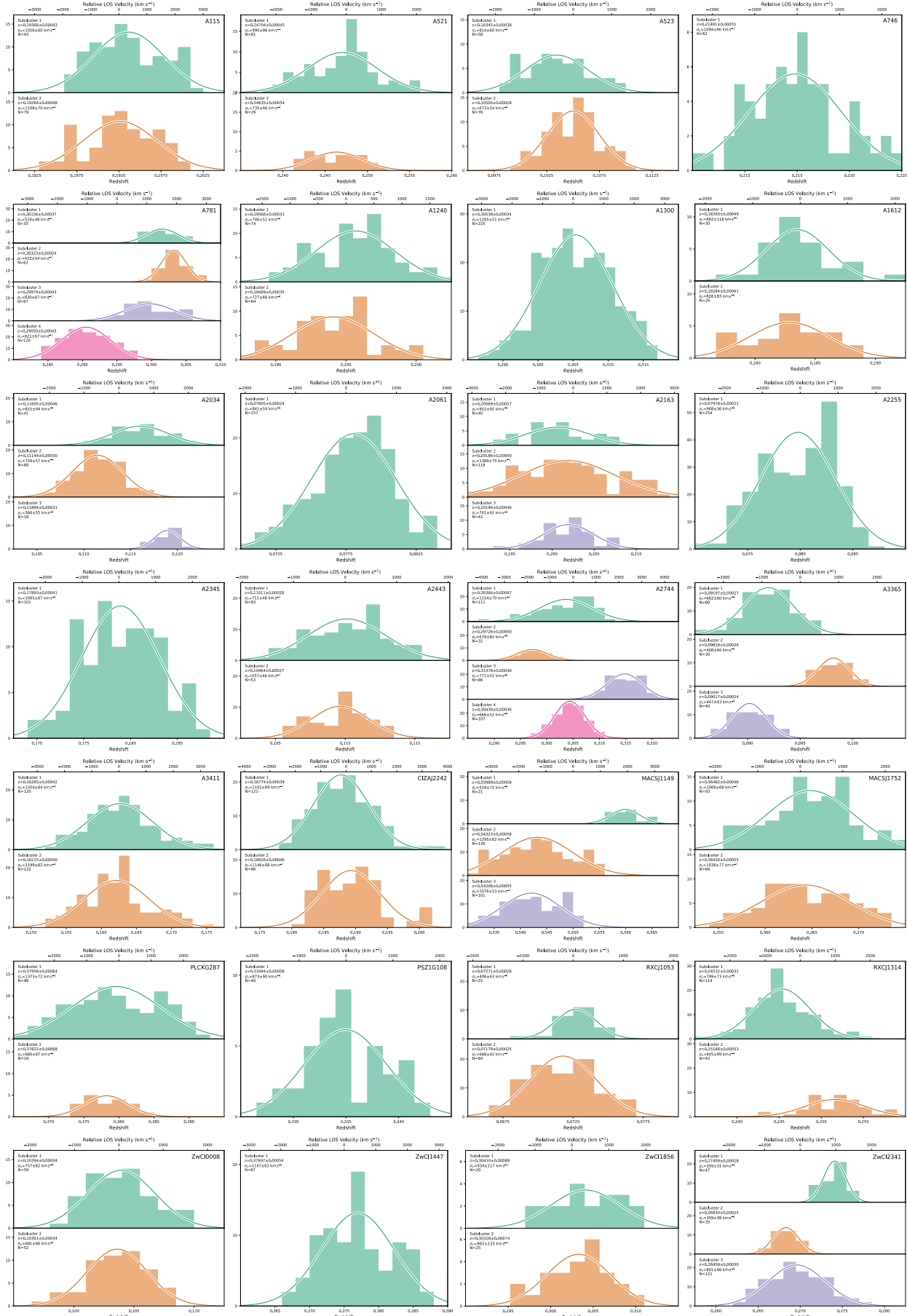


Figure 14. Subcluster redshift distributions for the lowest BIC model for 28 clusters. Each panel is analogous to Figure 13. Individual figures are available in the online version of this article.

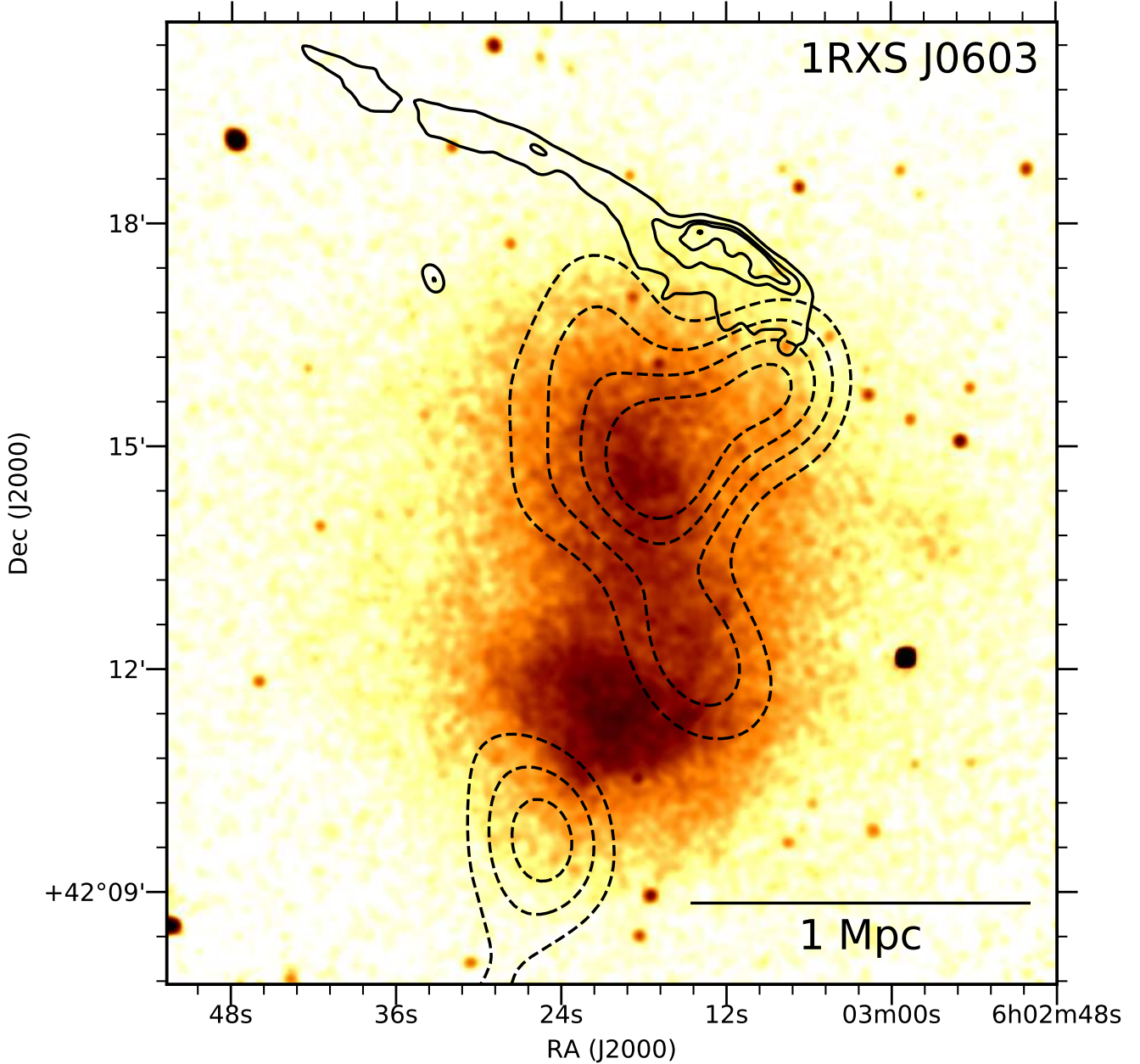


Figure 15. X-ray surface brightness map for 1RXSJ0603 based on a 250 ks of Chandra ACIS exposure. The map is created in the 0.5–2.0 keV band and is exposure corrected. GMRT 610 MHz solid black contours and red sequence luminosity dashed black contours are presented.

by pre-accelerated particles from a source such as radio galaxies.

Kierdorf et al. (2016) observed the radio relic at high frequency (4.85 and 8.35 GHz with 0.5 and 1.1 GHz bandwidths, respectively) with the Effelsberg 100-m telescope. They find a variable polarization along the radio relic with values up to $45 \pm 7\%$. Interestingly, the angle of the polarization vectors is variable along the relic, which is unexpected for a single shock front. Internal shock structure or foreground Faraday rotations are possible explanations.

Jee et al. (2015) present the only lensing analysis with a joint WL analysis on HST ACS/WFC3 and Subaru

SuprimeCam data. Four significant lensing peaks are discovered with good agreement between the lensing and cluster luminosity. Two of the four lensing peaks are situated in the north of the cluster toward the “tooth-brush” relic, one is far to the southeast, and the fourth is to the west. The two most significant peaks are oriented north-south and a merger between the two appears to have caused the elongation of the X-ray surface brightness profile as well as the “bristle” portion of the relic. Jee et al. (2015) fit a bimodal NFW profile (Navarro et al. 1996) and estimate $M_{200} = 6.29^{+2.24}_{-1.62} \times 10^{14} M_{\odot}$ and $1.98^{+1.24}_{-0.74} \times 10^{14} M_{\odot}$ for the main north and south subclusters are estimated, respectively. The total mass

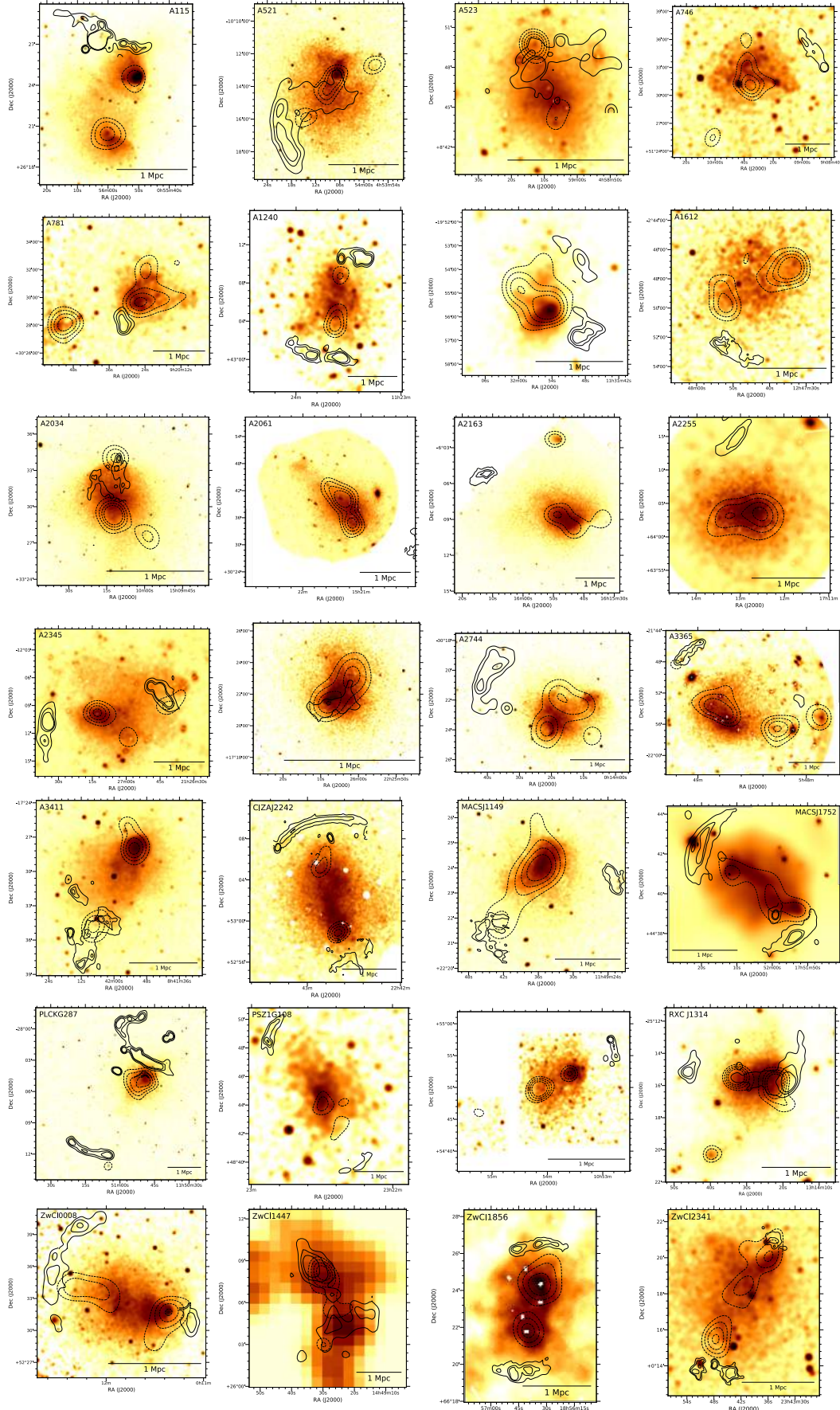


Figure 16. X-ray surface brightness maps for 28 merger clusters. Each thumbnail is analogous to Figure 15. Solid black contours are linearly spaced and represent radio relics from various radio images listed in Table 5. Dashed black contours are linearly spaced and represent the red sequence luminosity distribution. Individual figures are available in the online version of this article.

is estimated to be $\sim 10^{15} M_{\odot}$.

6.1.2. Results

We observed 1RXSJ0603 with three Subaru Suprime-Cam filters (*g*, *r*, and *i*) and four Keck DEIMOS slit masks resulting in 242 cluster members. The one dimensional redshift analysis of spectroscopic cluster members indicates that 1RXSJ0603 is a massive and rich cluster at $z = 0.22631 \pm 0.00038$. The global redshift histogram is well fit with a single Gaussian (see Figure 4). This could indicate that the merger is mostly in the plane of the sky (i.e. there is no peculiar velocity difference along the line of sight) and/or the subclusters are near apocenter (i.e. the relative 3D velocity is small).

In Figure 8 we present the red sequence luminosity map (*r* band), which is smoothed with a 41'' two dimensional Gaussian kernel. We confirm the results of [Jee et al. \(2015\)](#) finding up to four galaxy subclusters that are consistent with the lensing peaks. The DS-test circles in Figure 8 indicate a complex merger is underway between the various components. In the northern portion of the cluster, there is an East-West elongation. On the East side, the galaxies are at a redshift of $z \sim 0.23$ while on the West side, the galaxies are at a redshift of $z \sim 0.22$. Further south there is a bright star that affected our ability to target galaxies for spectroscopy. However, [Jee et al. \(2015\)](#) were able to successfully model and subtract the star from the Subaru SuprimeCam images. Note that we made use of the [Jee et al. \(2015\)](#) photometry in our analysis here. For details on the stellar profile subtraction see §2.1 of [Jee et al. \(2015\)](#). We detect a subcluster behind the star populated by a handful of cluster members at $z \sim 0.235$ in this region. Finally, in the south of the cluster, a large and well separated subcluster with $z \sim 0.22$ is aligned along the axis connecting the “head” of the Toothbrush relic with the Eastern half of the northern group of galaxies.

These four prospective subclusters are input into our MCMC-GMM analysis with input priors outlined in Table 6. In total, twelve GMM models are run (see Eq. 3). Details of these twelve models are listed in Table 7. We select the model with the lowest BIC score, which for 1RXSJ0603 is a four halo model including all four potential halos described above. Resultant subclusters 1–4 are ordered North to South. The four subclusters are presented in projected RA/DEC space in Figure 11. The subclusters are in agreement with the red sequence luminosity density map, and the substructure is roughly aligned with the radio relic (610 MHz GMRT data is presented in Figure 11).

The subcluster redshift analysis is presented in Figure 13. The head portion of the toothbrush radio relic is connected along an axis with the two most massive subclusters (2 and 4 in orange and pink, respectively); however, we cannot rule out more complicated merger scenarios. The brightness of the relic suggests that an extremely energetic merger occurred, which indicates that the primary collision occurred between Subclusters 2 and 4. These two subclusters are best aligned with the head of the toothbrush relic. Furthermore, the X-ray surface brightness map shows a bright ridge of gas connecting these two regions of the cluster lending further support for this scenario (see Figure 15).

To fully explore the range of merger scenarios, detailed

simulations are necessary covering a range of initial conditions, which is far beyond the scope of this paper. However, we hope that these results point simulators in the right direction and narrow the immense phase space to explore.

6.2. Abell 115

6.2.1. Literature Review

A115 has been extensively studied since its discovery as a double X-ray peak by [Forman et al. \(1981\)](#). [White et al. \(1997\)](#); [Shibata et al. \(1999\)](#); [Gutierrez & Krawczynski \(2005\)](#) have also studied its X-ray properties. [Giovannini et al. \(1987\)](#) conducted a 4.9 GHz VLA observation of the cluster primarily studying the bright radio galaxy source near the northern radio relic. [Govoni et al. \(2001b\)](#) followed this with a 1.4 GHz VLA observation and discovered the diffuse radio emission north of the cluster believed to be a radio relic. They note that there are two radio bright cluster members embedded in the diffuse relic emission. The relic is highly extended (~ 2.5 Mpc \times 0.5 Mpc) perpendicular to the supposed merger axis, however they note that the relic seems rather close to the northern cluster.

More recent X-ray analysis based on Chandra X-ray observations such as [Gutierrez & Krawczynski \(2005\)](#) (based on 50 ks) find that the northern and southern subclusters have cool cores (~ 3 keV) that are significantly cooler than the surrounding gas (~ 5 keV) and the hottest gas (~ 8 keV), which is located between the two subclusters. It is atypical for there to be two cool cores in a post merger system. [Rossetti et al. \(2017\)](#) found $\sim 30\%$ of Planck SZ clusters to have a cool-core, thus only $\sim 10\%$ of bimodal major mergers host two cool-cores pre-pericenter. It is unlikely that both would survive a head on collision, which perhaps suggests the subclusters did not pass through one another and instead merged with a large impact parameter. [Botteon et al. \(2016\)](#) analyzed deep Chandra observations (334 ks) finding evidence for a shock in both the density and temperature profiles of the ICM. Both methods suggest a low mach number of $M \sim 1.4 - 2.0$. The shock is spatially coincident with the western end of the radio relic. They argue that the location of the shock is explained by an off axis merger between unequal mass subclusters based on simulation results ([Ricker & Sarazin 2001](#)).

The picture of an unequal mass merger is substantiated by [Barrena et al. \(2007\)](#) with a spectroscopic survey obtaining 88 cluster member spectra, following up on an earlier survey by [Beers et al. \(1983\)](#), which resulted in 29 redshifts. In addition to clearly detecting the northern and southern subclusters [Barrena et al. \(2007\)](#) also find evidence for two smaller subclusters to the east (~ 0.5 Mpc). [Barrena et al. \(2007\)](#) interpret the system as being a pre-merger based on the agreement in location of the BCG’s and two X-ray peaks. However [Gutierrez & Krawczynski \(2005\)](#); [Botteon et al. \(2016\)](#) suggest that there has been a glancing merger. This is substantiated by the presence of the radio relic in the north. [Barrena et al. \(2007\)](#) find a large line-of-sight velocity difference between the north and south subclusters of 1646 km s^{-1} and a projected separation of 0.89 Mpc. They estimate that the merger is 100 Myr after core passage and is occurring within 20° of the plane of the sky. This would

require a substantial 3D merger speed of $\sim 4500 \text{ km s}^{-1}$, which is likely too large even for free-falling 10^{15} M_\odot subclusters from infinity.

[Okabe et al. \(2010\)](#) performed a weak lensing analysis of A115 based on Subaru SuprimeCam imaging and detected the north and south subclusters at a significance of ~ 4 and 5 sigma respectively. Interestingly both the north and south lensing peaks are offset from the corresponding galaxy density peaks (both luminosity and number) substantially. [Okabe et al. \(2010\)](#) only noted the complexity of this merger in passing stating that it is the reason for it being an outlier in their one-dimensional lensing analysis. [Oguri et al. \(2010\)](#) conducted the two-dimensional lensing analysis of this sample but made no significant note of the system.

6.2.2. Results

We made use of archival Subaru SuprimeCam imaging in V and i bands, and we observed A115 with two Keck DEIMOS slitmasks, which we combined with all redshifts from the literature yielding 198 galaxies confirmed at the cluster redshift. The one dimensional redshift analysis indicates that A115 is a massive system at $z = 0.19285 \pm 0.00040$. The global redshift distribution is very well fit by a single Gaussian with a velocity dispersion of $1439 \pm 79 \text{ km s}^{-1}$.

The red sequence luminosity (i band) is smoothed with a $52''$ two dimensional Gaussian kernel. We confirm a bimodal distribution with a north to south orientation. The DS-test circles indicate that the south subcluster is at a redshift of ~ 0.1925 and the northern subcluster is at a slightly higher redshift of ~ 0.195 (see Figure 9), which is also true for the two BCGs.

These two potential subclusters are input into our MCMC GMM analysis with input priors outlined in Table 6. Details of the two models run are presented in Table 7. We select the second model with two halos based on the substantially lower BIC score. Resultant Subclusters 1 and 2 (north to south) are presented in projected space in Figure 12. There is good agreement between the red sequence luminosity and spectroscopy with a slight offset in the Subcluster 1 stemming from uneven spectroscopic sampling. There are far more galaxies detected spectroscopically to the north of the BCG, which biased the GMM results. The two subclusters are roughly aligned with the western end of the radio relic (1.4 GHz VLA contours: [Govoni et al. 2001b](#)) and the associated shock ([Botteon et al. 2016](#)). The subcluster redshift analysis is presented in Figure 14. The two subclusters have similar redshifts suggesting a small line of sight velocity difference. The more complete data rules out a velocity difference of $\sim 1600 \text{ km s}^{-1}$ previously reported.

The X-ray surface brightness map (see Figure 16) shows clear bimodality and good agreement between the galaxies and X-ray peaks. There is clear evidence of a glancing merger in the swirl of gas to the east of the line connecting the two subclusters. Inspection of the wake features trailing the two gas cores suggest that the northern (southern) core is traveling southwest (northeast). This suggests that the subclusters have reached apocenter and the gas cores are spiraling around as gravity pulls them back. Simulations exploring a range of impact parameters will be necessary to fully understand the gen-

eration of a radio relic in glancing merger, but it seems that the merger phase can be well constrained given the present X-ray morphology.

6.3. Abell 521

6.3.1. Literature Review

Abell 521 has been extensively studied since its first detailed study by [Arnaud et al. \(2000\)](#), who noted a northwest to southeast bimodal X-ray distribution in the ROSAT/HRI imaging and an ‘X’ shaped galaxy distribution with one of the axes corresponding closely to the X-ray emission. They suggested that A521 might be a young cluster forming at the crossing of two filaments with one pointing towards A517 ($z=0.2244$, projected $82'$ away) and the other in the direction of A528 ($z=0.2896$, projected $106'$ away) and A518 ($z=0.1804$, projected $50'$ away). This study was also the first to note the existence of the large diffuse radio relic in the southeast apparent in NVSS imaging.

[Maurogordato et al. \(2000\)](#) used 41 spectroscopic redshifts and found evidence of three subclusters and a large velocity dispersion ($\sim 1400 \text{ km s}^{-1}$) for the system. The core of the brightest cluster galaxy showed clear signs of interaction effects, including the presence of multiple nuclei. They noted an arc-like feature to the north of the BCG, but the spectra placed on the arc did not detect the redshift. [Ferrari et al. \(2003\)](#) obtained 125 spectroscopic redshifts of cluster galaxies and found a similarly high velocity dispersion for the system. They claim that the system is composed of 7 groups and a ridge.

[Ferrari et al. \(2006\)](#) observed A521 for 38 ks with Chandra and confirmed the general finding of [Arnaud et al. \(2000\)](#) but with the higher resolution were able to identify two dominant clumps, a diffuse southern clump and a denser northern clump, which appear to have two sub-peaks. Additionally they found evidence for smaller clumps in the northeast and west. The two dominant X-ray peaks have a northwest to southeast axis consistent with the elongated galaxy axis. The radio relic is found to lie at the periphery of the X-ray emission which has been confirmed by [Giacintucci et al. \(2008\)](#) and [Bourdin et al. \(2013\)](#).

A521 has been observed in the radio from 153 MHz - 5 GHz; over this range the radio relic has a spectral index of $\alpha = -1.45$ ([Giacintucci et al. 2008; Brunetti et al. 2008; Dallacasa et al. 2009; Macario et al. 2013; Venturi et al. 2013](#)). [Giacintucci et al. \(2008\)](#) and [Macario et al. \(2013\)](#) noted that these results support the scenario where the radio relic is the result of Fermi type 1 diffusive shock acceleration. [Macario et al. \(2013\)](#) also note that the radio halo of A521 has a very steep radio spectrum with a slope $\alpha = \sim -1.8$, which suggests a large energy budget in the form of relativistic electrons. [Giacintucci et al. \(2008\)](#) estimates that the Mach number of the shock is ~ 2.3 based on the radio observations, which is consistent with the X-ray estimated Mach number of 2.4 ± 0.2 ([Bourdin et al. 2013](#)).

[Okabe et al. \(2010\)](#) performed a weak lensing analysis of A521. They do not discuss the results in detail other than noting that the radial shear profile of the cluster is poorly fit by a singular-isothermal-sphere profile and acceptably fit by an NFW profile, for which the estimate a total $M_{200} = 4.58 \pm 1.0 \times 10^{14} \text{ M}_\odot$. [Richard et al. \(2010\)](#)

observed the central region with HST WFPC2 and Keck LRIS and confirmed the arc identified by [Maurogordato et al. \(2000\)](#) to be three images of a face on spiral galaxy at $z = 1.043$. They complete a strong lensing analysis and estimate the mass within 250 kpc of $6 \times 10^{13} M_{\odot}$. They noted that since the strong lensing information is only on one side of the BCG, their strong lensing analysis was hindered with regards to determine the location of the peak of the mass distribution.

6.3.2. Results

We made use of archival Subaru SuprimeCam imaging (V and i bands) and 120 cluster member redshifts from NED. The global cluster redshift is 0.24676 ± 0.00041 and a velocity dispersion is $1100 \pm 76 \text{ km s}^{-1}$. This redshift distribution is well fit by a single Gaussian.

The red sequence luminosity distribution has at least three distinct peaks (Figure 9). The central peak is also elongated along the same northwest to southeast axis. Each of these regions is dominated by a distinct bright galaxy; however, the cluster-wide BCG is in the northern half of the middle luminosity peak. We placed subcluster priors centered on each galaxy over density and used conservative redshift windows (see Table 6) centered on the redshift of the brightest galaxy of each halo. The preferred model from the BIC analysis has two subclusters stemming from priors b and d in Table 6. Resultant Subclusters 1 and 2 are presented in projected space in Figure 12. There is good agreement with two of the three red sequence luminosity peaks. The NW red sequence peak was under-sampled spectroscopically, which likely contributed to our GMM's preference to discard it. More confirmed cluster members in this region are necessary to resolve this structure. The same is true of the southern extension of the middle group of bright red sequence galaxies. While there is a bright galaxy at its core, the redshift difference is small, so it is possible that it is in fact an offshoot of Subcluster 1. More redshifts would be required to explore this further. The preferred two subclusters are well aligned with the radio relic. In Figure 14, we present the redshift analysis of the two subclusters. Subcluster 1 is more massive than subcluster 2; and their line of sight velocity difference is very small. Subcluster 2 is not well fit by a single Gaussian. Inspecting the DS-circles in Figure 9 shows both blue and green circles in the central region of this subcluster, which could indicate composite line of sight structure or a lack of spectroscopy sampled from the underlying distribution.

The X-ray surface brightness map (see Figure 16) shows a bright peak of X-rays associated with subcluster 1, and a diffuse region near subcluster 2. This is indicative of a major merger between the two subclusters, along with the radio relic and galaxy distributions, which all lie collinearly.

In summary, Abell 521 may be as complex as a four way merger, but the available spectroscopy are unable to overcome the added parameters for more complex models than a simple bimodal model. That being said, the two preferred halos are likely the two that merged and launched the radio relic given the colinearity between the two subclusters, the X-ray extension, and the radio relic. Abell 521 is a prime candidate for deeper optical imaging in order to complete a strong and weak lensing analyses

to help map the dark matter distribution to better understand this system.

6.4. Abell 523

6.4.1. Literature Review

Abell 523 has been the subject of three detailed studies. [Giovannini et al. \(2011\)](#) were the first to note the diffuse radio emission associated with the cluster. They found a north-south bimodal distribution of galaxies with RASS X-ray emission between the two galaxy over-densities and also elongated in a north to south direction. They classify the diffuse radio emission as a radio halo but note that the radio luminosity is abnormally high given the X-ray luminosity. They also noted that the elongation of the radio halo perpendicular to the elongated distribution of gas and galaxies is atypical of radio halos.

[van Weeren et al. \(2011b\)](#) confirm the diffuse radio emission and bimodal galaxy distribution with deeper INT VRI imaging. However, they suggest that the diffuse radio emission should be considered as a possible radio relic due to its patchy morphology and perpendicular morphology with respect to the cluster gas.

[Girardi et al. \(2016\)](#) recently presented a detailed multi-wavelength study of the system. With new data including 132 spectroscopically confirmed galaxies (80 cluster members), INT imaging, and 27 ks Chandra exposure, it is found that Abell 523 is a massive system ($\sim 7.9 \times 10^{14} M_{\odot}$) based on σ_v -mass scaling relations. Two subclusters are identified along the same axis evident from previous studies. They find disturbance in the ICM with elongation toward the north/northeast direction in agreement with the RASS X-ray image. They confirm the presence of the radio feature and classify it as an extended radio halo. A merger of a bimodal head-on collision is discussed; however, more complicated scenarios are not ruled out. In addition, directly in the background a cluster present at $z \sim 0.14$ with an east–west bimodal distribution.

6.4.2. Results

We observed A523 with Subaru SuprimeCam in g and r bands, and with three slitmasks with Keck DEIMOS. Our spectroscopic survey largely overlapped that of [Girardi et al. \(2016\)](#) with an RMS velocity difference of $90(1+z) \text{ km s}^{-1}$ based on 59 duplicate redshifts. Our spectroscopic survey adds 175 unique galaxy redshifts and brings the total cluster member population to 149 galaxies. From our one dimensional redshift analysis, the global redshift is 0.10389 ± 0.00027 and the velocity dispersion is $921 \pm 53 \text{ km s}^{-1}$ in agreement with [Girardi et al. \(2016\)](#).

Additionally, we bring the number of background cluster members to 53 galaxies. Upon closer inspection, these 53 galaxies are split in velocity space into two groups; 37 galaxies with $z \sim 0.14$ are spatially dispersed behind Abell 523 with two over densities noted by [Girardi et al. \(2016\)](#). These galaxies have an average redshift and velocity dispersion of 0.13984 ± 0.00032 and $537 \pm 66 \text{ km s}^{-1}$, respectively. Additionally, 16 galaxies are tightly bunched in velocity space with a redshift of 0.15078 ± 0.00017 and velocity dispersion of $164 \pm 49 \text{ km s}^{-1}$; however, this over density of galaxies in velocity space is highly diffuse in projected space.

The red sequence luminosity (r-band) is smoothed with a $42''$ two dimensional Gaussian kernel. We confirmed a bimodal distribution of cluster galaxies with a north-south orientation. The DS-test circles indicate the northern subcluster has a redshift around 0.103, and the southern subculture has a redshift around 0.105. These two potential subclusters are input into our GMM analysis with prior distributions listed in Table 6. The two component model is strongly preferred over the null model with a single halo. Details of the two models are presented in Table 7. Resultant subclusters 1 and 2 are presented in projected space in Figure 12. The two sub-clusters are in good agreement with the red sequence luminosity distribution. Interestingly the diffuse radio feature is positioned nearly coincident with the northern subcluster, which poses a challenge for a bimodal merger scenario between subclusters 1 and 2 that launched a shock traveling north generating the radio relic. There have been conflicting classifications for this feature, despite its elongated morphology situated perpendicular to the merger axis. The subcluster redshift distributions are presented in Figure 14. The Subcluster 1 has a higher velocity dispersion and there is a moderate line of sight velocity difference though still small with respect to the velocity dispersion. Both subclusters are well fit by single Gaussians.

The X-ray surface brightness map (see Figure 16) shows an elongated and disturbed ICM situated between the two subclusters, which is a clear indication of a major merger between subcluster 1 and 2; however, as noted above, the radio relic's position is a challenge to explain as the result of a shock launched by this merger. Deeper X-ray and radio data may be required to resolve this issue. Furthermore, a weak lensing analysis may help by indicating the location of dark matter within this cluster.

6.5. Abell 746

6.5.1. Literature Review

A746 is a very little studied cluster. [van Weeren et al. \(2011b\)](#) identified a radio relic candidate in NVSS and confirmed it with deeper WSRT 1.4 GHz imaging. They found that the relic is located 1.7 Mpc to the northwest of the cluster center and has a physical extent of $1.1 \text{ Mpc} \times 0.3 \text{ Mpc}$. They also measured a large polarization fraction of $\sim 50\%$ (suggesting the merger axis is close to the plane of the sky). Their galaxy number density contours show a slight elongation along the north-south direction, which is roughly offset 45° relative to the cluster relic axis. However, optical information is highly contaminated by the bright star f Uma ($V_{mag} = 4.5$) located near the radio relic.

6.5.2. Results

Despite the very high light contamination by the star, we observed A746 with one Keck DEIMOS slitmask and two bands (g and r) of Subaru SuprimeCam. [Jee et al. \(2015\)](#) demonstrated the success of subtracting the stellar profile from optical imaging for 1RXSJ0603, which will be required before detailed analysis may be completed, but this is beyond the scope of this paper.

The DEIMOS observation resulted in 66 cluster members and a cluster redshift of 0.21434 ± 0.00059 and a cluster velocity dispersion of $1187 \pm 111 \text{ km s}^{-1}$. The red sequence luminosity density is complex with substructure

aligning north to south and east to west. The bright star may be limiting Source Extractor's ability to detect objects within the stellar halo where multiple galaxies are visible, but they are very highly contaminated. There is an additional group of red sequence galaxies $\sim 7'$ to the southeast of the cluster center nearly collinear with the radio relic (see Figure 9). However, our spectroscopic survey did not cover this region. Furthermore, the X-ray surface brightness does not appear to be disturbed in this direction (see Figure 16).

We conclude that the large amount of substructure in the red sequence luminosity distribution along with the clearly disturbed X-ray morphology indicate merger activity that generated the radio relic. However, given the extreme stellar contamination, we can not draw conclusions to as where merging substructure is located. We will not use A746 for any further ensemble analysis.

6.6. Abell 781

A781 is a well studied system, that is actually composed of multiple clusters at two different redshifts (0.3 and 0.43). After being cataloged by [Abell et al. \(1989\)](#), [Jeltema et al. \(2005\)](#) studied it as part of Chandra archival cluster survey. They briefly noted that it is a complex cluster with multiple peaks. [Wittman et al. \(2006\)](#) obtained deep ($R \sim 27$) multi-band optical imaging of the A781, since it is in Field 2 of the Deep Lens Survey (DLS: [Wittman et al. 2002](#)). They used this imaging to map the mass of the system via a weak lensing analysis. The mass map showed good agreement with the Chandra X-ray map. However, the western most subcluster was not discussed (since it fell outside the Chandra footprint), and the weak lensing mass map did not have the resolution to deblend the substructure within the main cluster. There have been multiple mass estimate analyses performed on A781 including weak lensing, X-ray, and galaxy velocity dispersion ([Abate et al. 2009; Kubo et al. 2009; Cook & Dell'Antonio 2012; Wittman et al. 2014](#)).

In an overlapping spectroscopic survey of DLS Field 2, [Geller et al. \(2005\)](#) found that the Main and Middle clusters were at redshifts of 0.302 and 0.291, respectively. However, they found that the East cluster is at a redshift of 0.4265. [Sehgal et al. \(2008\)](#) conducted two detailed X-ray analyses of the system using Chandra and XMM data, with their focus being on comparing X-ray and weak lensing mass estimates. They confirmed the previously reported Main, Subcluster, Middle, and East clusters ([Geller et al. 2005; Wittman et al. 2006](#)), as well as identified the West cluster in the larger field-of-view XMM image. In a later study [Geller et al. \(2010\)](#) also measured the redshift of the West cluster to be 0.4273 thus confirming that A781 consists of several subclusters in projection at two redshifts. In total they have obtained ~ 400 spectroscopic redshifts of the A781 system. While not specifically isolated in their analysis the substructure within the main cluster appears to be at the same redshift, (see Figure 13 of [Geller et al. 2010](#)).

[Venturi et al. \(2008\)](#) were the first to carry out a detailed radio study of A781 as part of their GMRT radio survey. In addition to a number of extended radio galaxies, they noted a low surface brightness radio feature southeast of the Main cluster, with out a matching optical counterpart, which they referred to as “periph-

eral radio emission". [Cassano et al. \(2010\)](#) note A781 to be an outlier in their study which showed that radio halos appear to be associated with clusters undergoing mergers, while those without halos are usually more relaxed. They argue that it is surprising that A781 does not have a detectable radio halo despite being disturbed. This is contradicted by [Govoni et al. \(2011\)](#), who claim to find evidence for a radio halo, as well as suggest that the radio emission identified by [Venturi et al. \(2008\)](#) is a radio relic on the grounds of its radial steepening. [Venturi et al. \(2011\)](#) question the claim of a radio halo, arguing that it would require an unusually steep radio spectrum since they do not detect it in their 325 and 610 MHz observations.

6.6.1. Results

We utilize the redshift catalog of the SHELS redshift survey, which covers the DLS Field 2 with complete spectroscopic coverage to a limiting magnitude of $R = 20.6$ using Hectospec ([Geller et al. 2014](#)). We combine known redshifts from the literature with the SHELS survey data to study A781. This results in 430 cluster members at the $z \sim 0.3$ cluster redshift. The global velocity distribution is very poorly fit by a single Gaussian indicating large velocity differences between the substructure along the line of sight (see Figure 5). The global redshift and velocity dispersion are 0.29748 ± 0.00034 and $1692 \pm 54 \text{ km s}^{-1}$, respectively. We note that this extreme velocity dispersion is not indicative of an extremely massive system, but rather of a system with large line of sight velocity differences.

Additionally, we identified 79 cluster members for the East group at a redshift of 0.42645 ± 0.00040 and a velocity dispersion of $766 \pm 64 \text{ km s}^{-1}$. We also identified 54 cluster members for the West group at a redshift of 0.42769 ± 0.00048 and a velocity dispersion of $764 \pm 79 \text{ km s}^{-1}$. The east and west groups are separated by $21'$ in projection ($\sim 7 \text{ Mpc}$ at $z = 0.43$). We will not discuss these groups further since their X-ray surface brightness distributions indicate that they are isolated halos and are uninvolved in a merger.

We made use of archival Subaru SuprimeCam imaging (V and i bands) and present the red sequence luminosity distribution (smoothed with a $40''$ Gaussian kernel) in Figure 9 along with the DS-test for the 430 cluster members. The source of the bimodal global redshift distribution is immediately evident with the significant line of sight velocity difference between the Middle ($z \sim 0.29$) and Main clusters ($z \sim 0.3$). Additionally, there is composite structure within the Main cluster with at least three groups. The luminosity peaks in the middle with extended light toward the north and west. Each of these extensions in the red sequence luminosity distribution hosts a bright BCG. We center the priors for our GMM on these galaxy locations and select a conservative redshift prior straddling the individual BCG redshifts for each group and a conservative prior range for the Middle cluster as well (see Table 6). Given the large line of sight velocity difference and large physical separation, our code should have no problem separating these structures. We note that the radio relic is situated to the southeast of the Main cluster. From the DS-test and redshift sequence luminosity distribution, it is ambiguous which subclusters provide the merger to create the radio relic.

Our GMM analysis results in a four component model with the lowest BIC score of twelve models varying from one to four subclusters. In addition, a three halo model without the halo b (see Table 6) was nearly as good of a fit. We focus on the four halo model because we can identify four distinct BCGs in the optical image as well as evidence for four distinct subclusters in the X-ray surface brightness profile (see Figure 16). Subclusters 1, 2, and 3 each are at $z \sim 0.3$ and subcluster four is at $z \sim 0.29$. The projected location of the three subclusters at $z \sim 0.3$ suggest a three way merger. The radio relic is situated in the southeast, which could indicate a merger between subclusters 1 and 3 or subclusters 2 and 3 that caused the radio relic. Inspection of the X-ray surface brightness shows that the gas is clearly more disturbed between subclusters 1 and 3 (green and purple in Figure 12). In fact, the ICM of subcluster 2 is situated coincident with the red sequence luminosity peak and appears to have a generally undisturbed profile; although, more X-ray integration will be necessary to confirm. There are relatively small line of sight velocity differences between these two subclusters, which are fit with individual Gaussians and presented in Figure 14.

In summary, these data provide a good example of the tremendous value of magnitude limited spectroscopy and combining it with multi-wavelength observations. Taking all evidence into account, the merger likely occurred between subclusters 1 and 3 launching the shock that created the radio relic to the southeast. Subcluster 2 is yet to reach core passage (although very near), and subcluster 4 is positioned along the line of sight with a large peculiar velocity difference. These four subclusters will likely eventually coalesce and form a single cluster.

6.7. Abell 1240

6.7.1. Literature Review

[Kempner & Sarazin \(2001\)](#) first suggested that A1240 hosts a radio relic based on diffuse emission detected in WENESS and NVSS images and an elongated X-ray emission from a pointed ROSAT observation. They suggested a non-zero impact parameter based due to the slightly off-axis location of the relics. [Bonafede et al. \(2009\)](#) confirmed two relics with VLA observations at 325 MHz and 1.4 GHz, and found average spectral index values of -1.2 ± 0.1 and -1.3 ± 0.2 for the northern and southern relics, respectively. They also measured integrated fractional polarizations of 26% and 29% for the northern and southern relics, respectively, with both having values ranging up to 70%.

[Barrena et al. \(2009\)](#) analyzed SDSS and INT WFC imaging and found a bimodal galaxy distribution—like, the relics, separated along a north to south axis. They used 95 member redshifts to find a line of sight velocity difference between the two subclusters of $\sim 400 \text{ km s}^{-1}$, and using a two-body model, they estimated a rest-frame 3D velocity difference of $\sim 2000 \text{ km s}^{-1}$. They measured a LOS velocity dispersion for the system of $\sim 870 \text{ km s}^{-1}$ and a corresponding mass of $\sim 0.9 - 1.9 \times 10^{15} \text{ M}_\odot$. [Barrena et al. \(2009\)](#) also analyzed archival Chandra data (51 ks) and derived a temperature of $\sim 6 \text{ keV}$ confirming a massive system. They also noted $A1237 \sim 10'$ to the south at a similar redshift; however, it is likely uninvolved in the merger in the observed state based on the

position of the radio relics.

6.7.2. Results

We observed two additional slitmasks for A1240 with Keck DEIMOS bringing the total number of confirmed cluster members to 146. The global redshift distribution is presented in Figure 5. The cluster redshift is 0.19458 ± 0.00029 , the velocity dispersion is 853 ± 62 km s $^{-1}$, and the redshift distribution is well fit by a single Gaussian. We also identify 24 cluster members for A1237 located ~ 2 Mpc to the southwest of A1240. A1237 has a redshift of 0.19374 ± 0.00053 and a velocity dispersion of 721 ± 83 km s $^{-1}$.

We observed A1240 in g and r bands with Subaru SuprimeCam. The red sequence luminosity distribution is smoothed with a 52'' Gaussian kernel and presented in Figure 9. A bimodal distribution aligned north-south between the radio relics is revealed suggesting a simple geometry. We select priors for the two subclusters for our GMM analysis based on conservative windows around the BCG redshifts and locations for these two subclusters (see Table 6). The two halo model is strongly favored by the BIC score (see Table 7). The two inferred subclusters are well aligned with the red sequence luminosity distribution and between the two radio relics (see Figure 12). The redshift distributions for the two subclusters are presented in Figure 14. The two are very similar suggesting a 1:1 mass ratio in the plane of the sky. Inspection of the X-ray surface brightness distribution in Figure 16 furthers this picture making A1240 among the cleanest bimodal mergers known and is a good candidate for further study.

6.8. Abell 1300

6.8.1. Literature Review

Pierre et al. (1994) studied A1300 with X-rays, as part of RASS, and in the optical with the ESO 3.6 m Telescope. Of their 42 RASS cluster sample they found that it was the most luminous at $z > 0.3$. The cluster was found to be optically rich and extended suggesting merger activity. Pierre et al. (1997) conducted a spectroscopic and photometric (B and R) follow-up of the cluster. With 52 spectroscopic redshifts of cluster members they measured a velocity dispersion of 1210 km s $^{-1}$. While they noted apparent substructure in 2D projected space, the velocity histogram was well modeled by a single Gaussian. Lemonon et al. (1997) presented deeper ROSAT observations of the cluster as well as added 10 more spectroscopic cluster member redshifts from the previously non-surveyed northern region. They argue that the multiple wavelength analysis suggests that A1300 is a major cluster merger that occurred at an early epoch. They argue that it is a merger where the clusters have already returned after their first pass through, since they do not detect an offset between the X-ray gas and the galaxies, nor do they detect evidence for substructure in the velocity histogram; although, this doesn't rule out a plane of the sky merger.

Giovannini et al. (1999) included A1300 in a list of radio halo and relic candidates in NVSS. Reid et al. (1999) discovered a number of diffuse radio sources in the vicinity of the cluster. They detect a number of tailed radio galaxies along the north-south axis of the cluster and one

to the northwest. Additionally, they argue that the diffuse emission to the southwest is a radio relic and that the central diffuse radio source coincident with ROSAT detected diffuse X-ray emission is a radio halo. Venturi et al. (2013) conducted GMRT follow-up observations of A1300 and largely confirm the Reid et al. (1999) interpretation. However, they discovered another possible radio relic candidate to the northwest. Unlike most mergers, two relics are discovered at 90° about the cluster center, and the radio halo is offset considerably from the bulk of the X-ray gas emission (in the opposite direction).

Ziparo et al. (2012) conducted a detailed optical/X-ray analysis of the system utilizing WFI imaging, VMOS spectra, and XMM X-ray spectral imaging. They note that the X-ray surface brightness map of A1300 appears disturbed and exhibits the signature of a shock consistent with the radio observations. They also claim the detection of a large-scale filament in which the main cluster is embedded. Ziparo et al. (2012) compare their observations with existing simulations and argue that A1300 is a complex systems where a major merger occurred ~ 3 Gyr ago with continual minor mergers occurring as filamentary groups are feed into the cluster. Note that the galaxy density extensions to the northeast and southeast of the cluster center are inline with the two radio relics discovered by Reid et al. (1999) and Venturi et al. (2013). However, it is unclear that minor mergers could produce bright radio relics.

6.8.2. Results

We observed A1300 with Subaru SuprimeCam in g and r bands. We utilize 227 cluster member galaxies from Ziparo et al. (2012). We find a cluster redshift of 0.30550 ± 0.00034 and a velocity dispersion of 1227 ± 55 km s $^{-1}$ in agreement with previous studies. The red sequence luminosity distribution has a primary elongation along a northeast to southwest axis aligned with the radio relic. Additionally, this is an extension to the north that could explain the radio relic candidate (see Figure 9). The DS-test shows a group of large yellow circles in the northeast; however, these galaxies have too low luminosity to stand out in the red sequence luminosity map. They are likely a well sampled low mass group that is too far from the cluster center to be dynamically important.

We place potential subcluster priors centered on the BCG of the three extended regions of the luminosity distribution, and center the redshift prior on the respective BCG redshifts (see Table 6). In total, five GMM models are run and compared with the BIC score. The single halo model is preferred. Inspecting Figure 9 again suggests potential reasons for this. The three subclusters are not well separated in projected space. Furthermore, the spectroscopic survey has not densely sampled the inner regions of the subclusters instead sampling the global cluster fairly uniformly over an area $\sim 3 \times 3$ Mpc.

Since the data do not support more complex subcluster models, we conclude with a mention of the BCGs for each potential subcluster. We listed our three proposed priors for the potential subclusters in Table 6. The redshifts of the three BCGs are 0.3082, 0.3016, and 0.3077, respectively. The confirmed radio relic to the southwest was likely launched by a merger between the second and third listed, which have a large line of sight velocity difference. This could explain the small angular projection

between subclusters; i.e., the merger is occurring substantially along the line of sight. In order to explore this further, the cluster cores should be more densely sampled spectroscopically.

6.9. Abell 1612

6.9.1. Literature Review

A1612 is a very little studied cluster. [van Weeren et al. \(2011b\)](#) provided the first targeted analysis of the system finding evidence for it being a post merger radio relic cluster. From ROSAT X-ray imaging they find an elongated gas distribution that is in agreement with the elongated (slightly bimodal) galaxy distribution based on SDSS imaging. With GMRT observations they find diffuse radio emission for which they cannot find an optical counterpart and classify it as a likely relic. The relic sits slightly off axis to the south of the cluster X-ray emission.

More recently, [Kierdorf et al. \(2016\)](#) observed the relic at 4.85 and 8.35 GHz with the Effelsberg 100-m telescope. Unfortunately, the large beam and nearby bright radio galaxy washed out the relic. A polarization of $20\pm7\%$ is estimated at 8.35 GHz near the relic location. Furthermore, Chandra X-ray data (29 ks) is presented, and the smoothed X-ray surface brightness map suggests a merger along a northwest to southeast axis, and X-ray point sources are detected in association with the radio point sources. Each point source has an optical counterpart in SDSS and appear to the BCG for each merging subcluster. A global X-ray temperature of $T_X = 5.50^{+0.4}_{-0.3}$ keV and 0.1–2.4 keV luminosity of $L_X = 1.8 \times 10^{44}$ erg s $^{-1}$ are estimated.

6.9.2. Results

We obtained one slitmask of Keck DEIMOS spectroscopy, which when combined with spectra from NED results in 73 cluster member galaxies. We made use of archival Subaru SuprimeCam imaging in V and i bands. The global redshift distribution is well fit by a single Gaussian of redshift 0.18229 ± 0.00049 and velocity dispersion 1081 ± 96 km s $^{-1}$. Meanwhile, the red sequence luminosity distribution is bimodal along an axis from southeast to northwest. The radio relic is slight south of this axis (see Figure 9). We place conservative priors on the peaks of the red sequence luminosity distribution (see Table 7) and the two halo model is preferred by the BIC score.

The two subclusters are displayed in projected space in Figure 12 showing good agreement with the red sequence luminosity distribution. They are displayed in velocity space in Figure 14. The two subclusters appear to be similarly massive and have a small line of sight velocity difference. Inspection of the X-ray surface brightness distribution shows elongation between the two subclusters. In summary, A1612 is undergoing a bimodal merger between similarly massive subclusters in the plane of the sky. The offset radio relic suggests a possible non-zero impact parameter; however, additional X-ray data, spectroscopy, and radio imaging will be necessary to understand this merger.

6.10. Abell 2034

6.10.1. Literature Review

A2034 is a well studied system at all wavelengths. [Kempner & Sarazin \(2001\)](#) noted faint extended WENSS radio emission north of the cluster center coincident with a discontinuity in the RASS X-ray image. [Kempner et al. \(2003\)](#) used Chandra to identify a cold front near this location and confirm that A2034 is a merging cluster. [Giovannini et al. \(2009\)](#) identified diffuse radio emission coinciding with the center of the cluster but noted that it appears elongated and irregular with respect to other radio halos. They also confirmed the diffuse radio emission north of the cluster (but connected to the other diffuse emission) and its coincidence with the X-ray cold front. With deeper Chandra data [Owers et al. \(2014\)](#) show that this cold front is actually a shock with a Mach number of 1.59 ± 0.06 corresponding to a shock velocity of ~ 2000 km s $^{-1}$. [Kempner et al. \(2003\)](#) also argued that the observed southern X-ray excess is not associated with the cluster and is likely a background cluster between $0.3 < z < 1$, however [Owers et al. \(2014\)](#) infer that the excess is consistent with it being gas stripped during the merger.

With WSRT [van Weeren et al. \(2011b\)](#) observed the diffuse emission to brighten near the position of the shock. They note that it is debatable whether this really is a radio relic. They also identify a small candidate radio relic (~ 200 kpc \times 75 kpc) to the west of the cluster center. [van Weeren et al. \(2011b\)](#) also note that the galaxy distribution appears bimodal, with two relatively equal distributions. However, [Okabe & Umetsu \(2008\)](#) find a more complex galaxy distribution based on luminosity density maps using Subaru imaging. [Owers et al. \(2014\)](#) use 328 spectroscopically confirmed cluster members to show that there is a substructure located at the front edge of the shock and that the galaxy distribution is more complex. Given the redshifts of this northern and main structures as well as the X-ray shock velocity they estimate the merger is occurring along an axis within ~ 23 degrees of the plane of the sky and observed ~ 0.3 Gyr after core-passage. [Okabe & Umetsu \(2008\)](#) also present the only weak lensing analysis and estimate a $M_{200} = 10.24 \pm 6.14 \times 10^{14}$ M $_{\odot}$, which is consistent with the [Geller et al. \(2013\)](#) spectroscopic velocity caustic estimate of $8.0 \pm 0.1 \times 10^{14}$ M $_{\odot}$. Note that both mass estimates treat A2034 as a single system when estimating the mass.

Most recently, [Shimwell et al. \(2016\)](#) present low frequency LOFAR radio observations and detect a complex network of steep spectrum radio features including a radio halo as well as up to three candidates for radio relics. One of these relics is coincident with the shock detected by [Owers et al. \(2014\)](#) and another is the same relic candidate detected by [van Weeren et al. \(2011b\)](#).

6.10.2. Results

We make use of 140 archival spectroscopic cluster members from NED. There are an additional 328 spectra from [Owers et al. \(2014\)](#) that are not public. We also utilized archival g and R band images from Subaru SuprimeCam. The R image is in fact the deepest image in our sample. The spectroscopy indicates a global redshift of 0.11381 ± 0.00033 and a global velocity dispersion of 1080 ± 55 km s $^{-1}$. The velocity histogram is well fit by a single Gaussian. Meanwhile, the red sequence luminosity distribution indicates at least three subclusters. The two brightest peaks are oriented north to south with the

northern group actually slightly north of the diffuse radio emission identified as a radio relic candidate, which is unusual and challenges the picture of the relic tracing the shock that generated by this possible north to south merger. The third peak in the red sequence luminosity distribution is situated to the southwest and has lower surface brightness.

We generated three subcluster priors (Table 6) and the GMM results in the three subcluster model with the lowest BIC. The three subclusters have relatively large line of sight velocity differences compared to other systems in our sample. Subclusters 1 and 2 are similar in velocity dispersion, and subcluster three is a low mass subcluster. Inspection of the X-ray surface brightness distribution further indicates that the primary merger is between subclusters 1 and 2. Interestingly, the northern subcluster 1 is ahead of the shock, which is hard to explain if the merger is bimodal. The shock and subcluster should decouple due to gravity post pericenter with the shock running ahead. For this reason, we can not rule out more complex merger scenarios.

6.11. Abell 2061

6.11.1. Literature Review

A2061 is a member of the Corona Borealis supercluster, which is collectively at $\sim z = 0.07$. This supercluster is extensively studied by SDSS thanks to its low redshift and full coverage by the SDSS footprint. A2061 is located $\sim 30'$ (2.7 Mpc) southwest of Abell 2067 (hereafter A2067), with a relative line of sight velocity difference of $\sim 600 \text{ km s}^{-1}$, and to which it is likely gravitationally bound (Rines & Diaferio 2006). This velocity difference is significantly lower than the $\sim 1600 \text{ km s}^{-1}$ estimate of Oegerle & Hill (2001). Rines & Diaferio (2006) note that A2061 is about 4 times more luminous in X-rays than A2067. Marini et al. (2004) note that the X-ray profile of A2067 is elongated in the northeast to southwest along the same axis as A2067, however van Weeren et al. (2011b) note that this elongation may be due to observed optical substructures within A2061 rather than an interaction with A2067. They also note that these substructure interactions within A2061 are likely the result of the observed radio relic to the southeast of A2061 (Kempner & Sarazin 2001; Rudnick & Lemmerman 2009; van Weeren et al. 2011b).

Abdullah et al. (2011) carried out an updated velocity dispersion analysis of A2061 finding $\sigma_v = 725 \pm 67 \text{ km s}^{-1}$ corresponding to a viral mass of $5.45 \pm 0.19 \times 10^{14} \text{ M}_\odot$. Einasto et al. (2012) carried out a GMM substructure analysis of the A2061/A2067 system and found that it was best fit by a three component mixture, but they do not present the spatial or redshift distributions of these substructures. The Planck Collaboration (Planck Collaboration et al. 2013) included the A2061/A2067 system in their study of filaments between interacting clusters but do not note anything specific about this system. Farnsworth et al. (2013) used Green Bank Telescope observations and found evidence for a possible inter-cluster filament between A2061 and A2067. They also find the first evidence of a radio halo in A2061 at 1.4 GHz.

6.11.2. Results

We obtained 157 cluster member redshifts for A2061 from SDSS and NED. We observed the system with Subaru SuprimeCam in g, r, and i bands. The velocity distribution is well fit by a single Gaussian of redshift 0.07805 ± 0.00025 and velocity dispersion $841 \pm 55 \text{ km s}^{-1}$. The red sequence luminosity is bimodal in a northeast to southwest axis. The northeast bright peak is also elongated along this axis.

We run one and two subcluster models with our GMM; the one halo model is preferred. Similar to A1300, we believe this is due to small projected separation between the two subclusters and also the spectroscopic sampling, which does not densely probing the cores of the two subclusters. Evidence from the bimodal red sequence luminosity distribution, extended X-ray emission, and radio relic in the southwest suggest a merger along this axis; however, the spectroscopic data are unable to further confirm this picture given the additional model parameters necessary. We will study line of sight velocity differences with the BCGs of each subcluster in §7.

6.12. Abell 2163

6.12.1. Literature Review

A2163 is one of the richest Abell clusters and has been extensively studied since it was identified as an exceptionally hot system (15 keV; Arnaud et al. 1992). This cluster has been identified as the most massive in Planck SZ catalog (Planck Collaboration et al. 2016). Many X-ray studies have found evidence that the cluster has a non-isothermal gas distribution with strong temperature variations in the center of the cluster (Markevitch et al. 1994; Elbaz et al. 1995; Markevitch et al. 1996; Markevitch & Vikhlinin 2001; Govoni et al. 2004; Ota et al. 2014). Feretti et al. (2001) were the first to identify a radio halo centered on the cluster and a potential radio relic ~ 2.2 Mpc to the northeast of the cluster center. Feretti et al. (2004) followed up the initial radio observations and measured the spectral index associated with the radio emission. Note that the hottest part of the X-ray emission (18 keV; Bourdin et al. 2011; Ota et al. 2014) is correlated with the location of the radio relic in the northeast of the main cluster. Many of the aforementioned X-ray studies along with Rephaeli et al. (2006) have attempted to measure a non-thermal component due to inverse Compton scattering of CMB photons by the relativistic population of particles suspected to be associated with the diffuse radio emission, but no conclusive evidence of non-thermal emission has been observed yet. SZ analyses have been completed as well (Wilbanks et al. 1994; Nord et al. 2009). The latter study found a low line of sight velocity difference and results consistent with an extremely massive cluster. The most recent radio analysis covered low frequencies between 88 MHz and 200 MHz using the Murchison Widefield Array. The radio relic and halo were detected in all radio images, and the spectral index for the halo and relic between 88 MHz and 1.4 GHz were estimated to be -0.90 ± 0.19 and -1.05 ± 0.19 , respectively (George et al. 2017).

A number of weak lensing analyses of the cluster have been carried out (Squires et al. 1997; Radovich et al. 2008; Okabe et al. 2011; Soucail 2012). Okabe et al. (2011) and Soucail (2012) both find evidence for a bimodal mass distribution with the peak of the X-ray gas

located between the two mass peaks. Additionally, [Soucail \(2012\)](#) identifies a mass peak $\sim 6'$ (~ 1.2 Mpc) to the north of the main cluster, which corresponds to substructure A2163-B identified in a spectroscopic survey of the area by [Maurogordato et al. \(2008\)](#). They argue that this structure will eventually merger with the main subcluster. [Soucail \(2012\)](#) estimate that the main cluster is composed of two subclusters of masses 7.1 and 2.5×10^{14} M_{\odot} that have undergone their first pass through and that the infalling A2163-B has a mass of $\sim 2.7 \times 10^{14}$ M_{\odot} . There is some discrepancy between these and the [Okabe et al. \(2011\)](#) mass estimates, which suggest a 8:1 to 10:1 mass ratio of the merging subclusters in the main cluster and a total mass for the system that is about 50% larger than the [Soucail \(2012\)](#) estimate. [Bourdin et al. \(2011\)](#) estimate a 4:1 mass ratio between the A2163-A subcluster components and conduct a timing-argument dynamics analysis which they suggest implies that the A2163-A subclusters collied ~ 0.1 -1.0 Gyr ago. All of these weak lensing analyses are based upon ground based weak lensing, and HST data reveals a more unsettled core than a simple bimodal structure (private communication with Doug Clowe).

6.12.2. Results

We base our analysis upon 382 archival spectroscopic galaxies from NED and [Maurogordato et al. \(2008\)](#) as well as archival Subaru SuprimeCam imaging in V and R bands. The spectroscopy indicates an extremely massive system with a redshift of 0.20115 ± 0.00035 and a velocity dispersion of 1469 ± 57 km s $^{-1}$. The redshift distribution is well fit by a single Gaussian.

The red sequence luminosity distribution is clearly bimodal between the northern and main components identified by [Soucail \(2012\)](#). The main cluster has three brightness peaks aligned east to west. The cluster BCG is in the easternmost subcluster. The redshifts of each subcluster are similar (see Figure 9), which poses a challenge for our GMM with small offsets in the projected spatial dimensions as well. We center uniform priors on the RA, DEC, and redshift coordinates of the respective BCGs for the four peaks in the red sequence luminosity distribution and implement our GMM on possible models ranging from a single halo to four (see Tables 6 and 7). The lowest BIC model is the single halo model. At first, this is unexpected given the clear multi-modality in the projected distribution of red sequence light and the clear merger scenario presented in the literature. However, this discrepancy between the literature and our GMM results in to be expected because the cluster is extremely massive, so small velocity differences are hard to detect, which effectively reduces the GMM to a two dimensional test. Furthermore, the projected offsets are very small, so it is more economical to place a single halo covering all of the data than to add model parameters in order to split the data. This scenario is challenging in general for the GMM in use here.

Given the completeness of the spectroscopy in A2163 and the clear evidence for a major merger, we altered some of the basic inputs for this cluster. We placed a variable velocity dispersion prior on each subcluster. Table 6 lists the priors for the RA, DEC, and redshift. We allowed halos a, c, and d to have velocity dispersions between 500 and 1000 km s $^{-1}$ while subcluster b was

allowed to vary between 800 and 1400 km s $^{-1}$ since it is clearly the core of the main cluster. We also lowered the minimum subcluster size, which effectively enforces that 68% of the assigned galaxies to a given subcluster must reside within the prescribed distance. For all clusters, this prior has been allowed to vary between 0.25 and 1 Mpc. We lowered the minimum value to 150 kpc for A2163. The single halo model was still preferred; although, a three halo model is only slightly disfavored by the BIC. Interestingly, the three-halo model matches well with results in the literature. We present this model hereafter due to the abundant information indicating the cluster is in a major merger.

The projected locations of the three subclusters are presented in Figure 12 and the velocity distributions are presented in Figure 14. Subclusters 2 and 3 appear to compose the major merger. The radio relic is far to the northeast suggesting a well evolved merger. A possible scenario is that these two subclusters passed through each other long ago allowing the radio relic to reach such a distance position. More recently, the fourth subcluster that has been identified in the X-ray ([Bourdin et al. 2011](#)) as a cool-core remnant seems to have plunged through the cluster center. The galaxies associated with this subcluster are too near subcluster 2, and have been blended together. In order to offer further interpretation of the cluster merger scenario, much more detailed simulations will be necessary. A full HST mosaic of the cluster may be necessary to deblend the various mass components in the cluster center given the conflicting results from the various ground-based lensing studies.

6.13. Abell 2255

6.13.1. Literature Review

[Tarenghi & Scott \(1976\)](#) were the first to discuss A2255 as a potential merging system with fifteen spectroscopic cluster members. They used the velocity dispersion and X-ray emission to show that the system did not follow a $\sigma_v - L_X$ relation. [Hintzen & Scott \(1980\)](#) followed with a spectroscopic analysis of radio galaxies. They showed that the cluster must be $\sim 4 \times 10^{14} M_{\odot}$ in order to provide a large enough ICM halo to support the observed radio emission. [Burns et al. \(1995\)](#) presented the first multi-wavelength analysis with X-ray, radio, and optical observations. The X-ray analysis identified a potential cool core (2 keV) as opposed to the cluster global temperature of 7.3 kev. Furthermore, the cluster is reported to have a velocity dispersion of 1240 km s $^{-1}$. The two BCGs have a line of sight velocity difference in excess of 2000 km s $^{-1}$. Finally, [Burns et al. \(1995\)](#) discover a steep spectrum radio source that had been speculated to be a radio halo; however, this emission sits 0.6 Mpc to the north of the X-ray center. [Burns et al. \(1995\)](#) preferred merger scenario is a merger between the bulk of the cluster with a galaxy group; this scenario is substantiated by numerical hydrodynamical/N-body simulations, which reproduced X-ray and radio features of the cluster.

A series of X-ray and radio analyses followed and generally agreed with the previous findings. [Feretti et al. \(1997\)](#) classified the radio source as a radio relic and found the global X-ray temperature to be lower than previous findings at 3.5 ± 1.5 keV. [Davis & White \(1998\)](#) agree with [Burns et al. \(1995\)](#) with the infalling group

picture; however, they suggest a much more energetic merger between larger components that could create the observed X-ray temperature variations and offsets between the X-ray surface brightness and BCGs. [Miller & Owen \(2003\)](#) present a deep VLA 1.4 GHz analysis and detect an abnormal abundance of radio cluster members, and it is proposed that the merger phase and geometry explain the surplus. [Govoni et al. \(2005\)](#) present deeper VLA 1.4 GHz data and report strong evidence for ordered magnetic fields in the form of strongly polarized regions extending ~ 400 kpc. The radio relic sits to the northeast of the cluster center and also exhibits polarized emission. [Sakelliou & Ponman \(2006\)](#) present XMM-Newton observations of the cluster scale ICM and reach similar conclusions to previous X-ray studies. The global temperature is 6.9 keV with the east generally cooler than the west. [Pizzo & de Bruyn \(2009\)](#) detect two additional radio relic candidates with one opposite the cluster center of the previously detected northeast relic. Additionally, they study the spectral index of the radio features and find steepening in the northeast radio relic toward the cluster center. Most recently, [Akamatsu et al. \(2017\)](#) study the relic region with Suzaku and confirm the presence of a shock associated with the relic via density and temperature jumps in upstream and downstream regions relative to the relic location. The temperature ratio suggests a Mach number of ~ 1.4 , which is lower than expected from the radio data suggesting pre-accelerated electrons in the shock region.

[Yuan et al. \(2003\)](#) present a very detailed study of the galaxy population with SDSS and 13 additional filters between 3000 and 10000 Å. Photometric and spectroscopic observations resulted in more than 500 cluster members that are distributed into a single over density with east-west elongation. Several groups are identified at the periphery suggesting the cluster is still dynamically active.

6.13.2. Results

We obtained 268 spectroscopic cluster members from NED and SDSS and archival Subaru SuprimeCam imaging in B and R bands. The spectroscopic cluster members are well fit with a single Gaussian with redshift 0.08012 ± 0.00024 and velocity dispersion 1137 ± 50 km s $^{-1}$. As reported earlier, the red sequence luminosity distribution is elongated east to west. There are two BCGs in the west and one in the east of this elongation. Inspection of the two BCGs in the west suggests they are moving along the line of sight with relative velocities of ~ 2000 km s $^{-1}$. Given the presence of galaxies at each corresponding redshift in the area, we place priors for a subcluster at each redshift in projection, and a third in the east centered on the redshift and projected location of the third BCG. A total of five models ranging from a single cluster to these three subclusters are run with the GMM. The BIC score does not support multiple subclusters. We again attribute this to the spectroscopy sampling, which is too sparse in the dense cluster center to pull apart the various subcomponents.

The radio relic is situated to the northeast, but does not have a clear pair of subclusters with an orientation that easily explains its presence. However, given the potential of a three way merger with large line of sight velocities, complex merger scenarios are feasible, but they will require more spectroscopy in the cluster center along

with detailed simulations to explore in full.

6.14. Abell 2345

6.14.1. Literature Review

[Dahle et al. \(2002\)](#) performed an optical and weak lensing analysis of Abell 2345 finding that the luminosity and number density distributions of galaxies have a peak near the “well-defined core” that is dominated by a cD galaxy. However, they note that archival ROSAT X-ray images show a large amount of substructure and suggest that this is evidence that the cluster may be in a dynamically young state. They do find that the highest peak in their weak lensing map is offset east of the cD galaxy by $\sim 1.5'$, but that a secondary peak is much closer to the cD galaxy. Note that the [Dahle et al. \(2002\)](#) analysis only covers the eastern subcluster. [Cypriano et al. \(2004\)](#) also estimated the mass of the system via weak lensing but did not discuss A2345 in detail. They fit a single isothermal sphere to the convergence map and estimate $\sigma_{SIS} = 909 \pm 138$ km s $^{-1}$, which is in agreement with [Dahle et al. \(2002\)](#).

[Giovannini et al. \(1999\)](#) were the first to identify A2345 as a radio relic cluster in NVSS, identifying two extended sources and making it the second double relic system discovered (the first being A3667, [Rottgering et al. 1997](#)). [Bonafede et al. \(2009\)](#) confirmed the presence of the two relics with VLA observations at 325 MHz and 1.4 GHz. They note several discrete radio sources near the western relic, but none are expected to produce diffuse radio emission. They estimated average spectral index values of 1.5 ± 0.1 and 1.3 ± 0.1 for the eastern and western relics, respectively. [Bonafede et al. \(2009\)](#) also measured mean fractional polarizations of 14% and 22% (with values up to 55%) for the eastern and western relics, respectively. The ROSAT X-ray image of the system indicates a northwest to southeast elongation that fits the radio relic picture. They also make a rough calculation based on the approximate Mach number that the collision velocity was ~ 1200 km/s and the merger occurred ~ 0.4 Gyr before the observed state. The most recent radio analysis was completed by [George et al. \(2017\)](#) using the Murchison Widefield Array at low frequency between 88 and 215 MHz. They confirm the presence of both radio relics as well as a number of unresolved radio point sources. Spectral indices of -1.29 ± 0.07 and -1.52 ± 0.08 were measured between 88 MHz and 1.4 GHz for the east and west relics, respectively.

[Boschin et al. \(2010\)](#) conducted a redshift analysis of the system using 98 cluster member redshifts. They claim that there are three separate subclusters (E, NW, SW), based on their photometric and spectroscopic analysis with the NW and SW subclusters having similar mean velocities but ~ 800 km s $^{-1}$ velocity difference compared to the E subcluster. They claim that the NW-SW subcluster axis is a natural explanation for the western relic while the E-NW-SW subcluster axis roughly coincides with eastern relic. However, they note that if this is the case it is perhaps surprising that there is not a third relic in the south. [Boschin et al. \(2010\)](#) estimate the system mass to be $\sim 2 \times 10^{15}$ M $_{\odot}$, but they admit that it is difficult to estimate the mass of the system with galaxy velocities due to the close proximity of the subclusters in projected and redshift space. They also performed a

rough timing argument dynamics analysis of the two possible mergers. For the E and NW+SW they argue that merger axis is $\sim 40^\circ$ with respect to the plane of the sky, and is ~ 0.35 Gyr since they collided with a velocity of $\sim 2000 - 2800 \text{ km s}^{-1}$. For the NW-SW scenario they estimate that the merger axis is $\sim 2 - 20^\circ$ and that they collided ~ 0.2 Gyr ago with a velocity of $\sim 300 - 1400 \text{ km s}^{-1}$. This dynamic analysis should be considered a very rough estimate since the system is not well suited to the assumptions implicit with the timing argument (e.g. it is a multi-modal system with overlapping halos).

6.14.2. Results

We obtained the spectroscopic redshifts presented in [Boschin et al. \(2010\)](#) and combined with the available spectra from NED. We also obtained archival V and R band Subaru SuprimeCam images for our photometric analysis. The redshift distribution is well fit with a single Gaussian of redshift 0.17881 ± 0.0045 and a velocity dispersion of $1158 \pm 88 \text{ km s}^{-1}$ based upon 101 spectroscopic cluster members. This is consistent with the previous results. The red sequence luminosity map has three peaks roughly in agreement with [Boschin et al. \(2010\)](#); however, their analysis of photometric galaxies was not weighted by luminosity, and the brightest galaxies in the NW over density are situated nearly coincident with the radio relic in that direction. This is difficult to explain if the NW subcluster was involved in the merger that launched the western radio relic.

We place subcluster priors on the three luminosity peaks and center the redshift window conservatively around the respective BCG redshifts. The GMM is run for five models ranging from one to three subclusters. The BIC score prefers the single halo model, which we again attribute to the lack of spectroscopic coverage in the high density regions; although, in this case the overall number of spectroscopic cluster members is small regardless of their position. We conclude that more spectra are needed to complete a full substructure redshift analysis and report only the respective BCG redshifts for ensemble analysis in §7. Finally, we note that the X-ray surface brightness map from XMM-Newton EPIC suggests a complex merger (see Figure 16). This is anomalous among most double relic systems (e.g. A1240, CIZAJ2242, MACSJ1752, RXCJ1314, ZwCl0008, ZwCl1856) which are all clearly bimodal and aligned with the X-ray surface brightness and radio relics.

6.15. Abell 2443

6.15.1. Literature Review

A2443 was part of the MX Northern Abell Cluster Survey II ([Miller et al. 2002](#)). They obtained 12 spectroscopic redshifts of cluster members and estimate a velocity dispersion of 975 km s^{-1} . [Wen et al. \(2007\)](#) conducted a 14 medium band optical imaging survey of the A2443 where they reached a limiting magnitude of $i \sim 20$ (note that the seeing was $5.2''$). From photometric redshifts they identified 301 galaxies at the cluster redshift. In the same field they observed ZwCL 2224.2+1651 ($z \sim 0.1$) located $15.7'$ ($\sim 2.5 \text{ Mpc}$) to the southeast of A2443, but note that there is insufficient evidence to determine whether the two clusters are interacting.

A2443 appears to be elongated in the direction of ZwCL 2224.2+1651. [Wen et al. \(2007\)](#) observe that the blue fraction of galaxies is much larger in ZwCL 2224.2+1651 compared to A2443.

[Cohen & Clarke \(2011\)](#) observed A2443 in the radio from VLA at 1425, 325, and 74MHz and find a number of diffuse radio sources. Two head-tail radio galaxies in the northwest show bent tails suggesting motion towards the northwest (consistent with the elongation of the cluster) and possibly suggestive of outgoing subcluster motion post pericenter. In addition to five head-tail radio galaxies they find evidence for a diffuse radio relic with east-west elongation. While there are a number of potential point source contaminants in this region, they note that the spectral index of the diffuse emission is too steep to easily be explained by radio galaxy emission and argue that it is much more likely to be a radio relic.

[Clarke et al. \(2013\)](#) observed A2443 with 15 ks of Chandra X-ray observations and found evidence that the ICM is highly disturbed and elongated along a northwest to southeast axis consistent with the elongated galaxy distribution. They also find two X-ray surface brightness edges, one along the northeast face and one along the southeast face. The southeast edge is largely coincident with the radio relic candidate from [Cohen & Clarke \(2011\)](#), suggesting that it may be the result of shocked ICM from a merger.

6.15.2. Results

We observed A2443 with two slitmasks with Keck DEIMOS, combined the spectroscopy with archival data, and obtained 157 cluster members. A2443 is the only cluster in our sample without Subaru SuprimeCam imaging; however, the cluster is covered with SDSS and is of sufficiently low redshift such that the SDSS imaging is sufficient to trace the red sequence. The spectroscopy is well fit by a single Gaussian with redshift 0.10979 ± 0.00023 and velocity dispersion $780 \pm 45 \text{ km s}^{-1}$ which is $\sim 200 \text{ km s}^{-1}$ less than previous results based upon far fewer galaxies.

We utilized SDSS g and r band catalogs to map the red sequence. The cluster is elongated and bimodal along a southeast to northwest axis in agreement with the X-ray emission. We placed subcluster priors on the respective BCGs in the northwest and southeast and ran one and two subcluster models with the GMM. The two halo model was preferred according to the BIC score, and the results suggest a plane of the sky merger with an unequal mass ratio.

The radio relic in A2443 is unlike other relics in our sample. It is the only “roundish” relic ([Feretti et al. 2012](#)) in our sample, and the ultra-steep spectrum and proximity to the cluster center suggests it is a radio phoenix class relic. These greatly differ from the larger scale relics such as the Toothbrush and Sausage relics found in 1RXSJ0603 and CIZAJ2242, respectively. Phoenixes appear to be more closely linked with the more localized radio plasma of AGN. This explains why the relic is positioned much closer to the center of the cluster than others in our sample. This also suggests that the shock is much closer to the center of the cluster than other systems, which implies that A2443 is a young merger. The small projected offset between subclusters supports this picture.

6.16. Abell 2744

6.16.1. Literature Review

A2744 is an extremely well observed and analyzed cluster, and is known to be a complex system with multiple merging subclusters (see e.g. Merten et al. 2011). The first indications of merger activity came from the detection of a radio halo and radio relic (Giovannini et al. 1999; Govoni et al. 2001a,b). The relic is situated to the northeast of the halo and has a linear extent of ~ 2 Mpc. Kempner & David (2004) presented the first detailed X-ray analysis with Chandra and concluded a major merger is occurring north to south with a large line of sight velocity component. Additionally, a smaller northwest component is infalling creating a possible bow-shock. Owers et al. (2011) generally agreed with this picture and with deeper Chandra observations detect a shock to the southeast of the cluster center. Note that no shock is identified to lie coincident with the radio relic. Owers et al. (2011) also presents a detailed galaxy analysis with ~ 300 spectroscopic cluster members. Evidence for three subclusters indicate a major north to south merger. They also find an interloping subcluster associated with the northwest ICM component identified in the X-ray observations. The main two components (north and south) have a large velocity difference, which substantiates the large line of sight component to the merger axis. More recently, Eckert et al. (2016) detected a shock coincident with the radio relic using XMM-Newton and Suzaku data. Most recently, George et al. (2017) used the Murchison Widefield Array to study the low frequency radio emission of the cluster between 88 MHz and 215 MHz. The radio halo and relic were detected at all observed frequencies. The spectral index between 88 MHz and 1.4 GHz was measured to be -1.09 ± 0.05 and -1.01 ± 0.07 for the halo and relic, respectively.

A2744 is a member of the Frontier Fields (Lotz et al. 2014) sample of clusters, and thus the deep HST observations have allowed for very detailed strong lensing analyses of the core of the mass distribution. Merten et al. (2011) presented the first joint strong/weak lensing analysis along with X-ray and galaxy analyses. It was found that A2744 is a complex merger with unique subclusters including an enhanced ram-pressure slingshot (see e.g. Hallman & Markevitch 2004). Merten et al. (2011) estimated the self interaction cross section of dark matter based on offsets between X-ray and lensing peaks resulted in one of the first upper limits of $\sigma_{DM} < 3 \pm 1 \text{ cm}^2 \text{ g}^{-1}$.

Several lens models have been calculated for A2744 (Lam et al. 2014; Johnson et al. 2014; Jauzac et al. 2015; Kawamata et al. 2016; Mahler et al. 2017). These strong lensing analyses mainly probe the cluster center where a large line of sight velocity difference between at least two subclusters has been identified. Updated strong and weak lensing analyses over the wider field have confirmed a massive ($M_{200} = 2.06 \pm 0.42 \times 10^{14} \text{ M}_\odot$) and complex merging system (Jauzac et al. 2016; Medezinski et al. 2016). Interestingly, the results in Medezinski et al. (2016) confirm large offsets between mass, galaxy, and X-ray components ($\sim 70\text{--}80''$).

Additional evidence relating to the merger includes the discovery of four jellyfish type galaxies undergoing recent starburst (Owers et al. 2012). Further study of the

star formation in cluster galaxies have found evidence of shock induced star formation (Rawle et al. 2014). The number of massive halos have raised the question of compatibility with Λ CDM structure formation models. Jauzac et al. (2016) searched for analogs in the MXXL simulation (Angulo et al. 2012), and Schwinn et al. (2017) use extreme value statistics to estimate that a volume ten times the MXXL volume would be required to find an analog.

6.16.2. Results

We utilized archival spectroscopy from NED and B and R band images from Subaru SuprimeCam. The spectroscopic catalog of 380 galaxies is well fit by a single Gaussian despite the clear multi-modality in the red sequence luminosity map. The global cluster redshift and velocity dispersion are 0.30590 ± 0.00035 and $1602 \pm 61 \text{ km s}^{-1}$, respectively. The red sequence luminosity distribution has three distinct peaks. The cluster core has a line of sight bimodal distribution of redshifts (Owers et al. 2011; Mahler et al. 2017) (see Figure 9). The northern peak in the red sequence luminosity distribution is elongated east to west and coincident with two peaks identified in lensing studies. Additionally there is a lower redshift, western peak associated with a known lensing over-density. We place five subcluster priors conservatively on these galaxy light peaks and set redshift priors based on the BCG redshifts of the respective subclusters. A2744 is the most complicated cluster of our sample, and we run 27 separate models with our GMM ranging from one to five subclusters.

The lowest BIC model is a four component model with the northern luminosity peak merged into a single subcluster, and the main halo center (where strong lensing analyses have been completed) split into two line of sight groups with a large line of sight velocity difference, and a fourth subcluster associated with the westernmost luminosity peak (see Figure 12). There is no obvious pair of subclusters aligned to explain the radio relic in the east; however, subcluster 1 has an east to west elongation. Given the complex state of the merger, it is difficult to fully explore merger scenarios without detailed simulations. Inspecting the X-ray surface brightness (Figure 16) indicates that the northern luminosity peak is actively merging given the large displacement between cluster light and the ICM. Furthermore, subcluster 4 (in the west) appears to have disrupted the ICM suggesting it has passed from east to west to reach its present position.

6.17. Abell 3365

6.17.1. Literature Review

A3365 is a little studied system with one radio relic and one radio relic candidate discovered in NVSS and observed with VLA and WSRT at 1.4 GHz (van Weeren et al. 2011b). They observed the cluster with INT and generated galaxy number density contours which suggest three separate galaxy peaks. One of the peaks is another cluster (RXC J0548.8-2154), which sits $9'$ to the west of the center of A3365 at the same redshift. van Weeren et al. (2011b) determined that together the system composed of A3365 and RXC J0548.8-2154 comprise the merging system. The X-ray peak is located closer to

RXC J0548.8-2154, but is clearly disturbed. We will refer to the whole system as A3365.

6.17.2. Results

We obtained spectroscopic redshifts with five Keck DEIMOS slitmasks and photometry in g and r bands with Subaru SuprimeCam. The spectroscopic survey resulted in 150 cluster members well fit with a single Gaussian of redshift 0.09273 ± 0.00028 and velocity dispersion $981 \pm 58 \text{ km s}^{-1}$. The red sequence luminosity distribution has three peaks. Two of these have similar redshifts, and the western-most has a higher redshift with a peculiar velocity of $\sim 1900 \text{ km s}^{-1}$. We place subcluster priors on each over-dense region with redshift windows conservatively straddling the respective BCG redshifts. We run one, two, and three component models with the GMM and find the three component model best fits the data according to the BIC score.

Inspection of the projected (RA, DEC) space distribution of the three subclusters suggests the east and middle subclusters likely merged to launch the shock associated with the radio relic. There is no clear alignment of subclusters with the radio relic candidate, which sits just north of the middle subcluster. These subclusters have similar redshifts, while the west subcluster has a large peculiar velocity. The east subcluster contains most of the mass of the cluster given its higher velocity dispersion.

Inspection of the X-ray surface brightness map substantiates the merger picture between the east and middle subclusters. The gas has mostly stayed in the east and been stripped from the middle subcluster in its apparent westward trajectory. Within the east, there are two bright galaxies along the extended ICM, which may indicate ongoing merger activity within the east. Finally, although at the edge of the XMM field of view, the western subcluster appears to have its ICM coincident with the galactic light distribution suggesting it has not yet merged.

6.18. Abell 3411

6.18.1. Literature Review

A3411 was included in the CIZA cluster catalog [Ebeling et al. \(2002\)](#) and Planck SZ cluster catalog [Planck Collaboration et al. \(2011\)](#), but [van Weeren et al. \(2013\)](#) were the first to publish a detailed analysis of this system. Their shallow (10 ks) Chandra X-ray map showed that the cluster gas has a cometary shape with the head located near the center of the northern subcluster (A3411) and the tail pointing in the direction of the southern subcluster (A3412), providing clear evidence that this is a dissociative cluster merger. Their VLA 1.4 GHz observations show diffuse emission near the northern subcluster, which they classify as a halo despite being highly elongated, and diffuse emission near the southern subcluster, which they class as a radio relic. They find that the southern radio relic is peculiar due to its fragmented morphology and suggest that this may be due to interactions with cosmic filaments or that it may reflect the presence of electrons in fossil radio bubbles that are being re-accelerated by the passing shock. [Giovannini et al. \(2013\)](#) largely confirm the [van Weeren et al. \(2013\)](#) findings and add that the average polarization of the radio relic is $\sim 20\%$.

[van Weeren et al. \(2017\)](#) identified a direct connection between a cluster member AGN and a portion of the radio relic and showed spectral aging across the radio jet portion connecting the relic to the galaxy. They then found an X-ray shock in deeper Chandra data and showed that the spectral index changed near the shock. The shock has a low Mach number ($\mathcal{M} < 1.7$) and would be unable to generate enough acceleration to observe the radio relic were it not for the pre-accelerated plasma from the AGN. This was the first direct observation of an AGN/shock connection in this manner and the clearest evidence yet that radio relics may be intimately connected to the AGN population. Also presented in [van Weeren et al. \(2017\)](#) are four of five of our DEIMOS slitmasks and our g and i band SuprimeCam imaging. A bimodal galaxy distribution is identified with equal masses from velocity dispersions. The masses and redshifts of the subclusters are combined with the projected separation and input into the MCMAC dynamics code ([Dawson 2014, 2013](#)) to estimate merger parameters. A3411 is found to have a 3D collision speed of $\sim 2600 \text{ km s}^{-1}$. A3411 is observed near apocenter, and within $\sim 45^\circ$ of the plane of the sky at 95% confidence.

6.18.2. Results

We have since added an additional slitmask of spectroscopic data from Keck DEIMOS in the eastern edge of the cluster. With this mask, the total number of cluster members increases from 174 (presented in [van Weeren et al. 2017](#)) to 242. The global velocity distribution is well fit by a single Gaussian with redshift 0.16225 ± 0.00030 and velocity dispersion 1239 km s^{-1} in agreement with [van Weeren et al. \(2017\)](#). The red sequence luminosity distribution is largely bimodal with a lower peak on the eastern edge of the north to south elongation and a significant peak to the north of the main two subclusters.

We run the GMM with models ranging from one to three subclusters. The lowest BIC model matches the bimodal picture presented in [van Weeren et al. \(2017\)](#) with two nearly equal, large subclusters arranged north to south. We note that the merger between these two likely did not cause the shock that is associated with the AGN and analyzed by [van Weeren et al. \(2017\)](#). Instead, that shock is likely associated with an optically poor group presently in the eastern flank of the cluster. The main merger likely created the shock that is far to the south and spawned the patchy relic morphology in the south. The X-ray surface brightness fits the picture of the main merger with a cool-core remnant in the north and a trailing wake feature back toward the south. Lensing studies and updated dynamical modeling are required to further understand the cluster's mass distribution and merger history. Low frequency radio observations may help explain the patchy radio relic morphology and associated shock; although, since the ICM is diffuse in the south, a direct X-ray shock is unlikely to be detected without an extremely deep Chandra image.

6.19. CIZA J2242.8+5301

6.19.1. Literature Review

CIZAJ2242 (a.k.a. the Sausage Cluster) was first discovered by [Kocevski et al. \(2007\)](#) in the second CIZA

sample. The cluster is situated behind the plane of the galaxy as observed from Earth (although it is away from the bulge). This explains the high extinction $A_v = 1.382$. This is likely the reason for the dearth of optical studies of the system prior to the Merging Cluster Collaboration's analysis (Stroe et al. 2014b; Jee et al. 2015; Dawson et al. 2015; Stroe et al. 2015; Sobral et al. 2015).

van Weeren et al. (2010) conducted the first comprehensive radio study of the system (including WSRT, GMRT, and VLA observations) with which they observed evidence of shock acceleration and spectral aging associated with the outward-moving shock. This was later confirmed with the follow-up study of Stroe et al. (2013). van Weeren et al. (2010) also observed that the northern relic is strongly polarized at the 50-60% level, and used this to infer that the merger angle must be within $\sim 30^\circ$ of the plane of the sky. They also used the spectral index to infer a Mach number of ~ 4.6 . Stroe et al. (2014c) observed with the system with the Arcminute Microkelvin Imager at 16 GHz and presented the first high frequency detection of diffuse radio emission associated with clusters. They found diffuse emission at the northern radio relic but note that the detected flux is inconsistent with diffusive shock acceleration predictions. Recent simulations suggest that adjusting the pre-existing fossil population, magnetic fields, and/or turbulence can help explain this spectral steepening above 2 GHz (Kang & Ryu 2016; Donnert et al. 2016; Fujita et al. 2016). Stroe et al. (2014a) studied the spectral age of radio features in the cluster. They found that individual galaxies with radio lobes appeared to be traveling either north or south indicating the relative motion of the sub-clusters within the plane of the sky. Note this is based on a few galaxies, which could occur by chance.

van Weeren et al. (2011a) conducted a suite of simulations studying potential analogs to the system and argue that the cluster is probably undergoing a merger in the plane of the sky (less than 10° from edge-on) with a mass ratio of about 2:1, and an impact parameter of 400 kpc. The core passage of the clusters happened ~ 1 Gyr ago. Kang et al. (2012) conducted diffusive shock acceleration simulations of the Sausage and found that Mach numbers from 2.0–4.5 were supported depending on the amount of pre-existing cosmic ray electrons. However, they question the ability of the merger event to produce such an elongated shock.

Kierdorf et al. (2016) studied the relic at 4.85 and 8.35 GHz with the 100-m Effelsberg telescope. They observe a variable polarization fraction from $\sim 55\%$ at the eastern end of the northern relic to $\sim 25\%$ at the western end. These values are in agreement with those estimated by van Weeren et al. (2010) at higher resolution, which suggest the magnetic fields are ordered on scales larger than the Effelsberg beam (300 kpc).

Three detailed X-ray analyses have been conducted, one with XMM-Newton (Ogurian et al. 2013b,a) and two with Suzaku (Ohashi et al. 2013; Akamatsu & Kawahara 2013). The results from XMM-Newton show an extreme north to south elongation of the X-ray gas largely consistent with the merger axis suggested by the radio relics. The XMM instrumental background levels prevent characterization of the surface brightness profile at the location of the northern radio relic. Suzaku observations near the southern radio relic provide evidence for a shock with

Mach number ~ 1.2 -1.3. Ogurian et al. (2013b,a) also note two interesting features of the gas. The first is a “wall” of hot gas east of the cluster center, and while not associated with a radio relic it does extend into the region behind the northern relic; they suggest that it may be indicative a more complex merger scenario. The second feature is a “smudge” of enhanced X-ray emission coincident with the eastern portion of the northern radio relic. Akamatsu & Kawahara (2013) found evidence for temperature jump at the location of the northern radio relic corresponding to a Mach number of 3.15 ± 0.52 , while lower than that predicted by the radio (4.6 ± 1.3 ; van Weeren et al. 2010) they are consistent within the 68% confidence intervals. They did not see a jump in the surface brightness profile, but they claim that this is due to the large Suzaku PSF (~ 380 kpc) being much larger than the width of the relic (~ 50 kpc). Note that they do not observe a significant temperature jump in the region east of the cluster.

The Merging Cluster Collaboration completed a detailed optical analysis of the system. Stroe et al. (2014b) conducted an H α survey of the cluster and find an order of magnitude boost in the normalization of the galaxy luminosity function in the vicinity of the relics, even greater than that of other known mergers at the same redshift. Jee et al. (2015) presented the first weak lensing analysis with the Subaru imaging described in §3.1. Despite the large and variable extinction, the data show a massive and bimodal system with a north to among the dDEIMOS spectroscopy south orientation that largely agrees the red sequence galaxies. The cluster as a whole is found to be very massive ($M_{200} = 11.0^{+3.7}_{-3.2} \times 10^{14} M_\odot$ and $9.8^{+3.8}_{-2.5} \times 10^{14} M_\odot$ for the northern and southern sub-clusters respectively). The galaxy luminosity and weak lensing mass peaks exhibit a ~ 190 kpc offset at a $\sim 2\sigma$ level. Dawson et al. (2015) present a subcluster and redshift analysis using our Subaru SuprimeCam imaging and Keck DEIMOS spectroscopic data. The subcluster algorithm is an expectation-maximizing GMM analysis suitable for simpler bimodal systems. The north and south subclusters are found to have similar line of sight velocities ($\Delta v = 69 \pm 190$ km s $^{-1}$). The velocity dispersions of the two subclusters indicate a 1:1 mass ratio in agreement with the lensing study. Finally, Sobral et al. (2015) analyzed 83 H α emitters among the DEIMOS spectroscopy and find that star-formation is boosted in the hottest X-ray regions near the subcluster cores. Additionally, evidence is found for enhancement from passing shocks in metal-rich galaxies.

Okabe et al. (2015) present a weak lensing analysis using a color-color selection, which is in principle more effective than the Jee et al. (2015) color-magnitude selection and find the southern subcluster to be two times more massive than the south. They also find the total mass to be $\sim 50\%$ of the mass as Jee et al. (2014), but the difference between the two masses are consistent within the uncertainty of the respective results.

Most recently, Molnar & Broadhurst (2017) completed a suite of hydrodynamical simulations finding a 1.3:1 mass ratio with a total mass of $\sim 1 \times 10^{15} M_\odot$ best describes the observations.

6.19.2. Results

Using the same spectroscopy and imaging as Dawson et al. (2015), we find the global redshift distribution to be well fit with a single Gaussian of redshift 0.18865 ± 0.00032 and velocity dispersion 1184 ± 64 km s $^{-1}$ in agreement with Dawson et al. (2015). The red sequence luminosity distribution is clearly bimodal. We fit one and two subcluster models with the GMM and find the two halo model. The two subclusters are similar in redshift and well aligned with the two radio relics and the extension of the ICM. CIZAJ2242 is a very clean, bimodal system with a simple geometry. Subclusters 1 and 2 have redshifts and velocities in good agreement with Dawson et al. (2015); although, the south subcluster has a slightly higher velocity dispersion instead of the north. These results show that our MCMC-GMM recovers the results of packaged EM-GMM codes on simple geometries.

6.20. MACS J114934.3+222342

6.20.1. Literature Review

Ebeling et al. (2007) were the first to report on MACSJ1149 as part of the MAssive Cluster Survey (MACS; Ebeling et al. 2001). Ebeling et al. (2014) followed up with Gemini GMOS and Keck DEIMOS spectroscopy. Of the MACS clusters, MACSJ1149 has the highest reported velocity dispersion of ~ 1800 km s $^{-1}$ as well as an X-ray luminosity of $\sim 18 \times 10^{44}$ erg s $^{-1}$ and temperature of ~ 9 keV (Ebeling et al. 2007). Smith et al. (2009) followed with a strong lensing analysis of the system based on HST/ACS imaging and Keck spectroscopic confirmation of multiply imaged galaxies finding a mass within 500 kpc of $6.7 \pm 0.4 \times 10^{14} M_{\odot}$. They found the core to be composed of a dominant structure associated with the BCG along with three additional massive halos along a northwest-southeast axis. Zitrin & Broadhurst (2009) published an independent strong lensing analysis and noted the largest known lensed image of a single spiral galaxy. This galaxy is a face-on spiral at a redshift of 1.49 and has been multiply imaged. One of these images contained a supernova, which in turn was multiple imaged by a cluster galaxy into an Einstein cross pattern. The supernova appeared in another of the images predictably and the time difference between the appearance of the supernova can be used to constrain cosmology and the lens model of MACSJ1149 (Refsdal 1964; Kelly et al. 2015; Sharon & Johnson 2015; Oguri 2015; Diego et al. 2016; Treu et al. 2016). Zitrin & Broadhurst (2009) argue that a nearly uniform mass distribution over a 200 kpc radius with a surface density near the critical density is needed to explain the small amount of image distortion in this spiral. Zheng et al. (2012) used the cluster's powerful magnification to discover a $z \sim 10$ galaxy. These results are largely thanks to MACSJ1149 being selected as part of the Cluster Lensing and Supernova Survey (CLASH; Postman et al. 2012) and as part of the HST Frontier Fields program (Lotz et al. 2014). CLASH studied MACSJ1149 with ground based weak lensing with Subaru/SuprimeCam (Umetsu et al. 2014), and with a joint weak and strong lensing analysis utilizing Subaru SuprimeCam and HST ACS (Umetsu et al. 2015), respectively. Both analyses resulted in extremely high masses for M_{200} : $25.4 \pm 5.2 \times 10^{14} M_{\odot}$ and $25.02 \pm 5.53 \times 10^{14} M_{\odot}$. MACSJ1149 is among the most

massive clusters (Planck Collaboration et al. 2016).

Bonafede et al. (2012) presented the first radio analysis with evidence for three diffuse sources including a radio relic southeast and a candidate relic west of the cluster and a candidate radio halo as well. The radio halo has an extremely steep spectral index between 323 MHz and 1.4 GHz: $\alpha \approx 2$ indicating the cluster merger is not recent and/or the (re)acceleration process was not efficient (Brunetti et al. 2008). The relics are not situated symmetrically with the extended ICM and mass distribution; the southeast relic is collinear, but the western relic candidate is nearly perpendicular to the merger axis suggesting it may actually not be a shock-tracing relic.

Ogurian et al. (2016) presented a deep (365 ks) Chandra X-ray analysis. MACSJ1149 is found to be among the most X-ray luminous ($L_{X,[0.1-2.4\text{keV}]} = (1.62 \pm 0.02) \times 10^{45}$ erg s $^{-1}$) and hottest ($T_X = 10.73^{+0.62}_{-0.43}$ keV) clusters known. X-ray surface brightness appears to be relatively regular for a multi-component merger indicating that MACSJ1149 could be an old merger in agreement with the steep spectral index of the candidate radio halo. A weak cold front to the northeast of the cluster was found as well as a possible surface brightness edge that could be the leading bow shock may indicate that merger activity is still present or that sloshing may be occurring in the ICM.

Using the archival Subaru SuprimeCam imaging and Keck DEIMOS and Gemini GMOS spectroscopy we completed a subcluster and redshift analysis (Golovich et al. 2016). A second massive subcluster is discovered to the south that extraordinarily lacks an associated X-ray peak. We interpreted that the merger between the northern subcluster (which has been extensively studied as part of CLASH and the Frontier Fields) and the southern subcluster stripped the gas of the southern subcluster. This merger occurred mostly in the plane of the sky ($\Delta v_{LOS} \sim 300$ km s $^{-1}$). A dynamics analysis shows the merger to be similar to El Gordo (Ng et al. 2015) in terms of its age and merger velocity. A third subcluster is identified to be merging with the northern subcluster along the line of sight, which perhaps provides explanation for the cold front discovered by Ogurian et al. (2016).

6.20.2. Results

Here we re-evaluate the substructure with our analysis scheme utilized in this paper. This is largely similar to the analysis presented in Golovich et al. (2016) with only minor changes, and we complete our analysis routine here for completeness. This will also test that slight changes in the redshift analysis do not significantly alter results. Our shrinking aperture technique results in 260 spectroscopic cluster members within R_{200} (as opposed to 278 in Golovich et al. (2016)). The global redshift distribution is well fit by a single Gaussian with a redshift of 0.54362 ± 0.00052 and velocity dispersion 1668 ± 76 km s $^{-1}$, making MACSJ1149 the highest redshift system in our sample.

We placed subcluster priors on the two bright subcluster peaks in the red sequence luminosity distribution as well as a broad, uninformative prior covering the northern extension of the red sequence luminosity distribution with a large peculiar line of sight velocity difference. This potential subcluster is evident in the DS-test with

the group of red circles in the north of the cluster. We run models with one to three subclusters and identify the three subcluster model to have the lowest BIC score. The three halo model is in good agreement with the results of Golovich et al. (2016).

6.21. MACS J175201.5+444046

6.21.1. Literature Review

MACSJ1752 was discovered as a bright X-ray source in ROSAT and confirmed spectroscopically by Ebeling et al. (2001). MACSJ1752 was first reported as a candidate radio relic cluster by Edge et al. (2003), although only in passing. van Weeren et al. (2012a) observed MACSJ1752 with the WSRT and found radio relics with sizes 1.3 and 0.9 Mpc, in the northeast and southwest respectively. They also measured integrated spectral indices of -1.16 and -1.1, suggesting shocks with Mach numbers of 3.5–4.5. They argue that the radio relics and X-ray distribution suggest a 2:1 mass ratio binary event that occurred with an impact parameter about four times the core radius of the larger subcluster. They also note a possible radio halo associated with the system. Bonafede et al. (2012) observed the system with GMRT and confirmed both the radio relics and radio halo. They find spectral indices in good agreement with the van Weeren et al. (2012a) measurements. Bonafede et al. (2012) also resolve spectral steepening across each of the relics, similar to that seen in the CIZAJ2242. They find that the NW relic has an average polarization of 20% with values up to 40%, and the SW relic has an average polarization of 10% with values up to 40%, with the higher polarization seen at the outer edge of the relics. They suggest that this decrease towards the inner edge could be due to turbulent motions developing after the shock randomizing the magnetic field. The northeast relic is among the brightest relics known, with similar brightness and morphology as the northern radio relic of PSZ1G108 (de Gasperin et al. 2015).

6.21.2. Results

We observed MACSJ1752 with four Keck DEIMOS slitmasks and with Subaru SuprimeCam in g, r, and i bands. The spectroscopic survey resulted in 176 cluster member galaxies within R_{200} . The red sequence luminosity map is badly affected by a very bright star near the northeast BCG. Before a full galaxy and lensing analysis can be completed, this stellar profile must be subtracted in a manner similar to the method presented in Jee et al. (2016). This star also hindered the spectroscopic survey since SDSS imaging was used for targeting, and SDSS did not detect objects in the vicinity of the star. To detect the northeast BCG spectroscopically we placed a slit manually. We still detected many galaxies to the north and west of the BCG, so we proceed with a subcluster analysis here. We centered subcluster priors on the two BCGs with conservative projected position and redshift ranges. We ran one and two subcluster models, and the two subcluster model was preferred, although only slightly. We suspect more spectroscopic completion near the core of the northeast subcluster will improve the BIC of a two halo model.

The two subclusters have similar redshifts and velocity dispersions suggesting a 1:1 merger in the plane of the

sky. The X-ray surface brightness distribution shows two “bullet-like” gas cores that are nearly coincident with the red sequence luminosity peaks. The survival of the two cores suggests a merger with a non-zero impact parameter. Although, the radio relics, galaxies, and ICM are all approximately collinear along a northeast to southwest axis.

6.22. PLCKESZ G287.0+32.9

6.22.1. Literature Review

PLCKG287 is the second most significant SZ detected cluster of the 20 new clusters in the Planck Early Release Catalog (Planck Collaboration et al. 2011) (after only Abell 2163). Bagchi et al. (2011) observed PLCK G287 with GMRT at 150 MHz and VLA at 1.4 GHz and discovered a pair of radio relics, that have a very large projected separation of 4.4 Mpc. They also identify a potential radio halo closer to the cluster center. Bagchi et al. (2011) found evidence for PLCKG287 being a post merger system with optical imaging from the IUCAA 2m and a shallow 10 ks XMM-Newton observation. They estimate a SZ and X-ray based masses of $M_{500} = 25 \pm 1.0 \times 10^{14}$ and $26 \pm 1.0 \times 10^{14} M_{\odot}$, respectively. These masses are consistent with the weak lensing based mass of Gruen et al. (2014): $M_{200} = 53 \pm 13 \times 10^{14} M_{\odot}$ and $M_{500} = 28 \pm 5.0 \times 10^{14} M_{\odot}$. Gruen et al. (2014) also noted a number of exceptional strong lens arc-like features. The two most separated features are 165'' apart. This is much larger than the expected Einstein radius of 37'' given the 68% upper confidence NFW fit and assuming a source redshift of 5. Thus it is called into question whether these arcs are actually multiple images. Zitrin et al. (2017) completed a strong lensing analysis with HST imaging and 20 sets of multiple images. A high-redshift dropout galaxy is identified with a photometric redshift of ~ 7 , and the critical area for $z \sim 10$ source galaxies is found to be 2.58 arcmin² making PLCKG287 the largest known cosmic lens.

Bonafede et al. (2014) observed PLCK G287 with GMRT at 150, 325, and 610 MHz. They determined that the northern most relic identified by Bagchi et al. (2011) is actually a radio galaxy with two lobes and some other point sources, however the northern relic closest to the cluster and the southern relic (2.8 Mpc from center) are confirmed. Bonafede et al. (2014) make the argument that the small projected distance of the northern relic and the large projected distance of the southern relic is due to two separate passes of a merging subcluster ($\sim 10\%$ of the mass of the main cluster). Most recently, George et al. (2017) observed the cluster with the Murchison Widefield Array at 88, 118, 154, 188, and 215 MHz. The two radio relics and halo are confirmed at each frequency. The northwest and southeast relics have spectral indices between 88 MHz and 3 GHz measured to be -1.19 ± 0.03 and -1.36 ± 0.04 , respectively. The radio halo was blended with several point sources, and no spectral index was estimated.

6.22.2. Results

We observed PLCKG287 with three Keck DEIMOS slitmasks and with Subaru SuprimeCam in g and r bands. We also obtained spectroscopy from VLT GMOS (M. Giardini, M. Nonino, private communication). These spec-

tra will be presented in a more detailed spectroscopic and photometric analysis in a forthcoming paper (Girardi et al. in prep.). The spectroscopic survey results in 302 spectroscopic cluster members well fit by a single Gaussian with redshift 0.38321 ± 0.00046 and velocity dispersion $1756 \pm 74 \text{ km s}^{-1}$. The red sequence luminosity distribution is dominated by a single peak with a much weaker peak sitting ~ 2 Mpc to the south. The DS-test corroborates this peak with a collection of blue circles in the vicinity. We placed subcluster priors over the two luminosity peaks and ran one and two halo models with the GMM. The two models have similar BIC scores with the two halo model only slightly preferred.

The main subcluster of PLCKG287 has an extreme velocity dispersion, and the second subcluster is situated near the south radio relic, which would be unexpected in a bimodal merger scenario. The relative positions of the two radio relics has been discussed with a proposal for a two core passage model by Bonafede et al. (2014). A second explanation could be an unequal mass merger. If these two subclusters merged to launch the underlying shocks in a single event, we would expect the southern relic to be much further from the center of mass since the much less massive southern subcluster will have merged extremely fast in the center of mass frame, launching the shock at approximately its merger velocity. Taking the center of mass to be the center of the main cluster, the approximate relic distances are 2.75 and 0.69 Mpc, which would indicate a 4:1 mass ratio merger. However, based on the velocity dispersions of the two GMM subclusters, the mass ratio is $\sim 10:1$, which similar to the Bullet Cluster.

The weak lensing analysis of Gruen et al. (2014) did not detect a second massive peak in the south. The X-ray surface brightness map does not reveal obvious X-ray emission indicating a separate ICM peak associated with the subcluster in the south. This could indicate that it has been stripped, or that the subcluster is very low mass. The bimodal merger picture is complicated further by the relative position of the relic and galaxies. The shock should run ahead occur as the subcluster approaches apocenter, but the subcluster is unexpectedly far from the center of the cluster. A more detailed lensing analysis with our Subaru imaging is forthcoming (Finner et al. in prep), and will be necessary to examine this further.

In the scenario proposed by Bonafede et al. (2014), where the south relic was launched at first core passage, and the north relic is launched during a more recent second core passage by the original infalling subcluster (note this model does not include the southern subcluster detected by our GMM), one complicating factor is the bright southern relic. The radio emission of a radio relic is believed to be short-lived (Skillman et al. 2013). A possible explanation is a scenario similar to Abell 3411. The cluster galaxies in the south could host an AGN that has created a region of mildly relativistic fossil electrons that are now being reaccelerated by the passing shock. Deeper X-ray and radio observations in this region would be necessary to search for such a scenario.

6.23. PSZ1 G108.18-11.53

6.23.1. Literature Review

PSZ1G108 is a very little studied system that first was discovered recently by Planck Collaboration et al. (2014) using its SZ signal. The cluster mass was later estimated by the Planck Collaboration to be $M_{500} = 7.7 \pm 0.6 \times 10^{14} \text{ M}_\odot$ (Planck Collaboration et al. 2016). de Gasperin et al. (2015) completed the only detailed analysis of the cluster and found it hosts one of the most powerful pair of radio relics known to date in addition to a radio halo with WSRT and GMRT in several frequencies. The injection spectral index of the northern and southern relic was found to be -1.02 and -1.17, respectively. The relics notably comprise the second most powerful radio system known at 1.4 GHz ($L = 44.6 \pm 0.3 \times 10^{24} \text{ W Hz}^{-1}$). Each relic shows 10–30% polarized emission. ROSAT show the X-ray emission to be centered between the two relics, but the data are insufficient to detect merger activity. The estimated luminosity is $L_X \sim 7.5 \times 10^{44} \text{ erg s}^{-1}$ based on the ROSAT emission, and using the (L, T) scaling relations provided by Pratt et al. (2009) a temperature of 6.5 keV was reported.

6.23.2. Results

We observed PSZ1G108 with two slitmasks on Keck DEIMOS and in g and r bands on Subaru SuprimeCam. Unfortunately, tracking problems made the SuprimeCam images unusable, so we make use of DSS images to trace the red sequence. The 40 spectroscopic galaxies are well fit by a single Gaussian in redshift space with a global redshift of 0.33494 ± 0.00059 and velocity dispersion $873 \pm 90 \text{ km s}^{-1}$. The red sequence distribution is elongated along the same axis as the two radio relics. The data are insufficient to complete a subcluster analysis, so we present only a single halo GMM model.

The X-ray surface brightness map indicates a main ICM peak near the middle of the cluster equidistant from the two relics with X-ray emission streaming northward toward the bright northern relic. Deeper X-ray observations along with photometry and spectroscopy are needed to study this system in detail.

6.24. RXC J1053.7+5452

6.24.1. Literature Review

RXCJ1053 is a little studied cluster although it appears in both SDSS and REXCESS cluster catalogs. Aguera et al. (2007) reported a velocity dispersion of $\sim 650 \text{ km s}^{-1}$. Rudnick & Lemmerman (2009) made the first mention of a radio relic with an extent of 1 Mpc and a low flux. van Weeren et al. (2011b) presents the WSRT 1382 MHz observations and finds a weak radio relic in the west. A general bimodal picture is found with the X-ray emission between the two galaxy peaks and the radio relic along the same axis. Between the low velocity dispersion, weak radio emission ($0.2 \times 10^{24} \text{ W Hz}^{-1}$), and low X-ray luminosity ($L_X = 0.44 \times 10^{44} \text{ erg s}^{-1}$) the system appears to be a low mass merger.

6.24.2. Results

We observed RXCJ1053 with four slitmasks of Keck DEIMOS spectroscopy and in g and r bands with Subaru SuprimeCam. The spectroscopic survey resulted in 119 cluster members within R_{200} very well fit by a single Gaussian with redshift 0.07217 ± 0.00021 and velocity dispersion $653 \pm 41 \text{ km s}^{-1}$ in agreement with Aguera

[et al. \(2007\)](#). RXCJ1053 is the lowest redshift cluster in our sample as well as the cluster with the lowest velocity dispersion. The red sequence luminosity distribution is aligned along a southeast to northwest axis with the relic at the northwest end. There are three red sequence luminosity peaks with the brightest peak in the middle but the BCG in the northwest. The southeast peak is just above our 3σ contour.

We place subcluster priors on the three peaks with conservative redshift priors and run one, two, and three halo models with the GMM. The lowest BIC model has two subclusters over the middle and northwestern peaks. Subcluster 1 (northwest) contains the cluster BCG, but it has a very low velocity dispersion. Meanwhile, subcluster 2 is slightly less settled with no dominant BCG, but it contains most of the mass of the cluster. The two subclusters are well aligned with the radio relic to the northwest, and the X-ray surface brightness distribution indicates a merger along the same axis. The brightest X-ray emission is associated with subcluster 1. Lower mass subclusters have been observed holding onto their gas (e.g. the Bullet Cluster, ZwCl0008), and often indicate a cool-core remnant. Deep X-ray observations would be necessary to fully classify RXCJ1053 as a low mass “Bullet-like” cluster.

6.25. RXCJ1314.4-2515

6.25.1. Literature Review

RXCJ1314 is a double relic cluster. [Valtchanov et al. \(2002\)](#) obtained 37 spectroscopic redshifts of cluster members and found that there is a significant bimodal distribution in redshift space (~ 1700 km/s separation) and is supported by a bimodal distribution of galaxies in projected space. The double relics have been observed on VLA and GMRT ([Feretti et al. 2005; Venturi et al. 2007, 2013](#)), although little work has been done studying the spectral steepening or polarization. [Mazzotta et al. \(2011\)](#) briefly reported on their analysis of XMM-Newton data (106 ks), and found a shock front consistent with the leading edge of the western radio relic. They note that there is excellent agreement between the Mach number estimates of X-ray and radio. Interestingly this shock front is M-shaped which they suggest may indicate infalling material. Most recently, [George et al. \(2017\)](#) observed the cluster with the Murchison Widefield Array at low frequencies between 88 MHz and 215 MHz. The east relic is clear in each band except the lowest frequency (88 MHz), but the west relic and halo are blended for all frequencies. The east and west relics are found to have spectral indices between 118 MHz and 1.4 GHz of -1.03 ± 0.12 and -1.22 ± 0.09 , respectively.

6.25.2. Results

We observed RXCJ1314 with two Keck DEIMOS slit-masks and with Subaru SuprimeCam in g and r broadband filters as well as NB814 for H α study. Here we only analyze the broadband imaging. The spectroscopic survey resulted in 156 cluster members, which are well fit by a single Gaussian with redshift 0.24703 ± 0.00035 and velocity dispersion 1094 ± 64 km s $^{-1}$. The red sequence luminosity distribution has three peaks. Two are aligned east to west between the double radio relics, and the third is to the south. Unfortunately we do not have spectroscopic coverage for the south subcluster, but inspection

of the X-ray surface brightness distribution suggests that the subcluster has yet to merge since the ICM is well aligned with the galactic light. Interestingly, there is a stream of gas suggesting the subcluster may have had a glancing interaction or that it is embedded within a gas filament that is being accreted by the main cluster to the north.

We place subcluster priors on the east and west subclusters and allow for a conservative velocity prior. The GMM is run for one and two halo models. The two halo model is preferred according to the BIC score. The two subclusters have ~ 1500 km s $^{-1}$ line of sight velocity differences, which is the largest among the double relic systems in our sample. The velocity dispersions of the two subclusters are similar suggesting a 1:1 mass ratio merger.

The large line of sight velocity difference suggests a merger axis with a substantial component along the line of sight. The radio contours for this cluster (see Figures 9, 12, and 16) are based on our VLA polarization observations. For details on the preparation of these contours see [Golovich et al. \(2017\); Benson et al. \(2017\)](#), where we present analogous observations for ZwCl0008 and ZwCl2341. These radio observations will provide an upper limit on the viewing angle of the merger axis based upon the semi-analytic work of [Ensslin et al. \(1998\)](#), which may help contain the dynamics of this cluster. The dynamics of RXCJ1314 will be studied in a forthcoming paper.

6.26. ZwCl 0008.8+5215

6.26.1. Literature Review

[van Weeren et al. \(2011c\)](#) first identified ZwCl 0008 as a double radio relic system while searching the 1.4 GHz NVSS, 325 MHz WENSS, and 74 MHz VLSS surveys. They carried out a radio survey of ZwCl 0008 with GMRT observations at 241 MHz and 640 MHz and WSRT observations at 1.3–1.7 GHz in full polarization mode. Two radio relics were identified, with the eastern relic larger than the western relic. Spectral index maps show a steepening trend toward the cluster center for both relics indicating motion away from the center. The spectral indices at the front of the relics were reported to be -1.2 ± 0.20 and -1.0 ± 0.15 for the east and west relics respectively. Taking these as the injection spectral indices, Mach numbers (\mathcal{M}) of $2.2_{-0.1}^{+0.2}$ and $2.4_{-0.2}^{+0.4}$ were reported for the east and west relics. In addition, the polarization was measured at 5 – 25% for the east relic and 5 – 10% for the west relic.

ZwCl 0008 was studied in a follow up simulation analysis by [Kang et al. \(2012\)](#), whose diffusive shock acceleration simulations showed that $\mathcal{M} = 2$ explains the relics in ZwCl 0008 regardless of the level of pre-existing relativistic electrons. They also find a projection angle between 25 and 30° to model the spectral index and radio flux.

[Kierdorf et al. \(2016\)](#) studied the eastern relic at 4.85 and 8.35 GHz with the Effelsberg 100-m telescope. The relic is detected at both frequencies, but only the southern portion in the high frequency band. Polarized emission is detected at 4.85 GHz; whereas, [van Weeren et al. \(2011c\)](#) detected only patchy polarized emission at 1.4 GHz. A maximum polarization fraction of $26 \pm 7\%$ and $22 \pm 4\%$ is estimated for the 8.35 and 4.85 GHz images, re-

spectively, which is in agreement with the value estimated by [van Weeren et al. \(2011c\)](#).

Most recently, [Golovich et al. \(2017\)](#) present a wide range of observations including HST ACS+WFC, Subaru SuprimeCam, Keck DEIMOS, Chandra, and JVLA imaging. The HST and Subaru imaging are used to complete a weak lensing analysis, which finds a $\sim 4:1$ mass ratio between two mass peaks. The lower mass peak is associated with a cool-core remnant analogous to the “bullet” in the Bullet Cluster. The JVLA observations were used to estimate the polarization of the radio relics, which were measured to be as high as 40%. The spectroscopy and photometry indicate a bimodal merger as well. Interestingly, there are large offsets between the BCGs and lensing peaks; although, the uncertainties in the lensing centroids are large due to the low mass and redshift of this system. Finally, a dynamics analysis shows the cluster to be near apocenter having passed pericenter with a relative velocity of $\sim 2000 \text{ km s}^{-1}$ $\sim 1 \text{ Gyr}$ before the observed state.

6.26.2. Results

Here we re-evaluate the galaxy substructure with our MCMC-GMM. In [Golovich et al. \(2017\)](#) we utilized a simpler GMM without MCMC functionality. Our shrinking aperture method results in 116 spectroscopic cluster members, and the red sequence luminosity distribution based on our Subaru SuprimeCam g and r observations is bimodal along an east to west axis. The cluster redshift distribution is well fit by a single Gaussian with redshift 0.10383 ± 0.00027 and velocity dispersion $791 \sim 56 \text{ km s}^{-1}$ in agreement with [Golovich et al. \(2017\)](#).

We place subcluster priors on the two BCGs with conservative redshift ranges. The two halo model is preferred over the single halo model although only slightly. Based on the preponderance of evidence for a bimodal merger, we only study the two halo model. The main difference between this subcluster model and the results of [Golovich et al. \(2017\)](#) is the mass ratio based on the velocities. Subcluster 1 (east) is more massive according to the lensing analysis; however, the velocity dispersion of subcluster 2 was larger in [Golovich et al. \(2017\)](#). Here, while still similar, the velocity dispersions suggest subcluster 1 is more massive, in agreement with the lensing results; although, with more similar masses than the 4:1 mass ratio suggested by the lensing analysis. Finally, the results here are in agreement with a low line of sight velocity difference between the two subclusters.

6.27. ZwCl 1447+2619

6.27.1. Literature Review

ZwCL1447 is a single relic and halo system that is part of the [Dressler et al. \(1999\)](#) sample of 10 Distant Rich Clusters of Galaxies. [Giovannini et al. \(2009\)](#) found a radio relic candidate in the north, however when [Govoni et al. \(2012\)](#) investigated the system with more radio observations they found that this northern relic candidate was actually a radio halo; additionally, they detected a southern radio relic. Both the radio halo and southern radio relic have considerable point source contamination. [Giovannini et al. \(2009\)](#) find that both the ROSAT X-ray measured gas distribution and the SDSS measured cluster galaxy distribution are elongated along the axis

connecting the radio halo and relic, typical with post merger systems.

6.27.2. Results

We observed ZwCl1447 with two slitmasks of Keck DEIMOS and in g, r, and i bands with Subaru Suprime-Cam. The spectroscopic survey results in 116 cluster members well fit with a single Gaussian of redshift 0.37574 ± 0.00057 and velocity dispersion $1382 \pm 90 \text{ km s}^{-1}$. The red sequence luminosity distribution has three peaks; however, a bright star in the south has affected the contours. This star will need to be modeled out in more detailed analyses, but this is beyond the scope of this study.

Two of the red sequence luminosity peaks are aligned with the radio relic, and the third is situated to the south, just east of the relic. The radio halo is slightly offset from the main subcluster to the north suggesting the ICM could be displaced away from the center of the cluster. ZwCl 1447 is the only cluster in our sample without Chandra or XMM-Newton data. We present the X-ray map from RASS in Figure 16, which shows structure along the supposed merger axis, but is too low resolution to comment further.

We placed subcluster priors on the two luminosity peaks aligned with the radio relic. We left out the third southernmost peak due to our lack of spectroscopic coverage in this region. We run one and two halo models with the GMM, and the one halo model is preferred with a lower BIC. This is likely due to our sparse spectroscopic sampling in the south due to the bright star. We used SDSS imaging for target selection, and the photometric catalog is incomplete in this region. There are many galaxies within the stellar halo that are unrecovered from SDSS.

We note that the cluster velocity dispersion is high suggesting a massive system; however, stellar subtraction, X-ray observations, and more spectroscopic observations in the south are necessary to fully analyze this system.

6.28. ZwCl 1856+6616

6.28.1. Literature Review

ZwCl1856 (also known as PSZ1 G096.89+24.17) is a double relic system identified as such through a search of Planck SZ selected clusters ([Planck Collaboration et al. 2014](#)) in NVSS, WENSS, VLSS surveys carried out by [de Gasperin et al. \(2014\)](#). The Planck Collaboration estimates the mass to be $M_{500} = 4.4^{+0.45}_{-0.48} \times 10^{14} \text{ M}_\odot$ ([Planck Collaboration et al. 2016](#)). The RASS emission corresponds to a X-ray luminosity of $L_X = 3.7 \times 10^{44} \text{ erg s}^{-1}$. Using (L, T) scaling relations from [Pratt et al. \(2009\)](#), this corresponds to $T_X \sim 4 \text{ keV}$ ([de Gasperin et al. 2014](#)).

[de Gasperin et al. \(2014\)](#) carried out WSRT 21 cm observations sufficient to study the polarization of the relics. The two relics are symmetrically located along a north-south axis separated by $\sim 2 \text{ Mpc}$. The polarization is found to be $\sim 10\%$ for each relic. Finally, a radio halo is marginally detected. [de Gasperin et al. \(2014\)](#) suggests lower frequency observations could confirm or refute the presence of a halo.

6.28.2. Results

We observed ZwCl1856 with two slitmasks on Keck DEIMOS and with Subaru SuprimeCam in g and r bands. The spectroscopic survey utilized DSS imaging for targeting, and as a result of the poor seeing the majority of detected objects were stars. The survey resulted in 48 cluster member redshifts that are well fit by a single Gaussian of redshift 0.30362 ± 0.00061 and velocity dispersion $990 \pm 106 \text{ km s}^{-1}$. As with PSZ1G108, the SuprimeCam imaging is mostly unusable due to tracking issues. Two of the six exposures in g band and all exposures in r band were lost to this issue. In order to define the color of detected objects, we observed PSZ1G108 with Gemini-N GMOS in g and r bands. We utilized a 2×1 mosaic covering the north and south portions of the cluster field including the two radio relics. Each pointing is composed of 5×110 s exposures. The data were reduced with the standard Gemini IRAF package, and the images were coadded with the same methodology as our SuprimeCam imaging.

The red sequence luminosity distribution is bimodal along a north to south axis symmetrically placed between the two radio relics. We placed subcluster priors on the two luminosity peaks and allowed for a conservative redshift range for our GMM. The two models are nearly equal according to the BIC score with the two halo model slightly preferred. We study only the two halo model due to the clear evidence of a major merger from the double radio relics and the X-ray surface brightness distribution, which is elongated along the same axis (see Figure 16). The two resulting subclusters have similar redshifts and velocity dispersions indicating a 1:1 mass ratio merger in the plane of the sky. In summary, ZwCl1856 appears to be among the cleanest bimodal systems in our sample; however, further observations will be necessary to study this system.

6.29. ZwCl 2341+0000

6.29.1. Literature Review

[Bagchi et al. \(2002\)](#) were the first to discover the diffuse radio emission associated with the radio relics in the 1.4 GHz NVSS survey, and concluded that the emission was the first evidence of cosmic-ray particle acceleration taking place at cosmic shocks. They also noted that ZwCl2341 is likely in the process of ongoing structure formation, so in many ways they were the first to directly observe and realize the association between radio relics and merging clusters. [van Weeren et al. \(2009b\)](#) followed-up the system with GMRT 157, 241, and 610 MHz observations, confirming this interpretation. They were able to measure radio spectral indices of -0.49 ± 0.18 and -0.76 ± 0.17 for the northern and southern relics, respectively. In their analysis they also presented Chandra X-ray observations and found that the ICM of the system is highly disturbed and elongated along the axis of the two relics. [Giovannini et al. \(2010\)](#) obtained follow-up 1.4 GHz VLA imaging of the system and confirmed the existence of the relics. Interestingly they also found evidence for polarized (11%) diffuse emission along optical filament of galaxies between the two relics, which they posit may be a giant and highly elongated radio halo or the merging of two clusters both hosting a central radio halo. [Akamatsu & Kawahara \(2013\)](#) observed the system with Suzaku in hopes of detecting temper-

ature or density jumps associated with the radio relic locations. While they observe a decrease in both, the angular resolution of Suzaku was not sufficient to check for the presence of a sharp discontinuity. [Ogrean et al. \(2014\)](#) did not detect a shock in the location of the radio relic in XMM-Newton and Chandra observations.

[Boschin et al. \(2013\)](#) conducted a spectroscopic survey of the survey of the system, obtaining 142 redshifts, 101 of which were cluster members. Analysis of the velocity distribution of cluster members yielded two distinct groups, and the possibility of a third. Spatial distribution of the galaxies shows an elongated shape to the cluster in the SSE-NNW direction with four over densities (three very significant), matching the elongated X-ray gas distribution. Their color-magnitude selection of cluster members showed a more complex structure, yielding eight galaxy density peaks.

[Benson et al. \(2017\)](#) present our Subaru SuprimeCam and Keck DEIMOS observations (see §3.2). [Benson et al. \(2017\)](#) find a three subcluster model best describes the data using a similar MCMC-GMM subclustering analysis to the one used in this paper. [Benson et al. \(2017\)](#) interpret the three subclusters to be involved in two mergers with the plane of the sky merger forming the two radio relics with a secondary line of sight merger within the north between two low mass subclusters. Using our Subaru imaging, [Benson et al. \(2017\)](#) complete the first weak lensing analysis finding a total mass of $4.49 \pm 1.72 \times 10^{14} \text{ M}_\odot$, which is substantially lower than previous estimates based on the velocity dispersion of subclusters ([Boschin et al. 2013](#)).

6.29.2. Results

Here we use our analysis scheme to study the same data presented in [Benson et al. \(2017\)](#). Namely, ZwCl2341 was observed with three slitmasks on Keck DEIMOS resulting in 224 cluster members within R_{200} . The redshift distribution is well fit with a single Gaussian with redshift 0.26960 ± 0.00029 and velocity dispersion $1036 \pm 49 \text{ km s}^{-1}$. The red sequence was mapped with g and r band images from Subaru SuprimeCam. The distribution has three distinct peaks aligned between the radio relics from northwest to southeast. There is an additional extension of red sequence luminosity toward the east of the northern peak.

[Benson et al. \(2017\)](#) elected to fit no more than three halos with the GMM. The preferred model was a three halo model associated with the northern and southern luminosity peaks with two in the north splitting in velocity space. Here we place the same three halos but with an additional halo associated with the middle luminosity peak, which was less distinct in the [Benson et al. \(2017\)](#) luminosity map.

We run 12 models ranging from one to four halos. The preferred model is analogous to [Benson et al. \(2017\)](#) with a slightly lower velocity dispersion for the southernmost subcluster (subcluster 3 in Figures 12 and 14). Subclusters 2 and 3 are well aligned with the radio relics and at similar redshifts suggesting a merger in the plane of the sky. The southern subcluster appears much more massive based on the velocity dispersion. Subcluster 1 has a higher redshift and may be involved in a secondary merger with subcluster 2.

Inspection of the X-ray surface brightness map shows

general elongation between the radio relics but also a clumpy morphology in the northeast indicating dynamical activity. Further X-ray observations and deeper imaging for more precise lensing will be necessary to fully understand this complex cluster.

7. RESULTS: SAMPLE

In the previous section, we discussed the results of the photometric and spectroscopic survey for 29 merging clusters. We used these results in conjunction with radio relic and X-ray surface brightness morphology to infer the most likely merger scenario that launched the shocks associated with the radio relics in each system. In this section, we compile results and study the ensemble characteristics of radio selection with respect to the velocity and geometry information.

7.1. Line of Sight Motion

Our spectroscopic survey and GMM analysis on each system allows for direct measure of the line of sight velocity difference between merging subclusters. Simply put, a large line of sight velocity difference between subclusters indicates a merger axis along the line of sight and/or near pericenter while a small line of sight velocity difference indicates a merger occurring within the plane of the sky and/or near apocenter.

To estimate the velocity difference, we draw random subcluster members (with replacement) from the subcluster histograms (see Figure 13 and 14) and calculate the line of sight velocity difference for each bootstrap. For the i th bootstrap from each subcluster,

$$v_{i_{1,2}} = \frac{(1+z_{i_{1,2}})^2 - 1}{(1+z_{i_{1,2}})^2 + 1} c, \quad (7)$$

where c is the speed of light. The line of sight velocity difference is then,

$$\Delta v_{\text{LOS}} = \frac{|v_{i_1} - v_{i_2}|}{1 - \frac{v_{i_1} v_{i_2}}{c^2}}. \quad (8)$$

We take the median of this distribution after 10,000 samples as the subcluster line of sight velocity difference and the 95% confidence interval for the remaining analysis.

For single halo clusters with clear luminosity bimodality aligned with the radio relic (A1300, A2061, ZwCl1447), we define the line of sight velocity difference by the BCG redshifts and assume a 200 km s^{-1} uncertainty, which is in line with spectroscopic studies of BCG peculiar velocities (e.g. Oegerle & Hill 2001). For three and four subcluster systems, we look for a preferred merger axis in the X-ray surface brightness map, the red sequence luminosity distribution, GMM substructure, and the radio relic(s). In A2744, no pair of subclusters aligned with the radio relic; however, subcluster one, in the north, has an east to west elongated red sequence luminosity distribution, which has a bright galaxy at either end. We use these two galaxies to define the line of sight velocity difference and assume 200 km s^{-1} uncertainty.

Note that we eliminated several systems from this analysis: A746 due to the extreme stellar contamination, which makes it impossible to map the red sequence luminosity distribution; A2255 due to the ambiguous merger

axis across all wavelengths; A2345 due to the complex merger where two separate mergers may have generated separate radio relics (Boschin et al. 2010); finally, PSZ1G108 due to insufficient optical imaging quality to map the red sequence luminosity distribution. This leaves 25 systems with estimates of the line of sight velocity difference between merging subclusters.

We then calculated the expected free-fall velocity from infinity (v_{max}) of two truncated NFW (Navarro et al. 1996) halos with mass determined using the $M_{200} - \sigma_v$ scaling relations of Evrard et al. (2008) assuming the mass-concentration relation of Duffy et al. (2008). Following Dawson (2013), we calculate the maximum free-fall velocity using conservation of energy and the potential energy, V , of overlapping truncated (at R_{200}) NFW profiles,

$$v_{\text{max}} = \sqrt{-\frac{2}{\mu} V(r=0)}. \quad (9)$$

We plot the ratio $\Delta v_{\text{LOS}}/v_{\text{max}}$ for each system in Figure 17. The 95% confidence intervals are color-coded according to the number of subclusters identified by our GMM analysis (green, orange, purple, and pink for one, two, three, and four subclusters, respectively). With the exception of a few outliers merging pairs of subclusters have low line of sight velocity differences compared with the free-fall velocity. In particular, with the exception of RXCJ1314, bimodal systems have line of sight velocity differences that are generally consistent with zero at $1-3\sigma$.

For comparison, we plotted the global velocity dispersion of each cluster as a point along the same axis, scaled to the free-fall velocity. This helps explain why the GMM was able to identify substructure in some systems and not in others. First, for the three one-halo systems at the top of Figure 17 (A1300, A2061, and ZwCl1447), the red sequence luminosity distribution clearly shows multiple peaks (see white contours in Figure 9), but the projected separation in these systems is small. Also, the spectroscopic completeness in the inner regions of these systems is insufficient to overcome the BIC penalty for the extra parameters necessary for bimodal models of these systems. The large line of sight velocity difference between the respective BCGs suggests that these mergers have a substantial fraction of their merger axis situated along the line of sight, which should help the GMM identify overlapping substructures; however, the velocity difference is not larger than the velocity dispersion of the cluster velocity distribution. In the case of RXCJ1314, which has a similar orientation to the three one-halo clusters at hand, the velocity difference is larger than the velocity dispersion, so the BIC penalty for extra model parameters does not outweigh the likelihood of having subclusters with a large line of sight velocity difference. The purple and pink points at the bottom of Figure 17 represent more complex systems. Relics may preferentially select for mergers occurring in the plane of the sky (as suggested by the results for the bimodal systems); however, this simple geometry could be washed out by more complex three and four body orbits by the time of our observations several hundred Myr after pericenter. Despite this, we find small line of sight velocity differences between the selected merging pairs in five of the eight most complex systems in our ensemble. However,

the interpretation of these merger scenarios is difficult without detailed simulations.

The results presented in Figure 17 also explain why the global velocity histograms are nearly universally well fit by a single Gaussian (see Figures 4 and 5). The line of sight velocity difference between radio selected merging subclusters is generally smaller than the velocity dispersion of the global cluster velocity distribution.

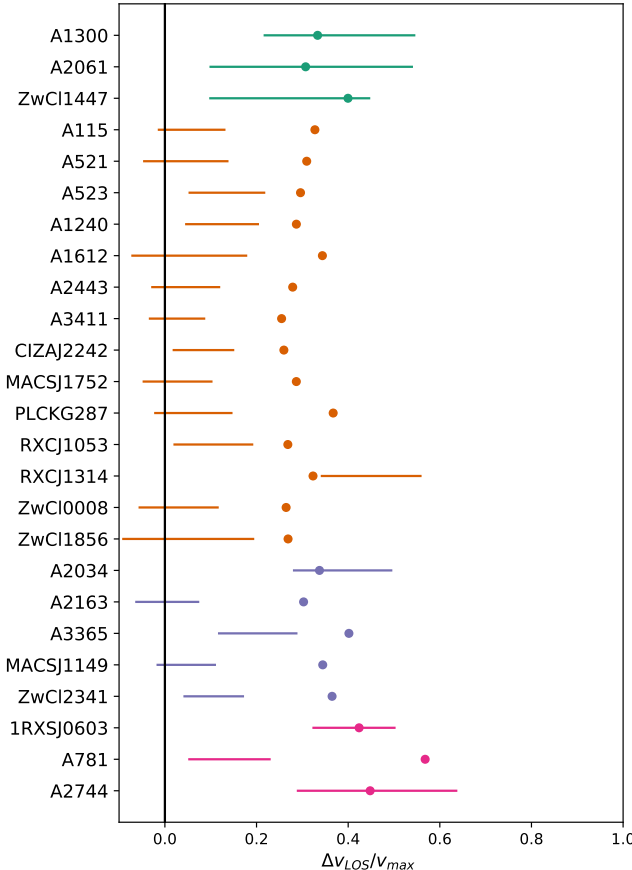


Figure 17. Line of sight velocity differences between merging subclusters associated with radio relics. The clusters are organized by the number of subclusters in the lowest BIC model (see Table 7). Green, orange, purple, and pink refer to systems comprised of one, two, three, and four GMM subclusters, respectively. The bars represent the 95% confidence interval for the ratio of line of sight velocity difference to maximum three dimensional infall velocity. The colored points are the ratio of the global velocity dispersion to the maximum free-fall velocity, for comparison.

7.2. Merger Geometry

In 28 of 29 systems in our sample (all except A2255), there is evidence of merger activity aligned with the radio relic. For the majority of these, our GMM has identified two substructures within the spectroscopy that are apparently the merging subclusters. In clusters with insufficient spectroscopic coverage to prefer multimodality, the red sequence luminosity distribution generally is elongated along the axis that connects with the radio relic (e.g. A1300, A2061, A2345, A2744, PSZ1G108, and ZwCl1447). In this subsection, we compare the axis connecting the two BCGs of apparent merging substructures with the axis connecting the center of mass to the center

of the radio relic. The basic geometry under examination is presented in Figure 18.

For clusters without GMM identification of substructure, we connect the brightest galaxies at the ends of the extension of the red sequence luminosity distribution. We withhold A2443 from this analysis because it is a known radio phoenix. This type of radio relic was shown to bias similar analyses (van Weeren et al. 2009a; de Gasperin et al. 2014). We withhold A746 due to the inability to identify substructure due to the bright star in the northwest. We also withhold PSZ1G108 due to the lack of good quality optical imaging for galaxy identification. Finally, we withhold A2255 and A2345 due to the complexity of the mergers and inability to define the merger geometries.

In Figure 19 we present the distribution of defined geometrical quantities for the 35 relics across 24 merging clusters. Radio relics are generally very well aligned with the BCG separation axis. Furthermore, with the exception of PLCKG287, radio relic systems have a narrow range of projected BCG separations (d_{proj}) and relic distances (from the center of mass). Without PLCKG287, the BCG separation and relic distance distributions tighten to 877 ± 288 kpc and 1070 ± 349 kpc.

In the middle panel of Figure 19, a weak trend between BCG projected separation and relic distance is apparent. This is expected for the outbound phase of the merger; however, post-apocenter, the BCGs return to smaller projected separations whilst the radio relics continue to propagate outwards. Detailed analysis is required to determine if a given system is in the outbound or returning phase (see e.g. Ng et al. 2015). This analysis is beyond the scope of this paper. The shock propagation speed is proportional to the mass of the opposite subcluster (Springel & Farrar 2007). The canonical example is that of the Bullet Cluster, where the lower mass “bullet” has merged from east to west at a high velocity, and the shock front is just ahead of it. The shock on the reverse side of the cluster is much closer to the center of mass. A good analogy is a piston punching through the ICM of the main halo driving the shock ahead, while the more massive cluster is moving slower with respect to the center of mass and thus doesn’t propel its shock as fast. To check for this, we compare the projected distance to the relic and the BCG in the center of mass frame for all 35 relics in Figure 20. If all subclusters are still outbound, we expect a correlation where BCGs further from the center of mass will be on the side of relics that have propagated further. We use the Spearman rank-ordered correlation test to check for correlation between the relic and BCG distances to the center of mass. We find a correlation in both the full relic sample and the double relic sample ($p = 0.012$ and $p = 0.0046$, respectively). Here, the p-value gives the chance that two uncorrelated datasets would give as strong a correlation.

7.3. Global Cluster Relations

In this subsection, we compile global cluster measures of temperature, X-ray luminosity, and cluster mass (as estimated by the Planck Collaboration) from the literature. We compare each of these measures against each other as well as the global velocity dispersion estimated from our spectroscopic survey. Each of these measures is known to be biased during a merger, but by compar-

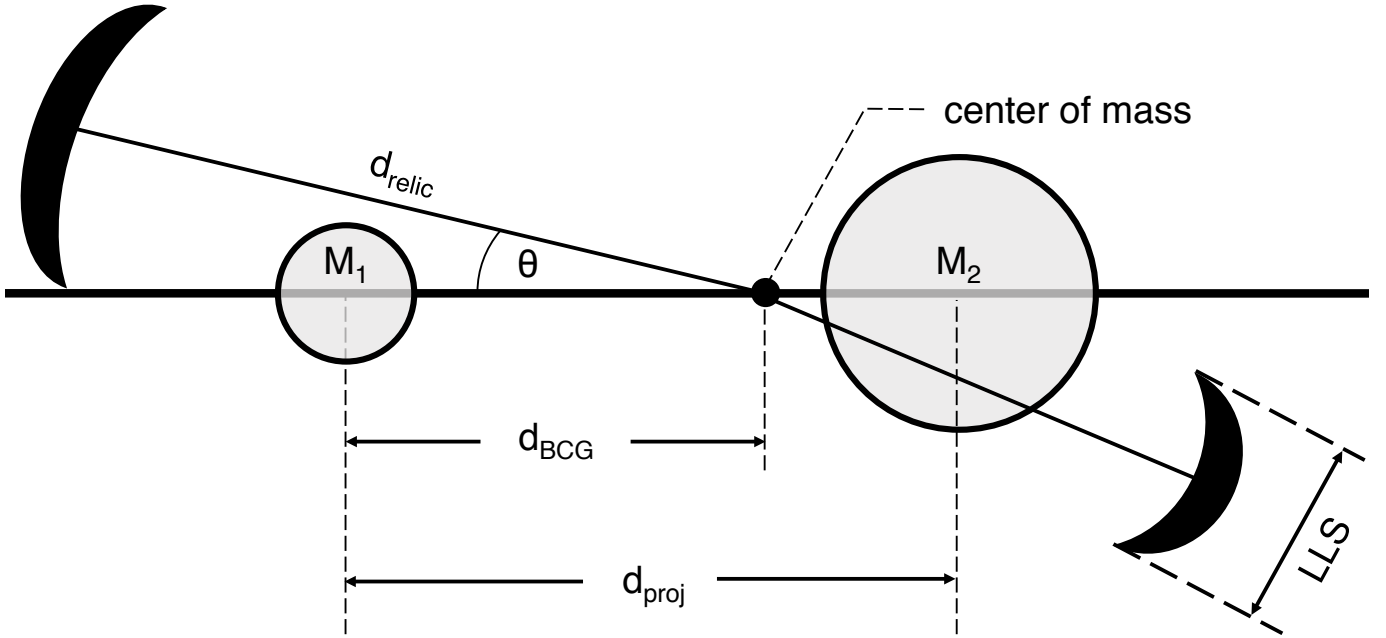


Figure 18. Schematic representation of the relic geometry for a double relic system (e.g. A1240). Each relic is located with a position angle and distance from the center of mass of the system determined from the velocity dispersions of subclusters aligned with the radio relics. Single relic systems follow the same conventions.

ing them, we may get a sense of how they are biased with respect to one another. The X-ray luminosities are quoted in the ROSAT 0.1-2.4 keV band. The Planck mass is taken from the PSZ1 catalog (Planck Collaboration et al. 2016). A few clusters are missing from this catalog. For these, the mass is estimated using the X-ray luminosity and the scaling relations of Pratt et al. (2009) following de Gasperin et al. (2014).

In Figure 21, we present the relationship between each of these global measures. There is a clear positive relationship between each. Interestingly, the temperature, X-ray luminosity, and Planck mass are related much more tightly with each other than the velocity dispersion. This is explained by the fact that each of these measures is based on the ICM; whereas, the velocity dispersion is traced by the galaxies, which more closely follow the DM distribution. Despite the scatter, there is still clear evidence of a positive correlation between each of these measures, which speaks to the usefulness of quoting these parameters despite the merger induced biases.

8. DISCUSSION

We have presented an optical and spectroscopic survey of 29 merging galaxy clusters featuring ~ 40 hours of optical imaging and ~ 5500 spectra of member galaxies. We have coupled these extensive optical observations with ~ 4000 ks of X-ray integration time and ~ 250 hr of radio integration time. This comprehensive set of data has allowed us to characterize the redshift, velocity dispersion, minimum number of subclusters, and most likely merger scenario for each system. In 21 of 29 systems, we link the radio relic(s) to galaxy substructure identified by our GMM subclustering analysis on the spectroscopic cluster populations. In six additional systems, the spectroscopic survey is insufficient to detect substructure that

is aligned with the radio relic(s), but there is clear substructure in the two dimensional red sequence luminosity distribution and additional evidence of a merger in the X-ray surface brightness map. In the two remaining systems either an extremely bright star (A746) or complex merger scenario (A2255) hinder our ability to decipher the merger that induced the respective radio relics.

On an individual system basis, we have compiled findings from the literature pertaining to X-ray, radio, galaxy, and lensing analyses of each system. We have contextualized the diverse literature with our galaxy analysis, characterized each system based on our substructure analysis, and identified the most likely merger scenario.

Our chief ensemble finding from the spectroscopic survey and subcluster analysis is the strong evidence for transverseness. The line of sight velocity difference between merging subclusters is generally low with a majority consistent with zero line of sight velocity difference at 3σ . Secondly, radio relics are a robust indicator of the merger axis. The relics are generally positioned within 20° of the axis connecting the BCGs of merging subclusters. Furthermore, double radio relics are a strong indicator of simple geometries. Clusters with double radio relics have an average of 2.4 identified red sequence luminosity peaks; whereas, single relic clusters have an average of 3.1 galaxy luminosity peaks.

In the following subsections, we discuss general considerations that highlight specific aspects of our analysis, results, and future directions for merging cluster studies.

8.1. Gold sample

Merging clusters offer a unique setting to study DM, the ICM, and galaxy formation during the most extreme periods of structure formation. These events occur over

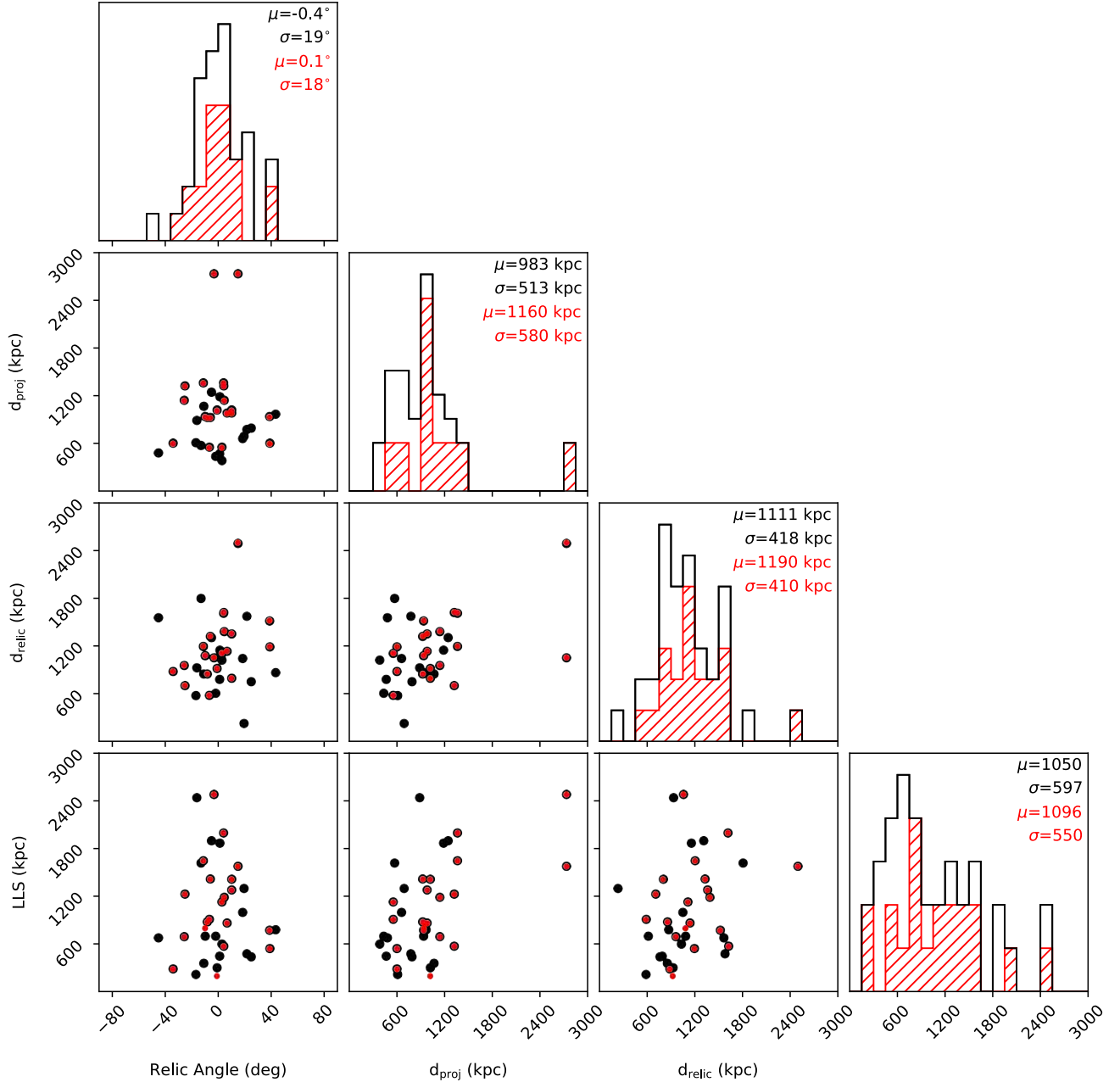


Figure 19. Radio relic geometry for 35 radio relics in 24 merging galaxy clusters. Relics tend to be well aligned with the axis connecting BCGs of merging subclusters. Negative angles imply clockwise angles from the BCG axis toward the relic position vector. The black distribution is for all relics, and the red distribution is for double relic clusters. See Figure 18 for a schematic representation of the defined geometry.

the course of several billion years, and radio relic selection has allowed us to identify systems in the period between the first and second collision of major mergers. In order to study the physics within the main components of these systems, we must be able to place meaningful constraints of the age and dynamics to control for time varying processes. The only systems that we can accurately describe in this context are simple, bimodal systems. Here we reduce our ensemble of 29 systems to a *gold sample* of eight systems that we propose be studied

in greater detail individually and together in precise ensemble analyses. Several of these systems have been featured in these types of studies by the Merging Cluster Collaboration to date. The primary feature of these systems is their simple geometry, often highlighted by double relics. Secondary considerations include high mass, redshift, small line of sight velocity difference, and large projected separation.

The Merging Cluster Collaboration *gold sample*:

- A1240

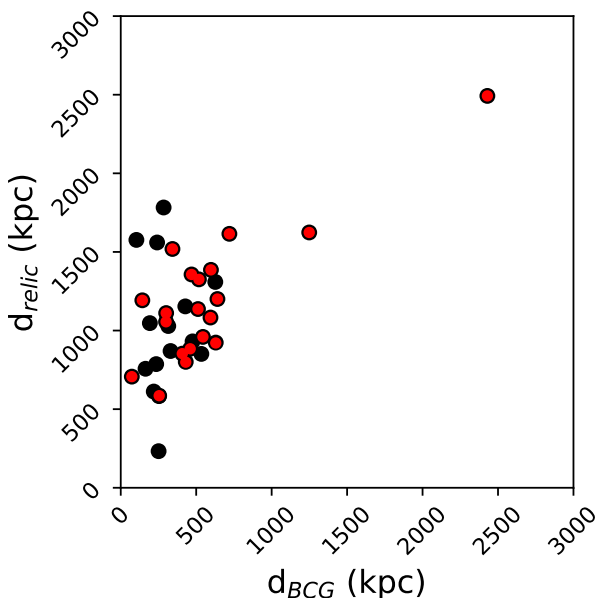


Figure 20. Projected distances from the center of mass to radio relics versus project distance from the center of mass to the opposite subcluster BCG for 35 radio relics from 24 merging clusters (black) and 22 radio relics from 11 double radio relic systems (red). We find a correlation between these two parameters as expected for a model of relic propagation in the center of mass frame (see e.g. Springel & Farrar 2007).

- A3411
- CIZAJ2242
- MACSJ1149
- MACSJ1752
- RXCJ1314
- ZwCl0008
- ZwCl1856

8.2. Galaxy Clusters as SIDM Probes

Since the Bullet Cluster was used to demonstrate the existence of an approximately non-collisional form of matter (Clowe et al. 2006) and then further to set an upper limit on the self-interaction cross section ($\sigma_{\text{DM}} < 0.7 \text{ cm}^2 \text{g}^{-1}$: Randall et al. 2008), astronomers have sought observations of merging clusters for stronger DM constraints. Using order of magnitude arguments, Bradac et al. (2008); Merten et al. (2011) found looser constraints than the Bullet Cluster offered with observations of MACSJ0025 and A2744, respectively. Astrophysical evidence for SIDM is generally found in galactic scales in the form of cored halos, diverse rotation velocities, missing satellites, and discrepant stellar dispersions in the most massive Milky Way satellites from CDM predictions. In principle, each of these issues are solvable with SIDM; however, debate in the literature is ongoing, with skeptics suggesting baryonic processes not included in simulations could explain the discrepancy with observations (see Tulin & Yu 2017, for an extensive review on this topic).

These small scale discrepancies with Λ CDM typically require $\sigma_{\text{DM}} \sim 1 - 3 \text{ cm}^2 \text{g}^{-1}$ to be explained by SIDM. At cosmic (Rocha et al. 2012) and cluster scales (Peter et al. 2012), cross sections at this level were shown to preserve large scale structure formation while causing more spherical halos with large (~ 100 kpc) cores. However, Newman et al. (2012a,b) found cores in relaxed clusters to be much smaller (~ 10 kpc). Kim et al. (2017) showed that merging clusters retain a signal for long after the merger in the form of wobbling BCGs, and Harvey et al. (2017) studied archival HST images and compared to simulations to estimate the average wobbling amplitude for 10 clusters to be ~ 13 kpc. Clusters should have much larger cores and BCG wobbling amplitudes if $\sigma_{\text{DM}} \sim 1 \text{ cm}^2 \text{g}^{-1}$.

In merging clusters, SIDM causes momentum transfer between the DM halos such that density distribution falls behind the galaxies (Kahlhoefer et al. 2014; Kim et al. 2017). Using this type of model, Harvey et al. (2015) studied an ensemble of merging clusters and further constrained the upper limit to $\sigma_{\text{DM}} < 0.47 \text{ cm}^2 \text{g}^{-1}$; however, Wittman et al. (2017) showed that specific analysis choices and more complete data from the literature significantly relaxed this constraint to $\sim 2 \text{ cm}^2 \text{g}^{-1}$. In this paper, we argued that constraining the phase of the merger is important for selecting proper systems to test SIDM hypotheses.

Kaplinghat et al. (2016) introduced a dark photon model with Yukawa type self-interactions. This model has a naturally velocity dependent cross section and could explain the apparent discrepant cross section limits inferred across galactic and cluster scales. Merging clusters merge with speeds of \sim a few times the velocity dispersion of relaxed clusters, thus the observable effect in the form of offsets between galaxy and DM peaks would be very small. If SIDM is indeed generated by a Yukawa-type, dark photon model, merging cluster modeling will need to be more precise to be able to push upper limits to these levels.

Offsets between DM and galaxy distributions remain the simplest SIDM observable to constrain in merging clusters; however, Ng et al. (2017) recently studied offsets in the Illustris simulation (Vogelsberger et al. 2014) and found that while the BCG offset is the most robust galaxy offset to measure, the distribution of offsets has a long tail of up to several hundred kpc due to projection effects. This poses a substantial problem for merging clusters as SIDM probes and suggests that any observed offset can never be explained unequivocally as a true SIDM effect. We have specifically compiled our “gold” sample of bimodal merging clusters to include only systems that are of simple geometry merging in the plane of the sky. These systems offer the best chance at probing SIDM hypotheses.

8.3. Future Work

In this subsection, we highlight a few projects that are currently underway to extend the analysis presented here. This is not an exhaustive list, but it offers readers a list of studies to look for in the future.

8.3.1. Merger Dynamics

The techniques developed to understand and quantify the dynamics of merging clusters have progressed

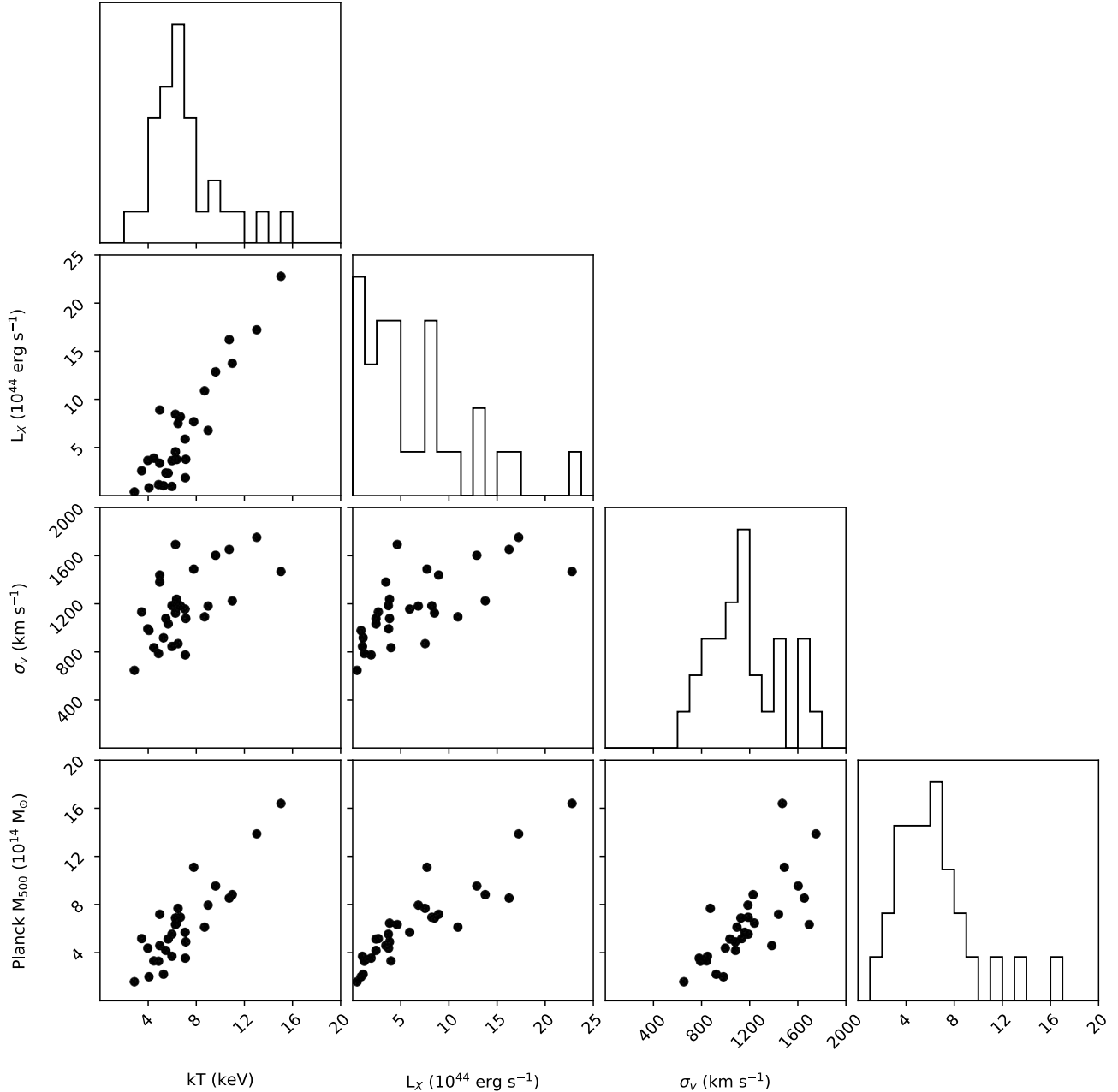


Figure 21. Relationships between four global measures for 29 merging clusters. The clear positive correlation between each suggests that despite the merger induced bias in each, measuring these values gives a first order understanding of the mass of a merging system.

rapidly, especially recently, with the rise of fast computational techniques (e.g. MCMAC: Dawson 2014) as well as powerful, large scale simulations including rich physics. These techniques have greatly enhanced our understanding of these systems. We hope our results here can offer simulators a constrained set of initial conditions with which to simulate these systems. In subsequent dynamical analyses, we will further constrain the dynamics of the eight, gold-sample clusters including timescales since pericenter, the observed phase of the merger, relative velocities, and merger geometry. Furthermore, we will match our observations to analog systems in large

scale N-body simulations (e.g., Dark Sky: Skillman et al. 2014). Our substructure models coupled with velocity information allow us to identify systems in cosmological N-body simulations that can be easily (re)simulated at higher resolution. This allows simulators to maintain realistic formation histories, accretion, and substructure while also satisfying the dynamical constraints of our results here. This technique will offer a substantial step forward in the simulation of these systems and greatly improve astrophysical inference.

8.3.2. BCGs

Recent studies of cosmological simulations (Ng et al. 2017) and simulations of merging clusters with SIDM (Kim et al. 2017) have shown that traditional offset measurements between galaxies and DM distributions may be too noisy to constrain DM. On the other hand, the inner most region of the DM profile may offer alternate signals of SIDM. First, if DM halos have large cores, infalling satellite galaxies may survive without falling completely into the BCG. Similarly, Kim et al. (2017) identified an additional SIDM signal with regard to the BCG position. Harvey et al. (2017) presented an analysis of BCG wobbling in archival HST imaging based on strong gravitational lensing. Several clusters in our sample feature strongly lensed source galaxies in the vicinity of the BCG (see A521 e.g. in Figure 22). These BCGs may offer a specific phase of the BCG wobbling and exhibit larger wobbling amplitudes than those found in relaxed clusters. With this in mind, we have compiled thumbnails of the BCG population in all 29 of our systems. In Figure 23, we present the inner 150×150 kpc centered on the BCG of 1RXSJ0603, which displays both strong lensing features and a multi-cored light profile. The thumbnails for the additional 28 systems in our ensemble are presented in Figure 24. Visual inspection of these thumbnails reveal several multi-modal BCGs and strong lensing features, which speaks to the utility of these alternate potential SIDM signals.

Additionally, BCG alignments have been studied in a range of clusters and have been shown to consistently trace the global cluster profile (e.g. West et al. 2017). The BCGs in actively merging clusters may help elucidate during which epoch of cluster formation this alignment is established. We look to answer this question in a forthcoming paper.

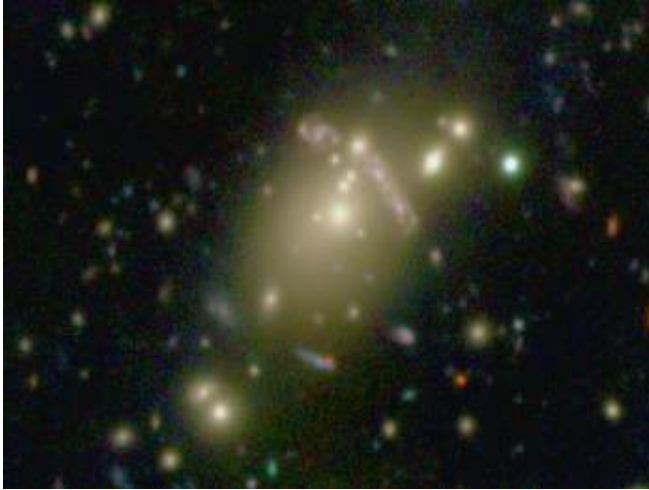


Figure 22. Subaru SuprimeCam VRI color-composite for the BCG of A521. The stellar halo has multiple cores as well as a candidate multiply lensed spiral galaxy. This image was processed using the *trilogy* software (Coe et al. 2012). With spectroscopy of the lensed galaxies, A521 is a good test case for BCG wobbling.

8.3.3. Lensing Studies

In this paper, we presented the red sequence luminosity distribution of each system. In 27 of the 29 clusters, this was based on multi-band Subaru SuprimeCam imaging.

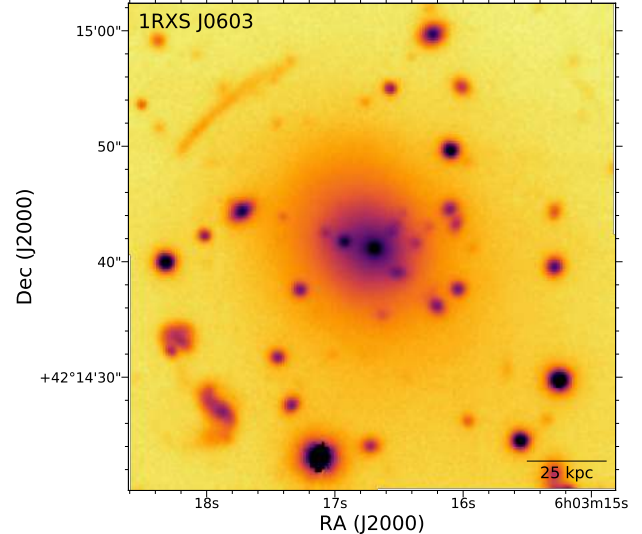


Figure 23. Subaru SuprimeCam r band cutout of the inner 150×150 kpc of the BCG of 1RXSJ0603. A strongly lensed arc is apparent along with several light peaks within the inner region of the overall light profile. This figure, along with the 28 analogous figures presented in Figure 24, will be analyzed in detail in a forthcoming paper.

This imaging is uniformly deep and wide enough for robust weak lensing studies. We have completed a number of such analyses already (Jee et al. 2015, 2016; Golovich et al. 2017; Benson et al. 2017), and we will continue to map the total mass profiles of all systems in the gold sample. We have specifically selected eight clusters in the gold sample to carry out a detailed study of offsets between the galaxy and mass distributions. This analysis will result in a constraint on the DM self-interaction cross section.

9. ACKNOWLEDGMENTS

The authors would like to make special thanks to the generous sharing of a multitude of spectroscopy, radio, and X-ray images. These data have contributed greatly to this project. We would like to thank the broader membership of the Merging Cluster Collaboration for their continual development of the science motivating this work, for useful conversations, and for diligent proofreading, editing, and feedback. NG would like to thank his cohort at UC Davis who have given an ear on many occasions. This material is based upon work supported by the National Science Foundation under Grant No. (1518246). This material is based in part upon work supported by STScI grant HST-GO-13343.001-A. Part of this was work performed under the auspices of the U.S. DOE by LLNL under Contract DE-AC52-07NA27344. Support for this work was provided by the National Aeronautics and Space Administration through Chandra Award Number GO5-14130X issued by the Chandra X-ray Observatory Center, which is operated by the Smithsonian Astrophysical Observatory for and on behalf of the National Aeronautics Space Administration under contract NAS8-03060. RJW is supported by a Clay Fellowship awarded by the Harvard-Smithsonian Center for Astrophysics. Some of the data presented herein were obtained at the W.M. Keck Observatory, which is operated as a scientific partnership among the California Institute of Technology, the University of Cali-

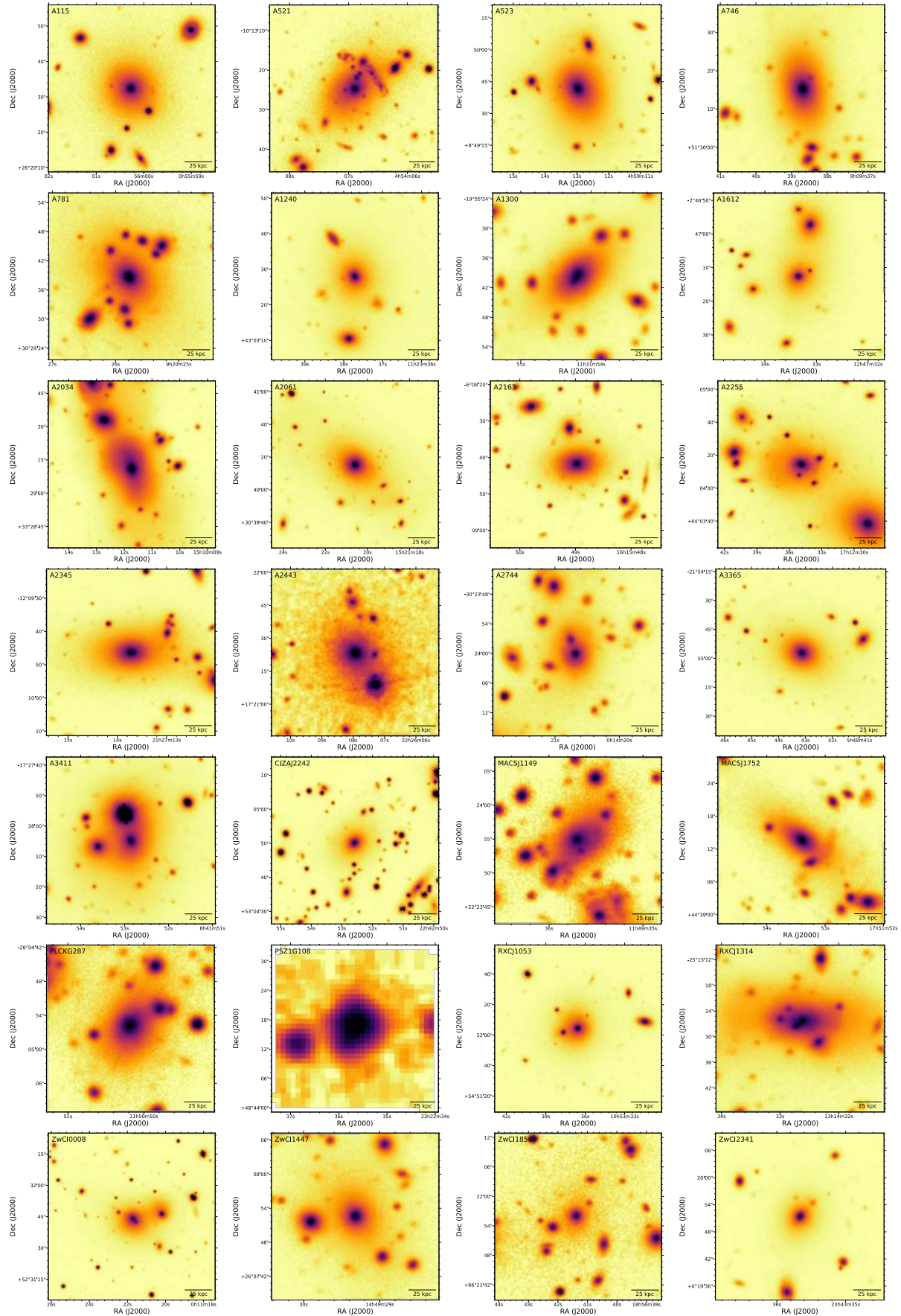


Figure 24. Subaru SuprimeCam cutout of the inner 150×150 kpc of the BCGs for 28 merging clusters. Each frame is the analogous image to Figure 23. Strong lensing features, multi-modal light peaks, and highly elliptical light profiles are evident. These features will be analyzed in detail in a forthcoming paper.

fornia and the National Aeronautics and Space Administration. The Observatory was made possible by the generous financial support of the W.M. Keck Foundation. Funding for the Sloan Digital Sky Survey IV has been provided by the Alfred P. Sloan Foundation, the U.S. Department of Energy Office of Science, and the Participating Institutions. SDSS acknowledges support and resources from the Center for High-Performance Computing at the University of Utah. The SDSS web site is www.sdss.org. The Digitized Sky Surveys were produced at the Space Telescope Science Institute under U.S. Government grant NAG W-2166. Funding for the DEEP2/DEIMOS pipelines has been provided by NSF grant AST-0071048. The DEIMOS spectrograph was funded by grants from CARA (Keck Observatory) and UCO/Lick Observatory, a NSF Facilities and Infrastructure grant (ARI92-14621), the Center for Particle Astrophysics, and by gifts from Sun Microsystems and the Quantum Corporation. This research has made use of the NASA/IPAC Extragalactic Database (NED) which is operated by the Jet Propulsion Laboratory, California Institute of Technology, under contract with the National Aeronautics and Space Administration. This research has made use of NASA's Astrophysics Data System. Based in part on data collected at Subaru Telescope and obtained from the SMOKA, which is operated by the Astronomy Data Center, National Astronomical Observatory of Japan. This research made use of Montage. It is funded by the National Science Foundation under Grant Number ACI-1440620, and was previously funded by the National Aeronautics and Space Administration's Earth Science Technology Office, Computation Technologies Project, under Cooperative Agreement Number NCC5-626 between NASA and the California Institute of Technology. This research made use of APLpy, an open-source plotting package for Python hosted at <http://aplpy.github.com>.

Facilities: Keck (DEIMOS) INT (WFC) Subaru (SuprimeCam) VLT (VIMOS) WSRT GMRT VLA Chandra (ACIS) XMM-Newton (EPIC) ROSAT (PSPC)

REFERENCES

- Abate, A., Wittman, D., Margoniner, V. E., et al. 2009, *ApJ*, 702, 603
 Abdullah, M. H., Ali, G. B., Ismail, H. A., & Rassem, M. A. 2011, *MNRAS*, 416, 2027
 Abell, G. O., Corwin, Jr., H. G., & Olowin, R. P. 1989, *ApJS*, 70, 1
 Adelman-McCarthy, J. K., Agüeros, M. A., Allam, S. S., et al. 2007, *ApJS*, 172, 634
 Aguerri, J. A. L., Sánchez-Janssen, R., & Muñoz-Tuñón, C. 2007, *A&A*, 471, 17
 Akamatsu, H., & Kawahara, H. 2013, *PASJ*, 65, arXiv:1112.3030
 Akamatsu, H., Mizuno, M., Ota, N., et al. 2017, *A&A*, 600, A100
 Alam, S., Albareti, F. D., Allende Prieto, C., et al. 2015, *ApJS*, 219, 12
 Angulo, R. E., Springel, V., White, S. D. M., et al. 2012, *MNRAS*, 426, 2046
 Aragon-Salamanca, A., Ellis, R. S., Couch, W. J., & Carter, D. 1993, *MNRAS*, 262, 764
 Arnaud, M., Hughes, J. P., Forman, W., et al. 1992, *ApJ*, 390, 345
 Arnaud, M., Maurogordato, S., Slezak, E., & Rho, J. 2000, *A&A*, 355, 461
 Baba, H., Yasuda, N., Ichikawa, S.-I., et al. 2002, in *Astronomical Society of the Pacific Conference Series*, Vol. 281, *Astronomical Data Analysis Software and Systems XI*, ed. D. A. Bohlander, D. Durand, & T. H. Handley, 298
 Bagchi, J., Enßlin, T. A., Miniati, F., et al. 2002, *New A*, 7, 249
 Bagchi, J., Sirothia, S. K., Werner, N., et al. 2011, *ApJL*, 736, L8
 Barrena, R., Boschin, W., Girardi, M., & Spolaor, M. 2007, *A&A*, 469, 861
 Barrena, R., Girardi, M., Boschin, W., & Dasí, M. 2009, *A&A*, 503, 357
 Beers, T. C., Flynn, K., & Gebhardt, K. 1990, *AJ*, 100, 32
 Beers, T. C., Geller, M. J., & Huchra, J. P. 1983, *ApJ*, 264, 356
 Bell, A. R. 1978, *MNRAS*, 182, 147
 Benson, B., Wittman, D. M., Golovich, N., et al. 2017, *ApJ*, 841, 7
 Bertin, E. 2006, in *Astronomical Society of the Pacific Conference Series*, Vol. 351, *Astronomical Data Analysis Software and Systems XV*, ed. C. Gabriel, C. Arviset, D. Ponz, & S. Enrique, 112
 Bertin, E., & Arnouts, S. 1996, *A&AS*, 117, 393
 Bertin, E., Mellier, Y., Radovich, M., et al. 2002, in *Astronomical Society of the Pacific Conference Series*, Vol. 281, *Astronomical Data Analysis Software and Systems XI*, ed. D. A. Bohlander, D. Durand, & T. H. Handley, 228
 Blackburn, J. K. 1995, in *Astronomical Society of the Pacific Conference Series*, Vol. 77, *Astronomical Data Analysis Software and Systems IV*, ed. R. A. Shaw, H. E. Payne, & J. J. E. Hayes, 367
 Bonafede, A., Giovannini, G., Feretti, L., Govoni, F., & Murgia, M. 2009, *A&A*, 494, 429
 Bonafede, A., Intema, H. T., Brüggen, M., et al. 2014, *ApJ*, 785, 1
 Bonafede, A., Brüggen, M., van Weeren, R., et al. 2012, *MNRAS*, 426, 40
 Boschin, W., Barrena, R., & Girardi, M. 2010, *A&A*, 521, A78
 Boschin, W., Girardi, M., & Barrena, R. 2013, *MNRAS*, 434, 772
 Boschin, W., Girardi, M., Spolaor, M., & Barrena, R. 2006, *A&A*, 449, 461
 Botteon, A., Gastaldello, F., Brunetti, G., & Dallacasa, D. 2016, *ArXiv e-prints*, arXiv:1604.07823
 Bourdin, H., Mazzotta, P., Markevitch, M., Giacintucci, S., & Brunetti, G. 2013, *ApJ*, 764, 82
 Bourdin, H., Arnaud, M., Mazzotta, P., et al. 2011, *A&A*, 527, A21
 Bradac, M., Allen, S. W., Treu, T., et al. 2008, *ApJ*, 687, 959
 Brüggen, M., van Weeren, R. J., & Röttgering, H. J. A. 2012, *MNRAS*, 425, L76
 Brunetti, G., & Jones, T. W. 2014, *International Journal of Modern Physics D*, 23, 1430007
 Brunetti, G., Giacintucci, S., Cassano, R., et al. 2008, *Nature*, 455, 944
 Burns, J. O., Roettiger, K., Pinkney, J., et al. 1995, *ApJ*, 446, 583
 Buton, C., Copin, Y., Aldering, G., et al. 2013, *A&A*, 549, A8
 Cassano, R., Ettori, S., Giacintucci, S., et al. 2010, *ApJL*, 721, L82

- Chung, S. M., Gonzalez, A. H., Clowe, D., et al. 2009, ApJ, 691, 963
- Clarke, T. E., Randall, S. W., Sarazin, C. L., Blanton, E. L., & Giacintucci, S. 2013, ApJ, 772, 84
- Clowe, D., Bradac, M., Gonzalez, A., et al. 2006, ApJL, 648, L109
- Coe, D., Umetsu, K., Zitrin, A., et al. 2012, ApJ, 757, 22
- Cohen, A. S., & Clarke, T. E. 2011, AJ, 141, 149
- Cohen, A. S., Lane, W. M., Cotton, W. D., et al. 2007, AJ, 134, 1245
- Condon, J. J., Cotton, W. D., Greisen, E. W., et al. 1998, AJ, 115, 1693
- Cook, R. I., & Dell'Antonio, I. P. 2012, ApJ, 750, 153
- Couch, W. J., & Sharples, R. M. 1987, MNRAS, 229, 423
- Cypriano, E. S., Sodré, Jr., L., Kneib, J.-P., & Campusano, L. E. 2004, ApJ, 613, 95
- Dahle, H., Kaiser, N., Irgens, R. J., Lilje, P. B., & Maddox, S. J. 2002, ApJS, 139, 313
- Dallacasa, D., Brunetti, G., Giacintucci, S., et al. 2009, ApJ, 699, 1288
- Davis, D. S., & White, III, R. E. 1998, ApJ, 492, 57
- Dawson, W. A. 2013, ApJ, 772, 131
- . 2014, MCMAC: Monte Carlo Merger Analysis Code, Astrophysics Source Code Library, , ascl:1407.004
- Dawson, W. A., Wittman, D., Jee, M. J., et al. 2012, ApJL, 747, L42
- Dawson, W. A., Jee, M. J., Stroe, A., et al. 2015, ApJ, 805, 143
- de Gasperin, F., Intema, H. T., van Weeren, R. J., et al. 2015, MNRAS, 453, 3483
- de Gasperin, F., van Weeren, R. J., Brüggen, M., et al. 2014, MNRAS, 444, 3130
- Diego, J. M., Broadhurst, T., Chen, C., et al. 2016, MNRAS, 456, 356
- Djorgovski, S., Lasker, B. M., Weir, W. N., et al. 1992, in Bulletin of the American Astronomical Society, Vol. 24, American Astronomical Society Meeting Abstracts #180, 750
- Donnert, J. M. F., Stroe, A., Brunetti, G., Hoang, D., & Roettgering, H. 2016, MNRAS, 462, 2014
- Dressler, A. 1980, ApJ, 236, 351
- Dressler, A., & Shectman, S. A. 1988, AJ, 95, 985
- Dressler, A., Smail, I., Poggianti, B. M., et al. 1999, ApJS, 122, 51
- Drury, L. O. 1983, Reports on Progress in Physics, 46, 973
- Duffy, A. R., Schaye, J., Kay, S. T., & Dalla Vecchia, C. 2008, MNRAS, 390, L64
- Ebeling, H., Barrett, E., Donovan, D., et al. 2007, ApJL, 661, L33
- Ebeling, H., Edge, A. C., & Henry, J. P. 2001, ApJ, 553, 668
- Ebeling, H., Ma, C.-J., & Barrett, E. 2014, ApJS, 211, 21
- Ebeling, H., Mullis, C. R., & Tully, R. B. 2002, ApJ, 580, 774
- Eckert, D., Jauzac, M., Vazza, F., et al. 2016, MNRAS, 461, 1302
- Edge, A. C., Ebeling, H., Bremer, M., et al. 2003, MNRAS, 339, 913
- Einasto, M., Liivamägi, L. J., Tempel, E., et al. 2012, A&A, 542, A36
- Elbaz, D., Arnaud, M., & Boehringer, H. 1995, A&A, 293
- Ensslin, T. A., Biermann, P. L., Klein, U., & Kohle, S. 1998, A&A, 332, 395
- Evrard, A. E., Bialek, J., Busha, M., et al. 2008, ApJ, 672, 122
- Faber, S. M., Phillips, A. C., Kibrick, R. I., et al. 2003, in Proc. SPIE, Vol. 4841, Instrument Design and Performance for Optical/Infrared Ground-based Telescopes, ed. M. Iye & A. F. M. Moorwood, 1657–1669
- Farnsworth, D., Rudnick, L., Brown, S., & Brunetti, G. 2013, ApJ, 779, 189
- Feretti, L., Boehringer, H., Giovannini, G., & Neumann, D. 1997, A&A, 317, 432
- Feretti, L., Fusco-Femiano, R., Giovannini, G., & Govoni, F. 2001, A&A, 373, 106
- Feretti, L., Giovannini, G., Govoni, F., & Murgia, M. 2012, A&A Rev., 20, 54
- Feretti, L., Orrù, E., Brunetti, G., et al. 2004, A&A, 423, 111
- Feretti, L., Schuecker, P., Böhringer, H., Govoni, F., & Giovannini, G. 2005, A&A, 444, 157
- Ferrari, C., Arnaud, M., Ettori, S., Maurogordato, S., & Rho, J. 2006, A&A, 446, 417
- Ferrari, C., Maurogordato, S., Cappi, A., & Benoist, C. 2003, A&A, 399, 813
- Foreman-Mackey, D., Hogg, D. W., Lang, D., & Goodman, J. 2013, PASP, 125, 306
- Forman, W., Bechtold, J., Blair, W., et al. 1981, ApJL, 243, L133
- Fujita, Y., Akamatsu, H., & Kimura, S. S. 2016, PASJ, 68, 34
- Gabici, S., & Blasi, P. 2003, ApJ, 583, 695
- Geller, M. J., Dell'Antonio, I. P., Kurtz, M. J., et al. 2005, ApJL, 635, L125
- Geller, M. J., Diaferio, A., Rines, K. J., & Serra, A. L. 2013, ApJ, 764, 58
- Geller, M. J., Hwang, H. S., Fabricant, D. G., et al. 2014, ApJS, 213, 35
- Geller, M. J., Kurtz, M. J., Dell'Antonio, I. P., Ramella, M., & Fabricant, D. G. 2010, ApJ, 709, 832
- George, L. T., Dwarakanath, K. S., Johnston-Hollitt, M., et al. 2017, MNRAS, 467, 936
- Giacintucci, S., Venturi, T., Macario, G., et al. 2008, A&A, 486, 347
- Giler, M., Wdowczyk, J., & Wolfendale, A. W. 1980, Journal of Physics G Nuclear Physics, 6, 1561
- Giovannini, G., Bonafede, A., Feretti, L., Govoni, F., & Murgia, M. 2010, A&A, 511, L5
- Giovannini, G., Bonafede, A., Feretti, L., et al. 2009, A&A, 507, 1257
- Giovannini, G., Feretti, L., Girardi, M., et al. 2011, A&A, 530, L5
- Giovannini, G., Feretti, L., & Gregorini, L. 1987, A&AS, 69, 171
- Giovannini, G., Tordi, M., & Feretti, L. 1999, New A, 4, 141
- Giovannini, G., Vacca, V., Girardi, M., et al. 2013, MNRAS, 435, 518
- Girardi, M., Boschin, W., Gastaldello, F., et al. 2016, MNRAS, 456, 2829
- Gladders, M. D., López-Cruz, O., Yee, H. K. C., & Kodama, T. 1998, ApJ, 501, 571
- Golovich, N., Dawson, W. A., Wittman, D., et al. 2016, ApJ, 831, 110
- Golovich, N., van Weeren, R. J., Dawson, W. A., Jee, M. J., & Wittman, D. 2017, ApJ, 838, 110
- Gonzalez, A. H., Sivanandam, S., Zabludoff, A. I., & Zaritsky, D. 2013, ApJ, 778, 14
- Govoni, F., EnBlin, T. A., Feretti, L., & Giovannini, G. 2001a, A&A, 369, 441
- Govoni, F., Feretti, L., Giovannini, G., et al. 2001b, A&A, 376, 803
- Govoni, F., Ferrari, C., Feretti, L., et al. 2012, A&A, 545, A74
- Govoni, F., Markevitch, M., Vikhlinin, A., et al. 2004, ApJ, 605, 695
- Govoni, F., Murgia, M., Feretti, L., et al. 2005, A&A, 430, L5
- Govoni, F., Murgia, M., Giovannini, G., Vacca, V., & Bonafede, A. 2011, A&A, 529, A69
- Gruen, D., Seitz, S., Brimioule, F., et al. 2014, MNRAS, 442, 1507
- Gunn, J. E., & Gott, III, J. R. 1972, ApJ, 176, 1
- Gutierrez, K., & Krawczynski, H. 2005, ApJ, 619, 161
- Hallman, E. J., & Markevitch, M. 2004, ApJL, 610, L81
- Harvey, D., Courbin, F., Kneib, J. P., & McCarthy, I. G. 2017, ArXiv e-prints, arXiv:1703.07365
- Harvey, D., Massey, R., Kitching, T., Taylor, A., & Tittley, E. 2015, Science, 347, 1462
- Hayashi, E., & White, S. D. M. 2006, MNRAS, 370, L38
- Hintzen, P., & Scott, J. S. 1980, ApJ, 239, 765
- Hwang, H. S., & Lee, M. G. 2007, ApJ, 662, 236
- Jauzac, M., Richard, J., Jullo, E., et al. 2015, MNRAS, 452, 1437
- Jauzac, M., Eckert, D., Schwinn, J., et al. 2016, MNRAS, 463, 3876
- Jee, M. J., Dawson, W. A., Stroe, A., et al. 2016, ApJ, 817, 179
- Jee, M. J., Hughes, J. P., Menanteau, F., et al. 2014, ApJ, 785, 20
- Jee, M. J., Stroe, A., Dawson, W., et al. 2015, ApJ, 802, 46
- Jeltema, T. E., Canizares, C. R., Bautz, M. W., & Buote, D. A. 2005, ApJ, 624, 606
- Johnson, T. L., Sharon, K., Bayliss, M. B., et al. 2014, ApJ, 797, 48
- Kahlhoefer, F., Schmidt-Hoberg, K., Frandsen, M. T., & Sarkar, S. 2014, MNRAS, 437, 2865
- Kang, H., & Ryu, D. 2016, ApJ, 823, 13
- Kang, H., Ryu, D., & Jones, T. W. 2012, ApJ, 756, 97
- Kaplinghat, M., Tulin, S., & Yu, H.-B. 2016, Physical Review Letters, 116, 041302
- Kass, R. E., & Raftery, A. E. 1995, Journal of the American Statistical Association, 90, 773

- Kawamata, R., Oguri, M., Ishigaki, M., Shimasaku, K., & Ouchi, M. 2016, ApJ, 819, 114
- Kelly, P. L., Rodney, S. A., Treu, T., et al. 2015, Science, 347, 1123
- Kempner, J. C., & David, L. P. 2004, MNRAS, 349, 385
- Kempner, J. C., & Sarazin, C. L. 2001, ApJ, 548, 639
- Kempner, J. C., Sarazin, C. L., & Markevitch, M. 2003, ApJ, 593, 291
- Kierdorf, M., Beck, R., Hoeft, M., et al. 2016, ArXiv e-prints, arXiv:1612.01764
- Kim, S. Y., Peter, A. H. G., & Wittman, D. 2017, MNRAS, 469, 1414
- Kocevski, D. D., Ebeling, H., Mullis, C. R., & Tully, R. B. 2007, ApJ, 662, 224
- Kodama, T., & Arimoto, N. 1997, A&A, 320, 41
- Kubo, J. M., Khiabanian, H., Dell'Antonio, I. P., Wittman, D., & Tyson, J. A. 2009, ApJ, 702, 980
- Lam, D., Broadhurst, T., Diego, J. M., et al. 2014, ApJ, 797, 98
- Lemonon, L., Pierre, M., Hunstead, R., et al. 1997, A&A, 326, 34
- Lotz, J., Mountain, M., Grogan, N. A., et al. 2014, in American Astronomical Society Meeting Abstracts, Vol. 223, American Astronomical Society Meeting Abstracts #223, 254.01
- Macario, G., Venturi, T., Intema, H. T., et al. 2013, A&A, 551, A141
- Mahler, G., Richard, J., Clément, B., et al. 2017, ArXiv e-prints, arXiv:1702.06962
- Marini, F., Bardelli, S., Zucca, E., et al. 2004, MNRAS, 353, 1219
- Markevitch, M. 2006, in ESA Special Publication, Vol. 604, The X-ray Universe 2005, ed. A. Wilson, 723
- Markevitch, M., Gonzalez, A. H., Clowe, D., et al. 2004, ApJ, 606, 819
- Markevitch, M., Gonzalez, A. H., David, L., et al. 2002, ApJL, 567, L27
- Markevitch, M., Mushotzky, R., Inoue, H., et al. 1996, ApJ, 456, 437
- Markevitch, M., & Vikhlinin, A. 2001, ApJ, 563, 95
- Markevitch, M., Yamashita, K., Furuzawa, A., & Tawara, Y. 1994, ApJL, 436, L71
- Maurogordato, S., Proust, D., Beers, T. C., et al. 2000, A&A, 355, 848
- Maurogordato, S., Cappi, A., Ferrari, C., et al. 2008, A&A, 481, 593
- Mazzotta, P., Bourdin, H., Giacintucci, S., Markevitch, M., & Venturi, T. 2011, Mem. Soc. Astron. Italiana, 82, 495
- Medezinski, E., Umetsu, K., Okabe, N., et al. 2016, ApJ, 817, 24
- Merten, J., Coe, D., Dupke, R., et al. 2011, MNRAS, 417, 333
- Miller, C. J., Krughoff, K. S., Batuski, D. J., & Hill, J. M. 2002, AJ, 124, 1918
- Miller, N. A., & Owen, F. N. 2003, AJ, 125, 2427
- Miyazaki, S., Komiyama, Y., Sekiguchi, M., et al. 2002, PASJ, 54, 833
- Molnar, S. M., & Broadhurst, T. 2017, ApJ, 841, 46
- Navarro, J. F., Frenk, C. S., & White, S. D. M. 1996, ApJ, 462, 563
- Newman, A. B., Treu, T., Ellis, R. S., & Sand, D. J. 2012a, ArXiv e-prints, arXiv:1209.1392
- Newman, A. B., Treu, T., Ellis, R. S., et al. 2012b, ArXiv e-prints, arXiv:1209.1391
- Newman, J. A., Cooper, M. C., Davis, M., et al. 2013, ApJS, 208, 5
- Ng, K. Y., Dawson, W. A., Wittman, D., et al. 2015, MNRAS, 453, 1531
- Ng, K. Y., Pillepich, A., Wittman, D., et al. 2017, ArXiv e-prints, arXiv:1703.00010
- Nord, M., Basu, K., Pacaud, F., et al. 2009, A&A, 506, 623
- Oegerle, W. R., & Hill, J. M. 2001, AJ, 122, 2858
- Ogorean, G., Brüggen, M., Simionescu, A., et al. 2013a, Astronomische Nachrichten, 334, 342
- Ogorean, G. A., Brüggen, M., Röttgering, H., et al. 2013b, MNRAS, 429, 2617
- Ogorean, G. A., Brüggen, M., van Weeren, R. J., Burgmeier, A., & Simionescu, A. 2014, MNRAS, 443, 2463
- Ogorean, G. A., Brüggen, M., van Weeren, R. J., et al. 2013c, MNRAS, 433, 812
- Ogorean, G. A., van Weeren, R. J., Jones, C., et al. 2016, ApJ, 819, 113
- Oguri, M. 2015, MNRAS, 449, L86
- Oguri, M., Takada, M., Okabe, N., & Smith, G. P. 2010, MNRAS, 405, 2215
- Ohashi, T., Akamatsu, H., Kawahara, H., Sekiya, N., & Takei, Y. 2013, Astronomische Nachrichten, 334, 325
- Okabe, N., Akamatsu, H., Kakuwa, J., et al. 2015, PASJ, 67, 114
- Okabe, N., Bourdin, H., Mazzotta, P., & Maurogordato, S. 2011, ApJ, 741, 116
- Okabe, N., Takada, M., Umetsu, K., Futamase, T., & Smith, G. P. 2010, PASJ, 62, 811
- Okabe, N., & Umetsu, K. 2008, PASJ, 60, 345
- Ota, N., Nagayoshi, K., Pratt, G. W., et al. 2014, A&A, 562, A60
- Ouchi, M., Shimasaku, K., Okamura, S., et al. 2004, ApJ, 611, 660
- Owers, M. S., Couch, W. J., Nulsen, P. E. J., & Randall, S. W. 2012, ApJL, 750, L23
- Owers, M. S., Randall, S. W., Nulsen, P. E. J., et al. 2011, ApJ, 728, 27
- Owers, M. S., Nulsen, P. E. J., Couch, W. J., et al. 2014, ApJ, 780, 163
- Peter, A. H. G., Rocha, M., Bullock, J. S., & Kaplinghat, M. 2012, ArXiv e-prints, arXiv:1208.3026
- Pierre, M., Boehringer, H., Ebeling, H., et al. 1994, A&A, 290
- Pierre, M., Oukbir, J., Dubreuil, D., et al. 1997, A&AS, 124, doi:10.1051/aas:1997192
- Pinkney, J., Roettiger, K., Burns, J. O., & Bird, C. M. 1996, ApJS, 104, 1
- Pizzo, R. F., & de Bruyn, A. G. 2009, A&A, 507, 639
- Planck Collaboration, Ade, P. A. R., Aghanim, N., et al. 2011, A&A, 536, A8
- . 2013, A&A, 550, A134
- . 2014, A&A, 571, A29
- . 2016, A&A, 594, A24
- Poggianti, B. M., Bridges, T. J., Komiyama, Y., et al. 2004, ApJ, 601, 197
- Postman, M., Coe, D., Benítez, N., et al. 2012, ApJS, 199, 25
- Pratt, G. W., Croston, J. H., Arnaud, M., & Böhringer, H. 2009, A&A, 498, 361
- Radovich, M., Puddu, E., Romano, A., Grado, A., & Getman, F. 2008, A&A, 487, 55
- Randall, S. W., Markevitch, M., Clowe, D., Gonzalez, A. H., & Bradac, M. 2008, ApJ, 679, 1173
- Rawle, T. D., Altieri, B., Egami, E., et al. 2014, MNRAS, 442, 196
- Refsdal, S. 1964, MNRAS, 128, 307
- Reid, A. D., Hunstead, R. W., Lemonon, L., & Pierre, M. M. 1999, MNRAS, 302, 571
- Rengelink, R. B., Tang, Y., de Bruyn, A. G., et al. 1997, A&AS, 124, doi:10.1051/aas:1997358
- Rephaeli, Y., Gruber, D., & Arieli, Y. 2006, ApJ, 649, 673
- Richard, J., Smith, G. P., Kneib, J.-P., et al. 2010, MNRAS, 404, 325
- Ricker, P. M., & Sarazin, C. L. 2001, ApJ, 561, 621
- Rines, K., & Diaferio, A. 2006, AJ, 132, 1275
- Rocha, M., Peter, A. H. G., Bullock, J. S., et al. 2012, ArXiv e-prints, arXiv:1208.3025
- Rossetti, M., Gastaldello, F., Eckert, D., et al. 2017, MNRAS, 468, 1917
- Rottgering, H. J. A., Wieringa, M. H., Hunstead, R. W., & Ekers, R. D. 1997, MNRAS, 290, 577
- Rudnick, L., & Lemmert, J. A. 2009, ApJ, 697, 1341
- Russell, H. R., Sanders, J. S., Fabian, A. C., et al. 2010, MNRAS, 406, 1721
- Sakelliou, I., & Ponman, T. J. 2006, MNRAS, 367, 1409
- Sanderson, A. J. R., O'Sullivan, E., Ponman, T. J., et al. 2013, MNRAS, 429, 3288
- Saro, A., Mohr, J. J., Bazin, G., & Dolag, K. 2013, ApJ, 772, 47
- Schlafly, E. F., & Finkbeiner, D. P. 2011, ApJ, 737, 103
- Schlegel, D. J., Finkbeiner, D. P., & Davis, M. 1998, ApJ, 500, 525
- Schneider, M. D., Frenk, C. S., & Cole, S. 2012, J. Cosmology Astropart. Phys., 5, 30
- Schwinn, J., Jauzac, M., Baugh, C. M., et al. 2017, MNRAS, 467, 2913
- Sehgal, N., Hughes, J. P., Wittman, D., et al. 2008, ApJ, 673, 163
- Sharon, K., & Johnson, T. L. 2015, ApJL, 800, L26
- Shibata, R., Honda, H., Ishida, M., Ohashi, T., & Yamashita, K. 1999, ApJ, 524, 603
- Shimwell, T. W., Luckin, J., Brüggen, M., et al. 2016, MNRAS, 459, 277

- Skillman, S. W., Warren, M. S., Turk, M. J., et al. 2014, ArXiv e-prints, arXiv:1407.2600
- Skillman, S. W., Xu, H., Hallman, E. J., et al. 2013, ApJ, 765, 21
- Skrutskie, M. F., Cutri, R. M., Stiening, R., et al. 2006, AJ, 131, 1163
- Smith, G. P., Ebeling, H., Limousin, M., et al. 2009, ApJL, 707, L163
- Sobral, D., Stroe, A., Dawson, W. A., et al. 2015, /mnras, 450, 630
- Soucail, G. 2012, A&A, 540, A61
- Springel, V., & Farrar, G. R. 2007, MNRAS, 380, 911
- Squires, G., Neumann, D. M., Kaiser, N., et al. 1997, ApJ, 482, 648
- Stanford, S. A., Eisenhardt, P. R., & Dickinson, M. 1998, ApJ, 492, 461
- Steigman, G. 2008, J. Cosmology Astropart. Phys., 10, 1
- Stroe, A., Harwood, J. J., Hardcastle, M. J., & Röttgering, H. J. A. 2014a, MNRAS, 445, 1213
- Stroe, A., Sobral, D., Paulino-Afonso, A., et al. 2017, MNRAS, 465, 2916
- Stroe, A., Sobral, D., Röttgering, H. J. A., & van Weeren, R. J. 2014b, MNRAS, 438, 1377
- Stroe, A., van Weeren, R. J., Intema, H. T., et al. 2013, A&A, 555, A110
- Stroe, A., Rumsey, C., Harwood, J. J., et al. 2014c, MNRAS, 441, L41
- Stroe, A., Sobral, D., Dawson, W., et al. 2015, MNRAS, 450, 646
- Sun, M., Voit, G. M., Donahue, M., et al. 2009, ApJ, 693, 1142
- Takizawa, M., Nagino, R., & Matsushita, K. 2010, PASJ, 62, 951
- Tarenghi, M., & Scott, J. S. 1976, ApJL, 207, L9
- Taylor, M. B. 2005, in Astronomical Society of the Pacific Conference Series, Vol. 347, Astronomical Data Analysis Software and Systems XIV, ed. P. Shopbell, M. Britton, & R. Ebert, 29
- Treu, T., Brammer, G., Diego, J. M., et al. 2016, ApJ, 817, 60
- Tulin, S., & Yu, H.-B. 2017, ArXiv e-prints, arXiv:1705.02358
- Umetsu, K., Zitrin, A., Gruen, D., et al. 2015, ArXiv e-prints, arXiv:1507.04385
- Umetsu, K., Medezinski, E., Nonino, M., et al. 2014, ApJ, 795, 163
- Valtchanov, I., Murphy, T., Pierre, M., Hunstead, R., & Lémonon, L. 2002, A&A, 392, 795
- van Weeren, R. J., Bonafede, A., Ebeling, H., et al. 2012a, MNRAS, 425, L36
- van Weeren, R. J., Brüggen, M., Röttgering, H. J. A., & Hoeft, M. 2011a, MNRAS, 418, 230
- van Weeren, R. J., Brüggen, M., Röttgering, H. J. A., et al. 2011b, A&A, 533, A35
- van Weeren, R. J., Hoeft, M., Röttgering, H. J. A., et al. 2011c, A&A, 528, A38
- van Weeren, R. J., Röttgering, H. J. A., & Brüggen, M. 2011d, A&A, 527, A114
- van Weeren, R. J., Röttgering, H. J. A., Brüggen, M., & Cohen, A. 2009a, A&A, 508, 75
- van Weeren, R. J., Röttgering, H. J. A., Brüggen, M., & Hoeft, M. 2010, Science, 330, 347
- van Weeren, R. J., Röttgering, H. J. A., Intema, H. T., et al. 2012b, A&A, 546, A124
- van Weeren, R. J., Röttgering, H. J. A., Bagchi, J., et al. 2009b, A&A, 506, 1083
- van Weeren, R. J., Fogarty, K., Jones, C., et al. 2013, ApJ, 769, 101
- van Weeren, R. J., Oglean, G. A., Jones, C., et al. 2016, ApJ, 817, 98
- van Weeren, R. J., Andrade-Santos, F., Dawson, W. A., et al. 2017, Nature Astronomy, 1, 0005
- Venturi, T., Giacintucci, G., Dallacasa, D., et al. 2011, MNRAS, 414, L65
- Venturi, T., Giacintucci, S., Brunetti, G., et al. 2007, A&A, 463, 937
- Venturi, T., Giacintucci, S., Dallacasa, D., et al. 2008, A&A, 484, 327
- . 2013, A&A, 551, A24
- Vikhlinin, A., Kravtsov, A., Forman, W., et al. 2006, ApJ, 640, 691
- Vikhlinin, A., Markevitch, M., Murray, S. S., et al. 2005, ApJ, 628, 655
- Vogelsberger, M., Genel, S., Springel, V., et al. 2014, MNRAS, 444, 1518
- Voges, W., Aschenbach, B., Boller, T., et al. 1999, A&A, 349, 389
- Wen, Z.-L., Yang, Y.-B., Yuan, Q.-R., et al. 2007, Chinese J. Astron. Astrophys., 7, 71
- West, M. J., de Propris, R., Bremer, M. N., & Phillipps, S. 2017, Nature Astronomy, 1, 0157
- White, D. A., Jones, C., & Forman, W. 1997, MNRAS, 292, 419
- Wilbanks, T. M., Ade, P. A. R., Fischer, M. L., Holzapfel, W. L., & Lange, A. E. 1994, ApJL, 427, L75
- Wittman, D., Dawson, W., & Benson, B. 2014, MNRAS, 437, 3578
- Wittman, D., Dell'Antonio, I. P., Hughes, J. P., et al. 2006, ApJ, 643, 128
- Wittman, D., Golovich, N., & Dawson, W. A. 2017, ArXiv e-prints, arXiv:1701.05877
- Wittman, D. M., Tyson, J. A., Dell'Antonio, I. P., et al. 2002, in Society of Photo-Optical Instrumentation Engineers (SPIE) Conference Series, Vol. 4836, Society of Photo-Optical Instrumentation Engineers (SPIE) Conference Series, ed. J. A. Tyson & S. Wolff, 73–82
- Yagi, M., Kashikawa, N., Sekiguchi, M., et al. 2002, AJ, 123, 66
- Yuan, Q., Zhou, X., & Jiang, Z. 2003, ApJS, 149, 53
- Zheng, W., Postman, M., Zitrin, A., et al. 2012, Nature, 489, 406
- Ziparo, F., Braglia, F. G., Pierini, D., et al. 2012, MNRAS, 420, 2480
- Zitrin, A., & Broadhurst, T. 2009, ApJL, 703, L132
- Zitrin, A., Seitz, S., Monna, A., et al. 2017, ApJL, 839, L11